Universidade do Minho
Escola de Engenharia

Ivo Henrique Baltazar Colmiais

Design and optimization of graphene passive circuits for radiofrequency biomedical sensors

julho de 2024

Design and optimization of graphene passive circuits for radiofrequency biomedical sensors
Ivo Henrique Baltazar Colmiais
UMinho | 2024

Universidade do Minho
Escola de Engenharia

Ivo Henrique Baltazar Colmiais

Design and optimization of graphene passive circuits for radiofrequency biomedical sensors

Tese de Doutoramento
Engenharia Biomédica

Trabalho efetuado sob a orientação do
Professor Doutor Paulo M. Mendes
Doutor Jérôme Gilles Ollivier Borme

julho de 2024

Direitos de autor e condições de utilização do trabalho por terceiros

Este é um trabalho académico que pode ser utilizado por terceiros desde que respeitadas as regras e boas práticas internacionalmente aceites, no que concerne aos direitos de autor e direitos conexos.

Assim, o presente trabalho pode ser utilizado nos termos previstos na licença abaixo indicada.

Caso o utilizador necessite de permissão para poder fazer um uso do trabalho em condições não previstas no licenciamento indicado, deverá contactar o autor, através do RepositóriUM da Universidade do Minho.

Licença concedida aos utilizadores deste trabalho



Atribuição-NãoComercial
CC BY-NC

https://creativecommons.org/licenses/by-nc/4.0/

Agradecimentos

Quero agradecer, em primeiro lugar, aos meus pais, Francisco e Alzira, pelo apoio constante, sacrifícios, amor, carinho e dedicação que me deram ao longo de toda a minha vida. Agradeço também à Bibiana pelo apoio, força e compreensão durante os momentos mais desafiantes. O meu percurso até aqui foi conseguido através de todo o vosso suporte.

Agradeço ao meu orientador, o Professor Doutor Paulo Mateus Mendes, pelos desafios propostos, a sua orientação e conselhos valiosos para o desenvolvimento deste trabalho ao longo ao longo dos anos. Para além disso, quero agradecer por todas as discussões, partilhas de conhecimentos e experiência que me permitiram evoluir em todos os aspetos.

Ao meu co-orientador, Doutor Jérôme Borme pela sua orientação, dedicação, conhecimentos e colaboração ao longo dos últimos anos que permitiram que o trabalho de sala limpa decorresse com maior fluidez.

Agradeço também à Universidade do Minho e ao INL (Laboratório Ibérico Internacional de Nanotecnologia) que me acolheram e proporcionaram instalações, recursos, e suporte institucional para o desenvolvimento deste trabalho.

Aos meus amigos e colegas de laboratório de Gualtar e do INL, tenho a agradecer o excelente ambiente de trabalho, os conselhos, as discussões e a entreajuda. Em particular, ao Hugo que sempre me incentivou, encorajou, e esteve sempre presente o desenvolvimento deste trabalho. Ao Vítor, agradeço também por todo o suporte, discussões, motivação e companheirismo que foram indispensáveis para a realização deste trabalho.

Agradeço também à Fundação para a Ciência e Tecnologia (FCT) pelo financiamento através das bolsas SFRH/BD/141462/2018 e COVID/BD/153002/2022, cofinanciadas pelo FSE através do Programa Operacional Regional

Statement of integrity

I hereby declare having conducted this academic work with integrity. I confirm that I have not used plagiarism or any form of undue use of information or falsification of results along the process leading to its elaboration.

I further declare that I have fully acknowledged the Code of Ethical Conduct of the University of Minho.

Resumo

O grafeno é um material atrativo pelas suas propriedades, o que se reflete no crescente número de publicações. Na busca por melhorias de desempenho e escalabilidade na eletrónica, o grafeno surge como candidato para aplicações de alta frequência devido às suas características elétricas. Possíveis áreas onde pode de ser utilizado são em circuitos radiofrequência (RF) sintonizáveis e aplicações biomédicas, possibilitando o desenvolvimento de biossensores sem fios de grafeno.

Os avanços tecnológicos tornaram os biossensores mais precisos e compactos. Hoje, espera-se que sejam práticos e com mínimo impacto no utilizador, como a leitura sem contato. Isto pode ser conseguido, por exemplo, através de biossensores RF de grafeno miniaturizados e sem fios. No entanto, a modelagem de dispositivos passivos de grafeno não está bem estabelecida e os simuladores modernos não a suportam, além da variabilidade do processo de fabrico que aumenta a complexidade. Torna-se necessário desenvolver ferramentas e metodologias para extrair e modelar com precisão as propriedades do grafeno, essenciais para soluções práticas de biossensores RF confiáveis e eficientes.

A abordagem para extrair as propriedades do grafeno foi utilizar a calibração TRL, em que a espessura do metal, a perda do substrato e o efeito da presença da *backgate* foram optimizados para garantir a precisão das medições. Em seguida, a calibração foi utilizada para extrair as propriedades do grafeno, tais como a sua resistência de contacto, a capacidade de contacto, a resistência intrínseca, a capacidade intrínseca e a indutância intrínseca. O processo de fabrico atingiu um rendimento de cerca de 40% a 55% utilizando grafeno monocamada. Estes dispositivos foram caracterizados de 1 GHz a 8.5 GHz, para uma tensão de *gate* de 0 V a 15 V e para uma largura de 50 µm. Estes dispositivos apresentaram uma resistência de grafeno extraída de 113 Ω até 886 Ω, uma capacidade extraída de 0.36 pF até 1.2 pF e uma indutância extraída máxima de 4.75 nH.

A validade da metodologia implementada, bem como a utilidade das propriedades RF extraídas do grafeno, foi demonstrada através do desenvolvimento de uma antena metálica que integra grafeno. Em seguida, através da comparação das medições e simulações de *backscatter*, foi possível modelar uma aproximação da resposta de *backscatter* esperada.

Os resultados deste trabalho contribuíram para o avanço do conhecimento sobre o grafeno, extraindo as suas propriedades e aumentando o conhecimento sobre a sua resistência sintonizável, capacidade quântica e indutância cinética. Estas são úteis para modelar e prever o comportamento de dispositivos de grafeno. Através do apoio da literatura, é possível concluir que a natureza sintonizável do grafeno pode permitir o desenvolvimento de novas soluções para aplicações de RF.

Palavras-chave: grafeno, radiofrequência, dispositivos passivos

Abstract

Graphene is a very attractive material due to its properties, which translates to an increasing number of publications over the years. In the endless search for performance improvement and scalability in electronics, graphene emerges as a novel candidate for high frequency applications due to its electrical characteristics. A possible application where it can be used is tunable radiofrequency (RF) circuits and even for biomedical applications, opening the possibility of developing graphene wireless biosensors.

Throughout the years, technological advancements have allowed biosensors to become extremely accurate and compact devices. Nowadays, these are also expected to be convenient, and have minimal impact on the user. An example is non-contact reading which could be achieved, for example, through RF graphene biosensors, being both miniaturized and having wireless readout. Developing such solutions depends on the ease and predictability of designing graphene electronics where graphene's tunable nature, quantum capacitance, and kinetic inductance must be considered. Currently, modelling graphene passive devices is not well established, modern simulators do not support it, and with fabrication process variability adding another level of complexity. Thus, it is necessary to develop tools and methodologies to extract graphene properties, allowing to predict and accurately model graphene components.

The approach to extract graphene's properties was using the TRL calibration where the metal thickness, substrate loss, and the effect of the back gate presence were analyzed to ensure the accuracy of the measurements. Then, it was used to extract graphene properties such as its contact resistance, contact capacitance, intrinsic resistance, intrinsic capacitance, and intrinsic inductance. The fabrication process achieved a yield of around 40% to 55% using monolayer graphene. These were characterized from 1 GHz to 8.5 GHz, for a 0 V to 15 V gate voltage and for 50 μm width. These devices had an extracted graphene resistance from 113 Ω up to 886 Ω, extracted capacitance from 0.36 pF up to 1.2 pF and a maximum extracted inductance of 4.75 nH.

The validity of the implemented methodology as well as the usefulness of the extracted graphene RF properties was demonstrated through developing a metallic antenna that integrates graphene. Then, through comparing the backscatter measurements and simulations, it was possible to model an approximation of the expected backscatter response.

This work's results further advance the knowledge on graphene, extracting its properties and increasing the knowledge on its tunable resistance, quantum capacitance and kinetic inductance. These are useful to model and predict graphene device's behavior. Through the literature support, it's possible to conclude that graphene's tunable nature could allow to develop novel solutions for RF applications.

Keywords: graphene, radiofrequency, passive devices

Table of Contents

List of abbreviations and acronyms viii

List of figures ix

List of tables xv

1 Introduction 1

1.1 Motivation 3

1.2 Objectives 4

1.3 Main contribution 5

1.4 Thesis outline 7

2 Graphene RF passive elements 8

2.1 Graphene inductors 10

2.2 Graphene capacitors 13

2.3 Graphene antennas 17

2.4 Device modeling 22

2.4.1 Modeling of graphene inductors 23

2.4.2 Modeling of graphene capacitors 24

2.4.3 Modeling of graphene antennas 25

2.5 Discussion 27

3 Extraction of graphene RF parameters 31

3.1 TRL calibration implementation 31

3.2 Design of calibration structures 32

3.3 CPW characteristic impedance measurement 33

3.4 Two-dimensional materials TRL calibration methodology performance assessment 34

3.4.1 Metal thickness effect on calibration accuracy 35

3.4.2 Substrate loss effect on calibration accuracy 36

3.4.3 Effect of transition from metallic CPW to 2D CPW device interface 37

3.4.4 Effect of back gate on the extracted graphene's characteristics 39

3.4.5 TRL validation for 2D material properties extraction 40

3.5 DUT parameter extraction methodology 42

3.5.1 Pi-model 43

3.6 Discussion 45

4 Fabrication of graphene devices and calibration structures 46

4.1 Cleanroom facilities 46

4.2 Fabrication requirements from simulations 46

4.3 Backgate conductivity evaluation 47

4.4 Electroplating growth of copper 50

4.5 Etchant compatibility 54

4.6 Graphene fabrication and techniques 57

4.6.1 Graphene growth 57

4.6.2 Large graphene crystal flakes 59

4.6.3 Graphene transfer 64

4.6.4 Reducing graphene contact resistance 68

4.7 Fabrication process for graphene devices and calibration structures 69

4.8 Fabricated devices analysis 77

5 High frequency characterization of graphene 79

5.1 Measurement setup 79

5.2 Measurement of graphene's characteristics 81

5.3 Extracting graphene characteristics 82

6 Graphene wireless sensor readout 92

6.1 Wireless readout working principle 92

6.2 Antenna design 94

6.3 Wireless readout of graphene sensor 95

7 Conclusions 101

7.1 Future work 103

8 References 104

Annex 1 - Hardmask fabrication 117

Annex 2 - Confocal Raman spectroscopy 119

LIST OF ABBREVIATIONS AND ACRONYMS

AMW	Average molecular weight
ASD	Amperes per square decimeter
CMOS	Complementary metal-oxide semiconductor
CPW	Coplanar waveguide
CVD	Chemical vapor deposition
DI	Deionized
DUT	Device under test
DWL	Direct write laser
EBR	Edge beam removal
FD	Forward directivity
FET	Field effect transistor
FRT	Forward reflection tracking
FSM	Forward source match
HDMS	Hexamethyldisilizane
IC	Integrated circuit
INL	International Iberian Nanotechnology Laboratory
IPA	Isopropyl alcohol
ITO	Indium tin oxide
LRM	Line-reflect-match
MEMS	Microelectromechanical System
MLG	Multilayer graphene
MOSCAP	Metal-oxide-semiconductor capacitors
PDMS	Polidimethilsiloxane
PMMA	Poly(methyl methacrylate)
RF	Radiofrequency
SOLT	Short-open-load-through
TRL	Through-reflect-line
VNA	Vector network analyzer

LIST OF FIGURES

Figure 1 - Fabricated graphene inductors (in octagonal shape, narrow square, and wide square) and their respective inductance and Q-factors [26]. 10

Figure 2 - Fabricated graphene square inductors with ¾-, 2-, and 3-turns, presented in [15]. 11

Figure 3 - a) Schematic of the graphene spiral inductor with the equivalent circuit parameters. b) Is the exploded view of a). c) Is the equivalent circuit model of the device presented in a). d) is a schematic view of the graphene inductor [15]. 11

Figure 4 - Fabricated ¾ turn graphene inductor, and measured Q factor until 67 GHz and predicted until 200 GHz [27]. 12

Figure 5 - Fabricated doped multilayer graphene inductor through electrophoretic deposition on the left, and Q factor on the right [37]. 13

Figure 6 - Diagram of the capacitor (left), and microscope image of the fabricated graphene biosensing capacitor (center) and capacitance value for different glucose concentrations (right) [29]. 13

Figure 7 - Proposed tunable LC tank with a graphene capacitor (left) and fabrication steps of the device, including the graphene transfer, metallic contact patterning and oxide deposition through evaporation (right) [30]. 14

Figure 8 - Capacitance (left) and Q-factors (right) of the fabricated graphene capacitor [30]. 14

Figure 9 -On the left, the effects on the Q-factor by modifying the capacitors parameters are plotted: L - length of fingers, W-width of fingers, S-spacing, t-thickness; the image on the right depicts the effects on the Q-factor by the equivalent oxide thickness and disorder in graphene (Dirac point) [31]. ... 15

Figure 10 - Proposed capacitor with intercalated graphene and hBN layers, where graphene was modelled as a conductor and hBN as insulator, for the THz range [38]. 16

Figure 11 - a) Optical image of the fabricated capacitor. b) conceptual and schematic drawing of the graphene capacitor. c) equivalent circuit of the graphene capacitor. d) capacitance dependence on bias voltage and AC signal voltage. e) experimental and theoretical quantum capacitance of the device. 16

Figure 12 - Proposed graphene patch antenna on the left, and its tunability range on the right [33]. ... 17

Figure 13 - Diagram depicting the graphene dipole proposed in [39], with the antenna design as well as substrate structure. 18

Figure 14 - Proposed graphene dipole that includes two additional graphene parasitic structures to reconfigure the antenna's radiation pattern, proposed in [34]. 18

Figure 15 - Designs and simulation in CST of different THz antennas proposed in [40]. 19
Figure 16 - Proposed graphene leaky-wave antenna (left) with beam scanning capabilities for THz and radiation patterns (right) [35]. 19
Figure 17 – A) proposed plasmon-induced graphene antenna with a nonamer array. B) dirac point shift with the wavelength. C) simplified proposed plasmon-induced graphene antenna with a heptamer. D) Scanning electron microscope image of the fabricated plasmon-induced graphene antenna [41], [42]. 20
Figure 18 - Proposed dipole (top left) and its on and off radiation pattern (top right) for 120 GHz, and the THz antenna array's radiation pattern with all antennas turned on (bottom left), and with two lines turned off (bottom right) [36]. 21
Figure 19 - Fabricated graphene antennas on the left side, and S11 with different DC bias on the right side [44]. 22
Figure 20 - Fabricated graphene antenna on the left and measured gain on the right [45]. 22
Figure 21 - Equivalent model of a graphene quantum capacitor. 24
Figure 22 - Calibration structures and dimensions used in the implementation of the TRL calibration algorithm. 33
Figure 23 - Comparison of extracted inductance and resistance parameters of the lumped model when 20 nm thick gold contacts are used, and the expected reference values. 36
Figure 24 - Comparison of extracted inductance and resistance parameters of the lumped model when a substrate with 100 Ω.cm conductivity is used and the expected reference values. 37
Figure 25 - Metallic contact between copper and the 2D material: (A) the case where the material is contacted directly to copper; (B) the case where the material is contacted with a 20 nm thick gold contact; (C) the consequence of undertaking scenario A and demonstrating the 2D material breaking and not making contact with copper; in (D) the consequence of scenario B, where the contact between the copper and 2D material is mediated through a 20 nm thick gold contact and the 2D material lays flat; (E) the consequence of scenario B, where the contact between the copper and 2D material is mediated through a 20 nm thick gold contact, and the material breaks and rolls back. 38
Figure 26 - Comparison of extracted inductance and resistance parameters of the lumped model when the contacts are made of 5 μm thick copper and the substrate has a conductivity of 10 kΩ·cm, and when 20 nm thick gold contacts are included, with the expected reference values. 39

Figure 27 - Diagram of the DUT measurement structure with the buried gate, with a contact width of 3 μm, length of 437 μm, and a square contact pad with a side of 150 μm. 40
Figure 28 - Comparison of the lumped element's inductance and resistance and the extracted parameters of the lumped model when the contacts are made of 5 μm thick copper, the substrate has a conductivity of 10 kΩ.cm, 20 nm thick gold contacts are included, and a 10 nm thick back gate is introduced. 40
Figure 29 - Comparison of the simulated and extracted DUT's characteristics without the backgate and with a 10 nm thick gold backgate. 41
Figure 30 - Comparison of the simulated and extracted DUT's characteristics without the backgate and with a 10 nm thick backgate made of custom material with a conductivity of 2×10^4 S/m. 42
Figure 31 - Pi-model proposed in [71]. 43
Figure 32 - Pi-model used to model the measured graphene devices. 44
Figure 33 - Fabrication of ITO conductivity measurement structures: in (A), the structure's dimensions are shown, and in (B) is shown the fabrication steps as well as the corresponding cross section. 47
Figure 34 - Fabricated ITO contacts on glass substrate in (A), and measured resistance for the thickness of 20 nm for each width in (B). 48
Figure 35 - On top is shown an optical microscope picture of the proposed meander with an aluminum contact, and on the bottom is shown the comparison between having a low conductivity backgate contact and a meander backgate. 49
Figure 36 - In (A) is shown the wafer holder, in (B) is shown the electrical spring-loaded contacts, and in (C) is shown a cross section view of the electrodeposition wafer holder with the arrows depicting the electrical current path. Adapted from [75]. 50
Figure 37 - Fabrication process for the electrodeposition of copper. 51
Figure 38 - On the left is shown the short standard after the lithography and developing as well as its dimensions, and on the right is shown the profilometer measurement of the resist thickness. 51
Figure 39 - Optical microscope images of the electroplating growth of copper before (left) and after (right) O_2 plasma treatment. 52
Figure 40 - Profilometer measurements after performing the growth of copper with 2 mA for 360 seconds. 53
Figure 41 - Profilometer measurement after increasing the exposed growth area with an EBR of 20 mm (left), and after updating the growth parameters while maintaining the 20 mm EBR (right). 54

Figure 42 - Result of wet etching the chromium adhesion layer with chrome etch 18 on the left, and etching the seed and adhesion layer after updating the wet etching process on the right. 55
Figure 43 - Photograph of the H_2O_2 compatibility test on top, and the results for the three metals (gold, copper, titanium) on the bottom. 55
Figure 44 - Photographs of the compatibility test of copper etchant 49-1 with the metals (titanium and gold), showing the metal samples submerged (top) and after the test (bottom). 56
Figure 45 – Graphene images obtained with the optical microscope, and the respective Raman spectra: (A) shows the optical microscope image of graphene on copper, (B) shows the Raman spectra of the graphene on copper, (C) shows the optical microscope image of graphene on silicon, and (D) shows the Raman spectra of the graphene on copper. 58
Figure 46 - Illustration of the copper foil with copper oxide, depicting the growth of large graphene single crystals, as reported in [95]. 59
Figure 47 - Effect of the copper foil roughness on the transferred graphene [95]. 60
Figure 48 - Cross section of the graphite box with the copper foil inside, with the sapphire wafer (source of oxygen), and the graphite spacers. 61
Figure 49 - Pre-treatment of the copper foil, oxidation process, and setup for the growth of graphene flakes. 62
Figure 50 - Optical microscope image obtained with the Raman system on the left, and Raman spectrum obtained on the right. 62
Figure 51 - Optical microscope images showing the effect on the size of graphene flakes when the CH_4 flow is increased in the growth of graphene 63
Figure 52 - Optical microscope images showing the effect on the shape of graphene flakes when the H_2 flow is increased in the growth of graphene 64
Figure 53 - Analysis of the PMMA residues after the graphene transfer for different PMMA mixtures [103]. 66
Figure 54 - Diagram of the graphene transfer procedure. 66
Figure 55 – Extending graphene contact length 5 µm (left) and 35 µm (right) and the difference in graphene contact. 68
Figure 56 - 3D representation of the desired graphene device. 69
Figure 57 - Optical microscope image of the backgate, meander, and contact after depositing SiO_2 and opening the contact. 72
Figure 58 - Optical microscope image after completing the fabrication of the gold contacts. 73

Figure 59 - Evolution of the resistance between two points: outside of the alignment marks between A and A' (approximately 4 cm from the center), and near the edges of the device between B and B' (approximately 1 cm away from the center). 74
Figure 60 - Evolution of the resistance between two points in three different locations: in the substrate, two adjacent copper contacts, and the same gold contact (left); and the evolution of the resistance in those cases (right). 75
Figure 61 - Optical microscope image of the fabricated device after electroplating copper and etching the seed layer, before annealing (left) and a close-up after annealing (right)..... 76
Figure 62 - Optical microscope image of one of the fabricated graphene devices..... 76
Figure 63 - Optical microscope images of the graphene in the DUT area of the fabricated devices..... 77
Figure 64 - Optical microscope images obtained with the Raman characterization system, and the respective Raman spectra for each device, where (A) has a device length of 40 µm, (B) has a device length of 10 µm, and (C) has a device length of 90 µm..... 78
Figure 65 - Diagram of the RF characterization setup (top), and photo of the setup (bottom). 79
Figure 66 - Developed LabView interface. 80
Figure 67 - Fabricated device for graphene characterization..... 81
Figure 68 – In (a) is shown the extracted resistance and in (b) the quantum capacitance of graphene for backgate bias voltages of 0 V, 5 V, 10 V, and 15 V. Fitted lines are shown in red for an easier interpretation of the results..... 82
Figure 69 - Extracted substrate resistance and capacitance. 83
Figure 70 - Extracted paralel capacitance for each device. 83
Figure 71 - Example of the implemented schematic for the extraction of graphene parameters..... 84
Figure 72 - Extracted contact resistance and contact capacitance of the three graphene devices, for the different voltage levels. 85
Figure 73 - Extracted graphene resistance, quantum capacitance, and kinetic inductance of the three graphene devices for the different voltage levels..... 86
Figure 74 – Measured (dots) and modelled (continuous line, through the model in Figure 71) graphene Y21 real and imaginary parameters, in A is shown the real part of Y21 of the device 1, in B is shown the imaginary part of Y21 of the device 1, in C is shown the real part of Y21 of the device 2, in D is shown the imaginary part of Y21 of the device 2, in E is shown the real part of Y21 of the device 3, and in F is shown the imaginary part of Y21 of the device 3. 88

Figure 75 - Measured (dots) and modelled (continuous line, through the model in Figure 71) graphene resistance and capacitance (and inductance), extracted from the real and imaginary parts of Y21. In A is shown the equivalent resistance of the device 1, in B is shown the equivalent capacitance of the device 1, in C is shown the equivalent resistance of the device 2, in D is shown the equivalent capacitance of the device 2, in E is shown the equivalent resistance of the device 3, and in E is shown the equivalent inductance of the device 3 (with an inset showing the equivalent capacitance at lower frequencies). 89
Figure 76 - Extracted resistance (A), capacitance (B), and inductance (C) of graphene at 0 V, per number of squares with a regression of the data. 90
Figure 77 - Dipole antenna designed with graphene to obtain a backscatter readout; the inset shows the area with the graphene, as well as its gate and dimensions. 94
Figure 78 - Results of the simulated antenna showing in (A) the 2D representation of the radiation diagram, in (B) the S11 of the antenna, and in (C) the gain and efficiency of the antenna. 95
Figure 79 – Diagram of the measurement setup on top, and setup used for the measurement of the backscatter of the antenna with graphene on the bottom. 96
Figure 80 – Measured S_{11} in dB of the backscatter by changing the graphene voltage from 0 to 4 volts in the working range of the measurement antenna. 97
Figure 81 - Variation of the S11 for different gate voltages. The graph on the left shows the results for raw data while the graph on the right shows the smoothed (Excel exponential smoothing with a damping factor of 0.8) results for easier visualization. 97
Figure 82 - Measured S11 in dB of the backscatter by changing the graphene voltage from 0 to 4 volts at 4.984 GHz, 5.068 GHz, 5.152 GHz, and 6.226 GHz. 98
Figure 83 - Block diagram of the simulated circuit to attempt to model the measured values. 99
Figure 84 - Results from the simulation of the circuit with the antenna and graphene to measure the backscatter: on the left are the results of S11 for a gate voltage of 0 V and 15 V, and on the right is the resulting difference from both cases. 99
Figure 85 - Steps of the fabrication of the hardmask. 117
Figure 86 - Optical microscope pictures of the patterned hard mask, on the left is shown one of the alignment marks, and on the right parts of the structures are shown. 118
Figure 87 - Raman spectrum of graphene, with the identification of the D, G, and 2D peaks [141]. .. 119

LIST OF TABLES

Table 1 - Planar inductor characteristics of graphene and metal inductors. 28
Table 2 - Capacitor characteristics of graphene and RF MEMS capacitors. 29
Table 3 - Graphene-metal contact resistivity, adapted from [77] 69
Table 4 - Developed fabrication process 70
Table 5 – Equations and calculated constants to fit the graphene elements values for 0 V and 15 V... 91

1 INTRODUCTION

Graphene is a one-atom-thick layer of carbon atoms arranged in a 2D honeycomb lattice. Since its discovery, an increasing number of studies have been published which provide an analysis of its synthesis as well as its physical and electrical properties. The advances made in those areas have allowed for the exploitation of the properties of graphene to integrate and improve electrical circuits [1]. Moreover, large-scale synthesis methods such as Chemical Vapor Deposition (CVD) have provided easier access to graphene, which have increased its industrial interest and have made commercial applications possible.

Part of the interest in graphene derives from its unusual properties. It is a single sheet of sp^2-hybridized carbon atoms, covalently bonded, forming a zero-bandgap semiconductor with relatively high conductivity. Compared to copper with the same thickness, it has lower resistance and can sustain a higher current density than any other known material [1]. Its crucial property in electronic applications is its high carrier mobility, with suspended graphene reaching mobilities up to 200000 $cm^2V^{-1}s^{-1}$ [2], while silicon has an electron mobility of 1400 $cm^2V^{-1}s^{-1}$ [3]. This property makes graphene a suitable material for radiofrequency (RF) applications [4]. The carrier mobility and the charge carrier velocity under a given electrical field are essential features of semiconductor electrical transport. However, as the transistors' gates shrink, the electrical field increases, and the steady-state velocity starts to saturate. At this point, the carrier saturation velocity becomes more critical for the performance of the device, which is not a problem for graphene given that it has an exceptionally high carrier saturation velocity -4.7 x 10^7 $cm.s^{-1}$[5], [6]. Graphene has unusual electronic excitations resulting from a continuous density of states connecting valence and conduction bands, with a singularity at the Dirac point, where the conduction and valence bands meet, and the density of states goes to zero, making graphene sometimes behave as a semiconductor, and sometimes as a metal. Moreover, electron-electron interactions are weak: its electrons are almost insensitive to disorder and have a long mean free path, making graphene exhibit a different behavior from standard metals and semiconductors, being a zero-gap semiconductor, and being often called a semimetal. Another consequence of its gapless density of states is the possibility to modify the free-carrier concentration through the application of electric fields, i.e., through gating. Another way to control the free-carrier concentration is through impurity doping through direct carbon atom substitution or physisorption, layer addition, and external stimuli such as optical stimulation [7], [8]. Some physical properties of graphene make it an excellent choice as a substrate for electronics, such as a high thermal conductivity (3000 W/mK^{-1}), a high Young's modulus of 1 TPa, it can sustain a million times higher

densities of electric current than copper, and silicon compatibility [9][10]. Finally, in biomedical applications, graphene can be functionalized, allowing for the development of biosensors [11], [12], [13], [14]. These properties make graphene a promising candidate for various high-frequency applications, with existing transistors having a cut-off frequency of up to 427 GHz, applications on low-loss interconnects and passives, and even metasurfaces up to 18.9 THz [15], [16], [17], [18]. Further information on the use of graphene in various RF applications is provided in review in [1].

Despite its advantages, it is hard to manufacture graphene devices, given the very particular characteristics of the material. Therefore, some of the most common processes used in conventional Complementary Metal-Oxide-Semiconductor (CMOS) fabrication cannot be employed directly and require adaptation, since some processes such as sputtering can damage the graphene. In other cases, graphene can't be grown directly in CMOS due to the high temperature of graphene growth and rugosity of the substrate. Although it is possible to transfer CVD graphene to a whole wafer, some folds, holes, and cracks can originate from the transfer, thus reducing the graphene integrity [19], [20]. Since the CMOS technology is reaching its performance limit due to the physical limits attained by device downscaling, graphene could be an excellent candidate to integrate silicon, enabling for solutions with novel properties. Some of the drawbacks associated with graphene which need to be overcome, are the following: its low on-off current ratio (which is important for digital applications), induced degraded carrier mobility by the surrounding materials, high metal-graphene contact resistance, and low current saturation, which, for example, decreases the high intrinsic gain in graphene field-effect transistors [21].

This work aims to use the graphene as an enabling element in the design of RF passives to support the design of RF circuitry. It starts with an analysis of the state-of-the-art graphene RF devices, such as inductors, capacitors, and antennas, as well as with the tools for modelling of these components. Then, the implementation of the TRL calibration for the characterization of 2D materials will be analyzed and discussed. Afterwards, the fabrication processes and techniques of graphene and graphene devices will be discussed. In addition to this, through using the implemented calibration and fabrication process, graphene structures were fabricated to extract graphene's properties. These structures also represent how it's possible to implement devices that have tunable resistance and capacitance (or inductance, depending on the structure geometry). Through its tunable properties, an antenna with graphene was fabricated to demonstrate that a backscatter readout could be implemented.

1.1 Motivation

The research on passive RF electronic components that use monolayer graphene is driven by graphene's electrical properties. Through graphene, passive components have the potential to surpass traditional counterparts in terms of speed, frequency response, and power handling. Furthermore, graphene's conductivity across a wide frequency range is another driving force that would allow passive components based on graphene to operate effectively across a broad spectrum of RF frequencies, making them suitable for different RF applications such as wireless communications, radar systems, and high-frequency instrumentation.

Another advantage of graphene is that components can be significantly reduced in size due to the atomically thin nature of graphene, which allows to create compact and lightweight devices. Still, its tunable nature through external stimuli, such as voltage gating, is also another interesting characteristic, since that allows to develop reconfigurable RF components. The tunability of graphene isn't limited by voltage gating and can be achieved through other methods. An example of such methods is through functionalization. This allows to include elements in the surface of graphene that allow to detect different types of molecules, allowing to implement graphene biosensors. Since it's possible to fabricate graphene biosensors and graphene has tunable properties, it would be interesting to develop graphene biosensors with wireless readout.

Furthermore, although it is required to adapt the current fabrication processes (such as for CMOS) graphene can be integrated with existing semiconductor technologies, fabrication processes, and techniques, making it compatible with current electronics nanofabrication techniques. This could also facilitate the integration of graphene-based passive components into current RF systems and circuits. Additionally, an increasing demand for high-performance RF components due to developments in new areas such as 5G, IoT, autonomous vehicles, and wearable electronics increases the pursuit for new solutions in which graphene-based passive components can be a part of.

The development of graphene components, however, still has several obstacles that must be overcome. The development of passive RF electronic components, using monolayer graphene, is challenging due to the need to obtain high-quality monolayer graphene, and seamlessly integrating it into RF components. Current methods, like CVD can introduce defects and impurities, which have an impact on the performance of the components. Although it is possible to integrate graphene-based components with existing semiconductor fabrication techniques, it is still necessary to adjust current design and

manufacturing approaches. To add to this problem, the scalability and cost-effectiveness of producing high-quality monolayer graphene, while being affordable, is also still challenging.

Although there is a vast activity in active graphene electronic components, the development of passive elements is also required [22], and still requires special attention [23] to enable complete devices to be implemented. With the increase on graphene research, it becomes apparent that, in the near future, circuits that make use of the graphene's characteristics and at increasingly smaller scales will be needed. In [24], for example, an RF sub-circuit that is based in graphene is presented and, although it uses CVD grown graphene, it was not used to increase the device's performance through the use of passive elements. A possible explanation would be the existing difficulty in designing the various sub-systems and interconnections in graphene. Moreover, with the development of graphene devices, it still is necessary to extract its intrinsic properties. Graphene transistors, for example, have been reported to have a unity current-gain cut-off frequency of 300 GHz, which is limited in many devices due to external contacts [15] (extrinsic characteristics). This means that intrinsic parameters must be extracted to measure the performance of graphene components.

Passive elements are essential in an RF circuit given that, ultimately, those are the components that limit its performance. Alike main elements, there are simple interconnections (that define maximum currents and circuit parasitics), resistors (that condition the system's performance), capacitors and inductors (whose Q factor and tolerances are key elements), and waveguides (whose losses should be controlled). Designing such circuits in graphene with currently available tools and methodologies, however, is still a limiting factor, that is aimed to be tackled. Therefore, it is currently difficult to predict the behavior or performance of graphene passive devices, which ultimately limits their implementation on electronics.

1.2 Objectives

The development of new wireless graphene sensors depends on how easy it is to conceive systems that are entirely based on graphene. In its current state, circuit design, even for passive elements, is very close to the material's physics, which prevents a higher adoption of such systems from occurring. Furthermore, some of those passives don't have the necessary characteristics for the implementation of a complete system yet. This leads to the need for more research [25], so that graphene sensors technology can be more accessible and optimized.

In conventional RF CMOS technologies, the circuits engineer selects the design kit that is associated to the technology that he's working on and can, with high levels of confidence, obtain an RF system within the desired characteristics. In other cases, where electromagnetic elements are involved, it may be needed to resort to FEM or FDTD tools. However, it is still possible to predict the performance of such systems with enough accuracy. As for graphene, the literature shows that conventional tools have difficulties in predicting its performance. Due to these problems, the objective of this work is to contribute to the state of the art of this extremely promising area, with the aim to reduce modelling and simulation difficulties and to aid in the future development of graphene passive circuits for radiofrequency biomedical sensors.

This work aims to:

-Extract and model graphene's characteristics, allowing to evaluate graphene's RF properties for a given fabrication process;

-Measure graphene properties, allowing to integrate them onto electronics schematic simulator, thus facilitating the simulation and development of graphene RF passive devices and systems;

-Design, implement, characterize, and model RF graphene passive elements;

-Demonstrate the integration of graphene on the development of some of the most basic radiofrequency system's blocks.

1.3 Main contribution

The contributions presented in this thesis address the problem of designing graphene RF passive components. To improve the design of these components, increasing the knowledge on graphene and its RF applications was targeted. Due to the multidisciplinary nature of developing RF electronics based on graphene, this work required working on and interconnecting different engineering areas such as RF electronics, nanotechnology, and microfabrication.

The main contributions on extracting graphene RF properties were:

-Implementing and testing the TRL calibration to characterize graphene, which is a widely adopted, standard calibration technique. This allowed to obtain the desired parameters to characterize graphene, while considering the various fabrication constraints regarding the integration of 2D materials. "Extraction of Graphene's RF Impedance through Thru-Reflect-Line Calibration";

-Integrate the calibration structures together with monolayer graphene devices in the same fabrication run. Through this process it was possible to integrate structures with back gate that allow to

characterize graphene (a 2D material), achieving a yield from around 40% up to 55%. “Extraction of Graphene’s RF Impedance through Thru-Reflect-Line Calibration“;

-To extract the RF properties of monolayer graphene for different chemical potentials (from 0 V to 15 V) through a buried gate (50 nm SiO_2 dielectric). This was performed from 1 GHz to 8.5 GHz, for a 50 µm graphene width, through using lengths of 10 µm, 40 µm, and 90 µm;

-Integrate the extracted graphene properties into electronics simulators such as Keysight ADS and Cadence AWR, through using lumped elements;

-To implement a test case where graphene was integrated onto a metallic antenna, allowing to demonstrate a backscattering device with tunable properties.

-To demonstrate that it is possible to approximate the behavior of such devices through graphene modelling and parameter extraction. This verification can support future developments of wireless, minimally invasive sensors.

Through this work, various oral presentations were originated, as well as the following publications:

- V. Silva, I. Colmiais, L. Baptista, J. Borme, P. M. Mendes, P. Alpuim, “Towards graphene based RF devices”, JORNADAS CF-UM-UP 2019, Centro de Física das Universidades do Minho e do Porto, Portugal, December 13th 2019;

-I. Colmiais, J. Borme, P. Alpuim, P. M. Mendes, "Graphene LC oscillator for biosensing applications", 2021 XXXVI Conference on Design of Circuits and Integrated Systems (DCIS), 24 November 2021.

-Ivo Colmiais, Vitor Silva, Jérôme Borme, Pedro Alpuim, Paulo M. Mendes, "Towards RF graphene devices: A review", FlatChem, Volume 35, 2022, 100409, ISSN 2452-2627, doi: 10.1016/j.flatc.2022.100409.

- Colmiais, I.; Silva, V.; Borme, J.; Alpuim, P.; Mendes, P.M. Extraction of Graphene’s RF Impedance through Thru-Reflect-Line Calibration. Micromachines 2023, 14, 215. https://doi.org/10.3390/mi14010215

-Diogo Baptista, Ivo Colmiais, Vitor Silva, Pedro Alpuim, P. M. Mendes, “2D Electronic circuits for sensing applications”,“Graphene Field-Effect Transistors: Advanced Bioelectronic Devices for Sensing Applications, Omar Azzaroni, Wolfgang Knoll John Wiley & Sons, Limited, Dec 27, 2023” https://books.google.pt/books/about/Graphene_Field_Effect_Transistors.html?id=MchqzgEACAAJ&redir_esc=y, September 2023

1.4 Thesis outline

In the first chapter, graphene for RF passive devices is introduced as well as its general characteristics, the motivation, objectives and main contribution of this work.

Then, the second chapter focuses on reviewing the literature on graphene passive components for RF electronics as well as current modelling techniques. This allows to demonstrate the current state of graphene passive RF electronics and that further effort is necessary in the extraction of graphene's properties and in characterization and modelling of graphene devices.

The third chapter discusses the extraction of graphene RF parameters through the implementation of the TRL calibration. Although it is a commercialized and well-known calibration, its application for 2D materials such as graphene and corresponding hurdles hadn't been explored yet. These materials require the supporting/contacting structures to have certain characteristics that influence the calibration accuracy. This chapter allowed to demonstrate these hurdles, analyze and implement the calibration, determine the requirements for its use in the characterization of graphene, and discuss the extraction of its parameters.

Chapter four discusses current graphene fabrication and characterization methods. Moreover, it discusses the importance of large graphene single crystals and their fabrication. Since graphene is grown in a separate substrate, its transfer to the target substrate is presented as well as the metallic contacts composition. Moreover, the fabrication of graphene devices as well as their fabrication process are discussed. The fabrication is described step by step, and the device is characterized, demonstrating that the requirements for the calibration of graphene are fulfilled.

Chapter five is the combination of the previous chapters, using the simulated and fabricated TRL calibration for the characterization of graphene, and using the fabricated graphene devices. Through this, it was possible to implement a measurement setup, measure, and characterized graphene's characteristics.

Chapter six makes use of the previously determined graphene characteristics to fabricate a device that could mimic a graphene biosensor with backscatter RF readout. This chapter focuses on discussing the wireless readout working principle and on the design of the backscatter antenna. The results of the measurements of this antenna with integrated graphene are reported and modelled.

Finally, chapter seven presents the conclusions of this work and possible future work opportunities.

2 GRAPHENE RF PASSIVE ELEMENTS

On-chip metal inductors have revolutionized radiofrequency electronics. However, their inductance density values are limited on account of their inherent scalability limitations, hindering continuous performance enhancement, meaning that further improvements could be achieved through researching other material's characteristics. Moreover, in some cases, planar inductors can occupy up to 50% of an RF-IC chip area, meaning that they are the largest contributors of IC's area [26]. The need to increase inductance density values made it become necessary to use new approaches. Thus, graphene has been suggested as a solution to this bottleneck, through the study of its large kinetic inductance, high conductivity, and small footprint [1], [15], [26], [27], [28].

Magnetic inductance is the property by which the current flow through a conductor generates a magnetic field around it. A time-varying current creates a time-varying magnetic field, which in turn induces an electromotive force in the circuit (self-inductance). When the magnetic field lines cross nearby circuit loops, these become inductively coupled, and a similar effect occurs (mutual inductance). On the other hand, the kinetic inductance is influenced by the inertial mass of the charge carriers when these are subjected to an alternating electric field. The manifestation of this behavior is an equivalent series inductance. It becomes clear that the magnetic inductance is defined and influenced by the geometrical design of the conductor, while the properties of the material influence the kinetic inductance.

Planar inductors have primarily relied on design improvements since the kinetic inductance in conventional metals is negligible. In contrast, the use of high kinetic inductance materials makes it possible to increase the total inductance of the component. It has been demonstrated that it is achievable to increase the inductance density and the quality-factor of the inductors when compared to conventional inductors [26]. Therefore, the literature suggests that by using graphene it should be possible to help overcome the current on-chip inductors' limitation. If integrating graphene while increasing the performance, flexibility, and integration becomes feasible, it should allow to improve electronic circuits as well as wireless communication systems.

Carbon nanomaterials are attractive due to their significant momentum relaxation time, meaning that a sizeable kinetic inductance can be obtained, which is comparable to the magnetic inductance [26]. This leads to increased inductance and area efficiency, further improving the performance of the inductor [26].

Graphene capacitors are still being explored, with application in biosensing [11], [29]. It is achieved by immobilizing surface receptors on the surface of the graphene capacitor, which, upon recognizing the

target molecules, changes the interface capacitance. Consequently, the graphene's surface charge density changes, which can be detected by measuring its conductance. These capacitors rely on the series association of the interface capacitance with the graphene quantum capacitance to create a graphene varactor, with its capacitance modified through the exposure to the target analyte, an effect called local gating [29]. Although graphene's RF characteristics for capacitors have neither been well defined, nor studied yet, some works claim that graphene is an excellent candidate, on account of its quantum capacitance and tuning possibility[30], [31], [32]. The latter is often achieved by biasing the RF signal with a DC voltage, which changes the carrier density in graphene [30]. The use of graphene capacitors has been proposed due to an increased tuning range when compared to microelectromechanical system (MEMS) capacitors, low control voltage, and smaller size [30], [31], [32].

In addition, rapid advancements in graphene industrial-scale fabrication, potentially cheaper processes (compared to MEMS) are being developed, and lower packaging requirements have been obtained. Finally, they can also outperform Metal-Oxide-Semiconductor Capacitors (MOSCAPs) at high frequencies. Consequently, the use of graphene capacitors has been proposed, with possible applications in voltage controlled oscillators, tunable filters, impedance matching, and phase shifters [31]. One of the parameters that can be used to evaluate the performance of electrical components, which will be used to compare inductors and capacitors, is the quality-factor (Q-factor, or Q). It is a dimensionless number that corresponds to the ratio of energy stored to energy dissipated. Therefore, it can be directly related to the undesired series resistance of inductors and capacitors, meaning thar higher series resistance is undesirable, and originates a lower Q-factor component.

The introduction of carbon materials has also been accomplished in antennas, where graphene and other nanomaterials improve future electronics and telecommunication technologies, where it has been proposed and explored for THz applications. In this case, graphene is used as a single layer or in composites with metal nanoparticles so as to maximize electrical conductance. For THz antennas, graphene has been chiefly used for modeling, simulation, and theoretical predictions. Still, the simulation process and the demonstration of the theoretical predictions are very intricate [33]. Although single-layer graphene holds a relatively high sheet resistance, it has the advantage of having a tunable conductivity through its dependence on the electron chemical potential, which can be controlled by DC biasing. This property can then be used to obtain controllable radiation characteristics, which allow for different radiation patterns and antenna states to be obtained [34], [35], [36].

In view of the exciting properties of graphene, a more in-depth analysis of its application in RF components will be provided.

2.1 Graphene inductors

In [26], multilayer graphene (MLG) is proposed since it ensures that graphene's significant quantum contact resistance can be lowered. However, using MLG has challenges associated with it, namely: much lower conductivity compared to conventional metals and the interlayer coupling, which reduces the charge carrier inertia (and consequently the kinetic inductance). The above-mentioned work reports an on-chip inductor based on intercalated MLG that overcomes the scalability challenge of metal inductors. The authors have resorted to bromine intercalation to tackle the described challenges so that the MLG's conductivity may be increased, and the interlayer coupling can be reduced (increasing the kinetic inductance). With this technique, it is claimed that quality-factors (Q-factors) of up to 12 and 1.5-times higher inductance can be achieved in a two-turn inductor, when compared with its copper counterpart. Although good results have already been achieved, the authors claim that the results can be improved by increasing the contact quality and improving the intercalation technology. For the latter, it is proposed that various compounds be used as dopants for the intercalated MLG, such as alkali metals (Li, Na, and K), halogens (Cl_2, Br_2, and ICl), and halides (BF_3, AsF_5, $AuCl_3$, and $FeCl_3$). Finally, as shown in Figure 1, three kinds of inductors were fabricated, and their respective Q-factors and inductances were measured. The narrow square presents the best result, achieving an inductance of around 1.2 nH between 5 GHz and 40 GHz, a maximum Q factor of 11 at 30 GHz, and around 6 at 40 GHz. The area is 40000 μm^2, achieving an inductance density of 40 nH/mm^2.

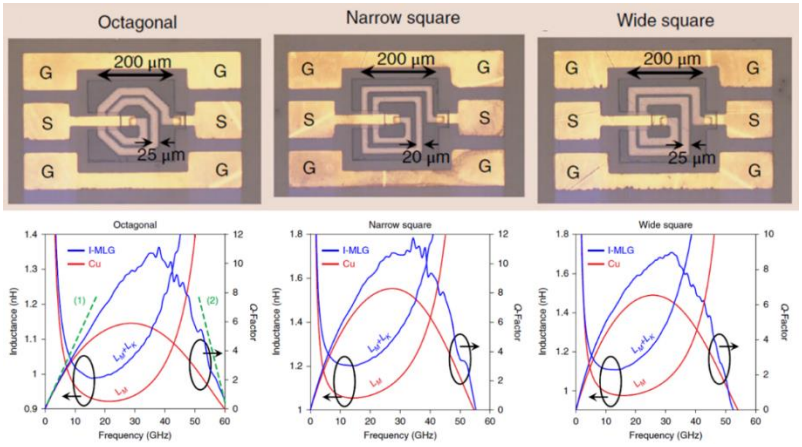


Figure 1 - Fabricated graphene inductors (in octagonal shape, narrow square, and wide square) and their respective inductance and Q-factors [26].

In [15], ¾-, 2-, and 3-turn graphene inductors were fabricated, as shown in Figure 2, along with their characteristics in the range 0 - 60 GHz. Various analyses were performed on the substrate and substrate dielectric so that the inductors' Q-factor could be improved, with the extracted model and the

characteristics of the device displayed in Figure 3. Low-loss substrates increase the Q-factor from 5 to 10 (4 mΩ.cm to 10 Ω.cm) in the range of 10-100 GHz. In the design of the authors, SiO_2 substrates allow for higher Q-factors than Si_3N_4 and Al_2O_3 in the range of 20-100 GHz, increasing from 6 to 10 [15]. A 2 μm-thick substrate dielectric improves the Q-factor from 10 to ~25 in the range of 50-300 GHz. The authors of the aforementioned work have also concluded that their graphene inductors exhibited skin-effect [26].

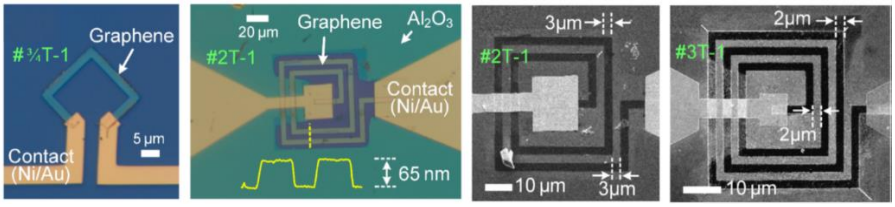


Figure 2 - Fabricated graphene square inductors with ¾-, 2-, and 3-turns, presented in [15].

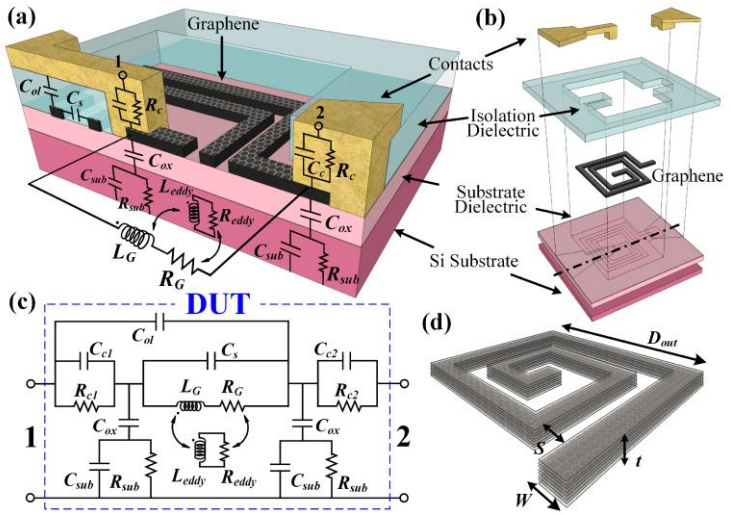


Figure 3 - a) Schematic of the graphene spiral inductor with the equivalent circuit parameters. b) Is the exploded view of a). c) Is the equivalent circuit model of the device presented in a). d) is a schematic view of the graphene inductor [15].

Furthermore, the authors claim that the Q_{max} and f_{op} can be optimized through dielectric engineering by reducing the inductor's operating frequency. Additionally, they have further increased (duplicated) the inductor's Q-factor through annealing, reducing the contact resistance from 356 Ω to 318 Ω. The fabricated inductors achieved highest Q-factor is 3 for a ¾-turn inductor, at a frequency of 40.8 GHz, with an inductance of 0.15 nH. The highest inductance is 0.66 nH for a ¾-turn inductor, with a Q-factor of 2.75 at 40.2 GHz. These inductors have areas of 576 μm^2 and 400 μm^2, corresponding to an inductance density of 0.26 $pH/\mu m^2$ and 1.65 $pH/\mu m^2$, respectively.

The Q-factors of CVD monolayer graphene and graphite inductors have been evaluated in [27] showing that the relatively high resistance of graphene causes negative Q-factors throughout the whole frequency range, meaning that graphene's resistance must be decreased, as stated in previous reports. The approach taken by the authors consisted in using graphite due to its lower resistance. Moreover, they conclude that the contact resistance is an essential factor that negatively influenced the inductors' Q-factor. They have achieved a measured maximum Q-factor of 2.36 at 67 GHz, with a calculated Q-factor of 6.46 at around 160 GHz. These results are shown in Figure 4, along with the fabricated inductor.

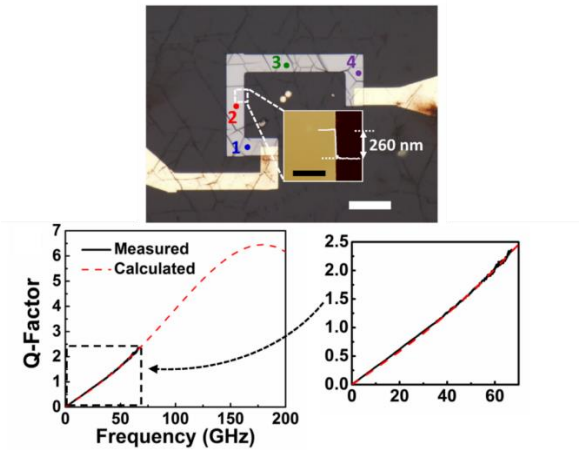


Figure 4 - Fabricated ¾ turn graphene inductor, and measured Q factor until 67 GHz and predicted until 200 GHz [27].

In [28], a study of the behavior of graphene up to 67 GHz was provided. According to the results of the measurements, the graphene square resistance is 798 Ω, and the kinetic inductance is 2.4 nH. From the measured results, it is concluded that the total inductance is 3.6 nH.

Graphene has been used for the fabrication of inductors, and their characteristics have been analyzed. These works significantly concur that the high resistance of graphene must be reduced in order for it to be used in inductors. On the other hand, graphene has various advantages when used for RF inductors, such as: increased inductance than its metal counterpart due to the added kinetic inductance and reduced inter-turn capacitance due to the minimal thickness of graphene compared to metal.

In [37], the authors have used electrophoretic deposition to develop an inductor with graphene. The graphene was prepared in a solution of acetone, ethanol, $Mg(NO_3)_2$, $Zn(NO_3)_2$, and $Al(NO_3)_2$. This solution was used to provide charge carriers and improve the performance of the device. Then, copper was sputtered on top to complete the inductor with doped graphene. The developed inductor is shown in Figure 5.

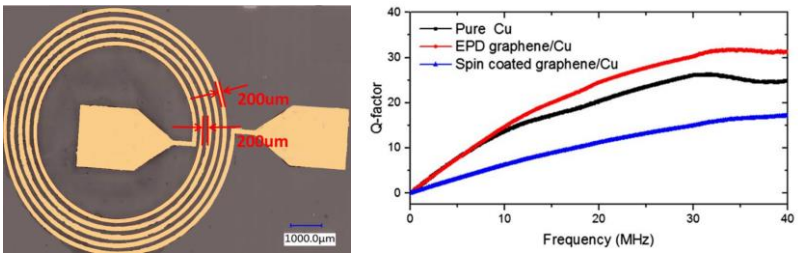


Figure 5 - Fabricated doped multilayer graphene inductor through electrophoretic deposition on the left, and Q factor on the right [37].

The inductors were characterized up to 40 MHz and exhibit a larger inductance and Q-factor in comparison to the pure copper version. The Q-factor of the copper version is 26.2, while the graphene and copper has a Q-factor of 30.3.

2.2 Graphene capacitors

In [29], a variable capacitor that senses glucose through the quantum capacitance effect is demonstrated. It uses a metal-oxide-graphene structure to implement a varactor that is compatible with passive wireless sensing. The capacitor's graphene was functionalized, which allows for the detection of the glucose in the solution, thus revealing its concentration and modulating the level of electrostatic doping of the graphene surface, leading to a capacitance change. The fabricated capacitor is shown in Figure 6, where a perspective and a microscopic view are displayed. The obtained capacitance values can be observed in the same figure. Although these were analyzed to measure its change through the glucose concentration, it is possible to observe that the capacity changes by modifying the DC bias. These values were measured with a 50 mV RMS, 1 MHz AC signal.

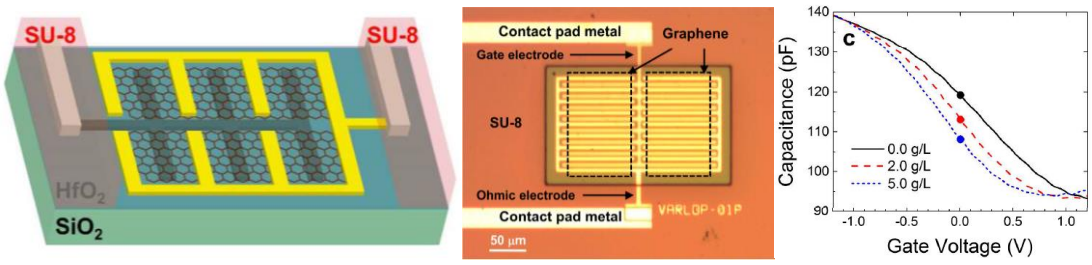


Figure 6 - Diagram of the capacitor (left), and microscope image of the fabricated graphene biosensing capacitor (center) and capacitance value for different glucose concentrations (right) [29].

In [30], graphene quantum capacitors are proposed and characterized. These are also tunable by controlling their charge density and can be used in tunable LC tanks. The authors claim a tuning range

of 1.3:1, achieved within a 1.25 V range with Q-factors up to 14.5 at 0.4 GHz. The capacitance density obtained was 2.65 fF/μm², being 100 times higher than RF MEMS. The implemented structure consists of two symmetrical capacitors placed on a CPW so that they could be characterized. Figure 7 represents this structure, where it is also demonstrated how to bias the capacitor and tune its capacitance. This design uses a multi-finger approach in order to make it possible to increase the capacitance while reducing graphene's parasitic resistance.

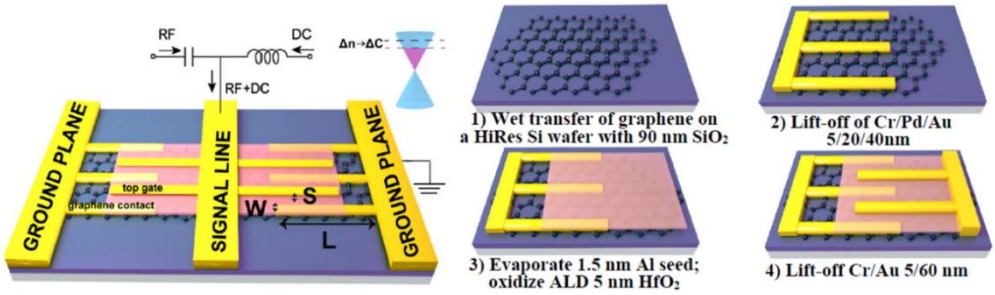


Figure 7 - Proposed tunable LC tank with a graphene capacitor (left) and fabrication steps of the device, including the graphene transfer, metallic contact patterning and oxide deposition through evaporation (right) [30].

The measured capacitance values and the Q-factor are displayed in Figure 8. It is possible to observe that the capacitance value can be changed through the applied bias. The low tuning voltage of these capacitors allows for low power ICs to be developed, and according to the authors, these capacitors have the advantage of a simplified fabrication process and can outperform alternative technologies' Q-factors at high frequencies. Although the maximum Q-factor is 15 at 0.4 GHz, the authors claim that it is possible to increase this value through simple design changes, predicting a maximum Q-factor of 200 at 5 GHz.

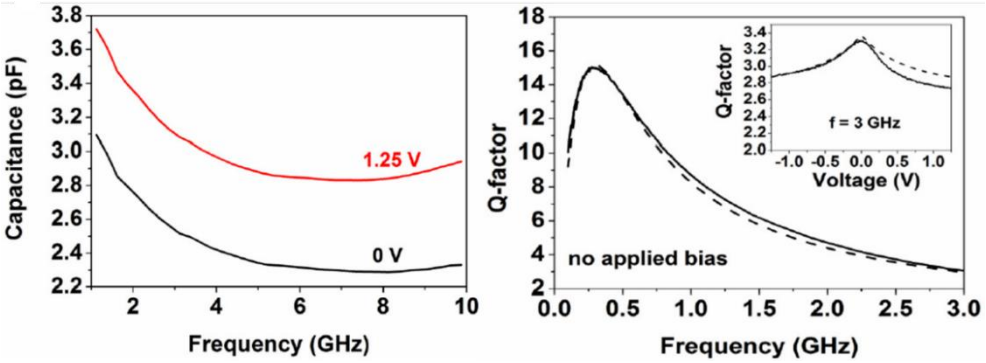


Figure 8 - Capacitance (left) and Q-factors (right) of the fabricated graphene capacitor [30].

The same kind of graphene capacitor is further explored in another work published by the same authors [31]. The capacitor is proposed to have a CMOS compatible fabrication process, and its performances were examined up to 10 GHz, achieving Q-factors up to 12 at 1 GHz. In this work, various

devices were fabricated with different dimensions so that their effects could be studied. These included modifying the number of fingers as well as their length. Findings show that by reducing the finger length, the Q-factor is increased due to the reduced series resistance, and also that the number of fingers doesn't significantly influence the Q-factor.

Moreover, this study concludes that the capacitors can be scaled to any capacitance by modifying the number of fingers without impacting the Q-factor. Subsequently, temperature tests were carried out showing a capacity dependence of temperature near the Dirac point. However, if operated further from it, there is little dependence on temperature (150 K to 350 K), and superior values are obtained when compared to MEMS and semiconductor variable capacitors. Further optimization was sought after the results for the fabricated capacitors were obtained. Through simulation, the authors have further improved some parameters to increase the Q-factor of the capacitor. Consequently, through this optimization, Q-factors of 44 at 1 GHz, 122 at 5.3 GHz, and above 50 from 1.1 GHz to 24.8 GHz were achieved. The results of the effects of the design parameters are displayed in Figure 9.

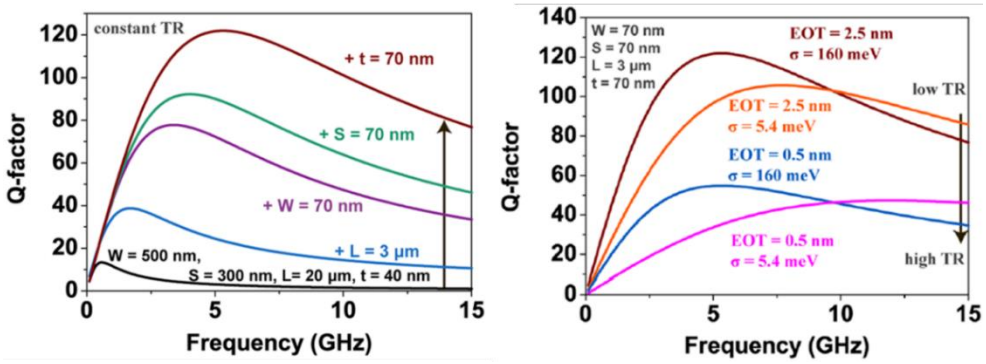


Figure 9 -On the left, the effects on the Q-factor by modifying the capacitors parameters are plotted: L - length of fingers, W-width of fingers, S-spacing, t-thickness; the image on the right depicts the effects on the Q-factor by the equivalent oxide thickness and disorder in graphene (Dirac point) [31].

An intercalated multilayer graphene capacitor is proposed in [38], and the diagram of the capacitor is displayed in Figure 10. The authors claim that a Q-factor higher than 20 was achieved, which has a tuning ratio up to 4.74%, by applying a bias of 0.8 V. In this proposal, the graphene was intercalated with hexagonal boron nitride (hBN), which improves its in-plane conductance due to its atomically smooth surface and fewer charge taps. After that, the graphene layers were modeled as conductive, the hBN layers as insulating, and the interlayer tunneling was neglected due to the decoupling caused by the hBN. Although the capacitor is proposed to function as a resonator in the THz range, the same concept could be explored for capacitors in the GHz range.

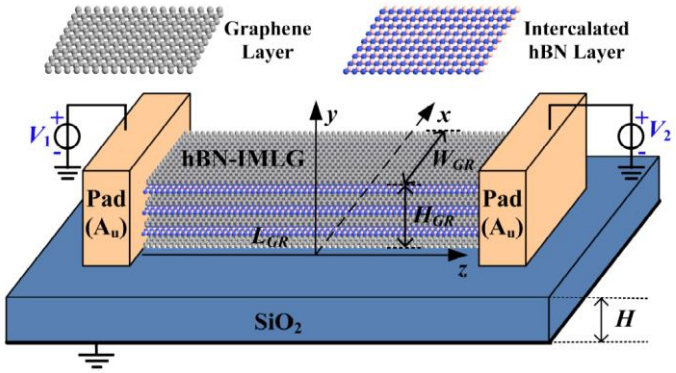


Figure 10 - Proposed capacitor with intercalated graphene and hBN layers, where graphene was modelled as a conductor and hBN as insulator, for the THz range [38].

A graphene capacitor, used in a tunable LC resonant tank, is presented in [32] and its tunability is achieved by exploiting the properties of graphene. The authors focus on the fabrication of the capacitor while the inductor was added externally. The graphene used in this device is exfoliated onto a substrate, and the dielectric is 10 nm thick hBN. Afterward, the contacts were deposited and patterned. The mentioned structure is displayed in Figure 11, which depicts the capacitance tuning ability of such capacitors.

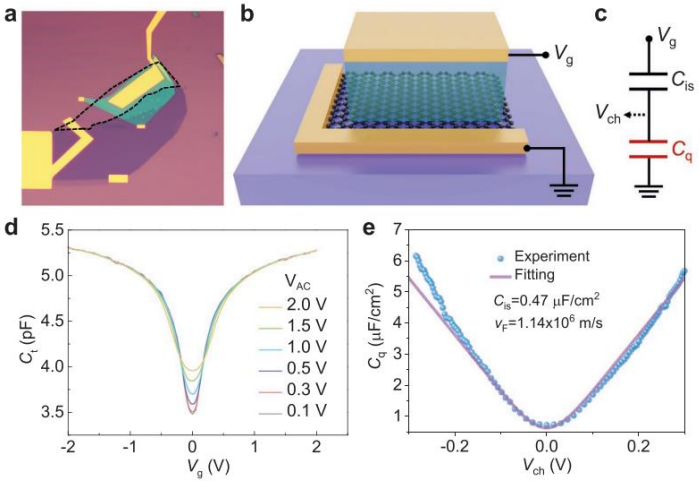


Figure 11 - a) Optical image of the fabricated capacitor. b) conceptual and schematic drawing of the graphene capacitor. c) equivalent circuit of the graphene capacitor. d) capacitance dependence on bias voltage and AC signal voltage. e) experimental and theoretical quantum capacitance of the device.

This device has a minimum capacitance of approximately 3.5 pF and a maximum capacitance of approximately 5.25 pF. The authors added a 2 mH inductor in series to implement a resonant tank and managed to get a tunable tank from 1.45 to 1.73 MHz. The capacitor had a tuning ratio of 1.53:1 with a control voltage of 2 V. However, the authors claim that a theoretical tuning of 8.3:1 with a low control

voltage of approximately 0.3 V can be achieved. In comparison, MEMS capacitors can have a tuning ratio of over 8:1 but require a tuning voltage of over 5 V. In the case of varactors, the tuning ratio is approximately 2:1, with a control voltage of around 1 V. Therefore, graphene capacitors offer an alternative technology with high tuning ratio and low control voltage that is compatible with CMOS.

2.3 Graphene antennas

The design of graphene antennas for higher frequencies was accomplished in [33], where a patch antenna for terahertz was simulated in CST, and graphene was modeled through Kubo formalism. In that case, a micrometer size and high far-field gain antenna was the intended result. In the abovementioned work, a transparent graphene antenna was proposed, as displayed in Figure 12, whose graphene patch measures 60 µm * 100 µm, resonates at 1 THz and has got a gain of approximately 5 dB. Moreover, it also delves into the influence of the chemical potential of graphene on the resonant frequency of the antenna. In order to obtain such control, polysilicon gating pads were placed under the graphene sheet, thus allowing for the application of a DC bias. This allowed for a predicted tunability range between 960 to 1030 GHz. The authors have also claimed that the graphene antenna outperforms its metallic counterpart in spectral characteristics. In addition, graphene antennas can be more advantageous given that the performance of metallic film antennas can be affected by microcracks.

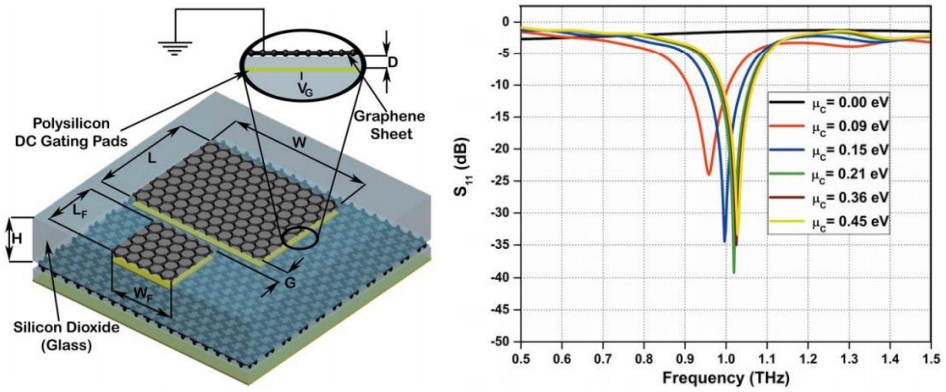


Figure 12 - Proposed graphene patch antenna on the left, and its tunability range on the right [33].

A graphene dipole is proposed in [39], where simulations in CST were used to analyze the influence of different substrates. For the simulations, Quartz-Silicon, GaAs-Silicon Nitride, and Polyimide-Glass were used, presenting thicknesses ranging from 80 to 120 µm with a step of 20 µm, as shown in Figure 13. With a targeted frequency of 1.02 THz, the 100 µm Quartz-Silicon substrate provided the best performance. At 100 µm, the best return loss of -45.5 dB, with a bandwidth of 0.11 THz, -14.76 dB

efficiency, and a directivity of 3.86 dBi was achieved. Still, using graphene has the drawback of having a low radiation efficiency due to its high resistance, when compared to metals in micro and mm-waves, but this is compensated due to its tunability properties.

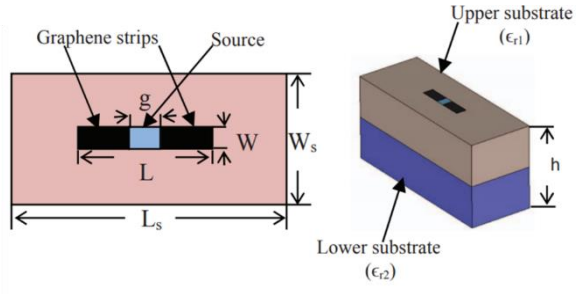


Figure 13 - Diagram depicting the graphene dipole proposed in [39], with the antenna design as well as substrate structure.

A "smart graphene antenna" for terahertz is proposed in [34] and simulated in HFSS, where graphene was modeled through the Kubo formalism. It has an approximate total length of 53.5 μm, and width of 26 μm. It can operate as an omnidirectional dipole and has a reconfigurable radiation pattern that is operated through chemical potential modification. Its operating range varies between 1.94 and 2.13 THz and offers four states that are used to modify its radiation pattern, with the maximum gain of -0.91 dBi, and one of them corresponding to "off". In this design, the authors have managed to increase the gain of the antenna in 2.13 dB through the introduction of graphene parasites, as shown in Figure 14.

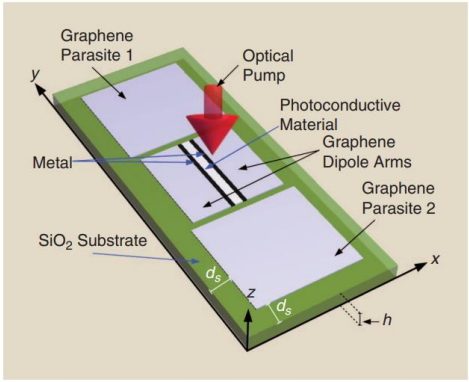


Figure 14 - Proposed graphene dipole that includes two additional graphene parasitic structures to reconfigure the antenna's radiation pattern, proposed in [34].

Studies such as the one provided in [40] for terahertz graphene antennas are being undertaken, providing an analysis of different structures through simulation, and modeling the graphene conductivity through Kubo formalism, as shown in Figure 15. Five structures were tested: a dipole, a fractal dipole, a spiral, a bow-tie, and a log-periodic antenna. The dipole (80 μm * 270 μm) had a directivity of 2.51 dBi at 0.834 THz and a bandwidth of 0.201 THz, with a second resonant frequency becoming more

appreciable when its width is reduced. From all the antennas, the log-periodic antenna achieved the highest directivity of 3.08 dBi and a bandwidth of 2.77 THz, but with the lowest radiation efficiency of 86% and largest occupied area (350 µm * 390 µm).

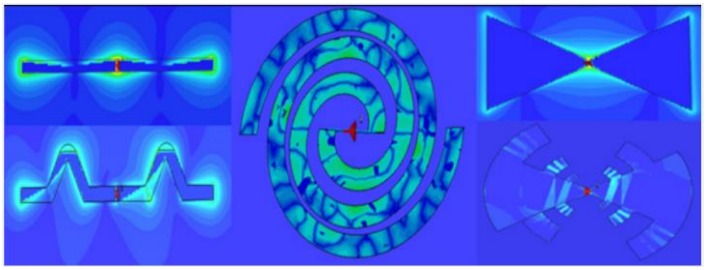


Figure 15 - Designs and simulation in CST of different THz antennas proposed in [40].

In [35], an electronically beam scanning THz antenna is proposed, simulated, and analyzed, as shown in Figure 16. The leaky-wave antenna performs beam scanning at a fixed frequency and is composed of a graphene sheet, which was modelled through Kubo formalism, that can be transferred onto a back-metallized substrate. Polysilicon was used to build a set of DC gating pads beneath so that graphene's conductivity can be modulated, and the leakage rate can be dynamically controlled. This is achieved through applied DC voltages to the gates so that the beam scanning capabilities can be obtained. The antenna exemplified in the paper had a 60 µm SiO_2 substrate, a very large graphene sheet with a width of 200 µm (to support the propagation of surface plasmon polaritons), a required reactance of 1302 Ω/sq (which can be tuned through the DC bias), and biasing pads with the width of 4.8 µm and spacing of 0.2 µm. Through these configurations, 4 beams could be generated at -45.5°, -9.3°, 15.4°, and 37.5°. This antenna, however, has a minimum operating frequency of around 0.5 THz, and the radiation efficiency is always dependent on the graphene quality such as the other graphene antennas. Finally, the fabrication steps for such an antenna can be carried out through existing microfabrication procedures.

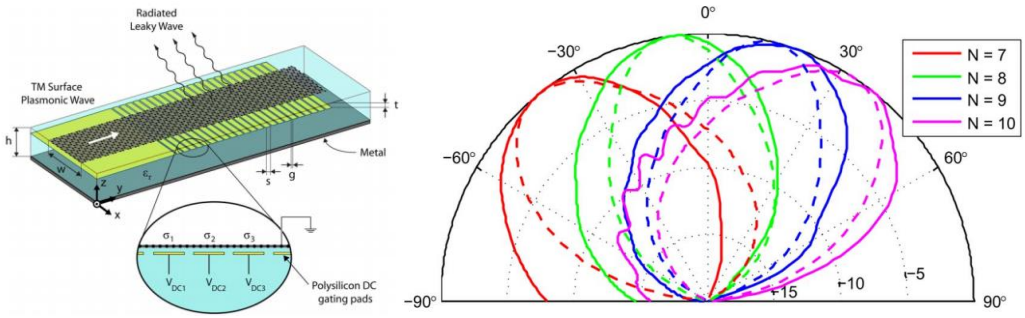


Figure 16 - Proposed graphene leaky-wave antenna (left) with beam scanning capabilities for THz and radiation patterns (right) [35].

Another form of implementing a graphene antenna is proposed in [41], which resorts to plasmon induced doping of graphene through laser excitation. An antenna with nine sub-units was fabricated, and joined with a graphene sheet, as shown in Figure 17. This forms a phototransistor that works through the photoinduced n-doping of graphene, which is caused by hot electrons that are plasmon generated by laser excitation. This phenomenon can be seen through the shift of the Dirac peak when the wavelength of the laser is changed. The doping efficiency becomes larger for the n-type graphene when in comparison with the p-type graphene. This hybrid antenna-graphene photodetector can achieve an 800% photocurrent enhancement with a 20% internal quantum efficiency with the detection being done through the electric current, since hot electrons can transfer directly into the conduction band. The photocurrent of the device can be actively tuned through gate biasing. This structure was fabricated and reported in [42] and is displayed in Figure 17.

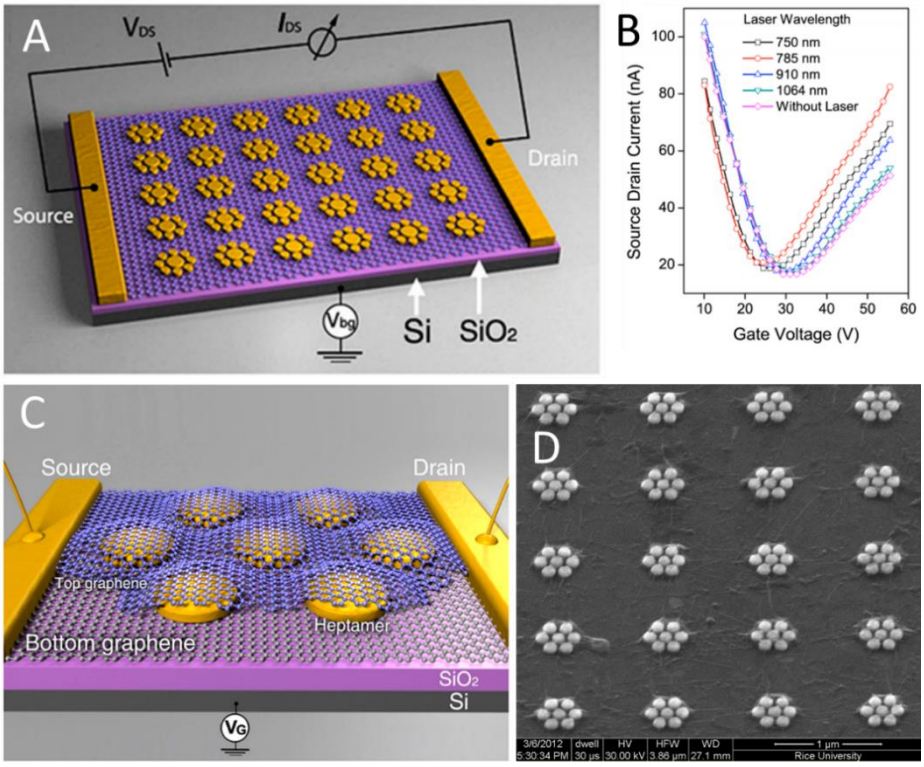


Figure 17 – A) proposed plasmon-induced graphene antenna with a nonamer array. B) dirac point shift with the wavelength. C) simplified proposed plasmon-induced graphene antenna with a heptamer. D) Scanning electron microscope image of the fabricated plasmon-induced graphene antenna [41], [42].

In [36], a GHz and a THz antenna that are based on graphene are proposed and simulated. The authors have demonstrated that metallic dipole antennas or arrays can benefit from graphene's ability to change from high to low resistivity. This can be directly controlled through a bias voltage and modify the radiation pattern and efficiency of the antennas. The proposed antennas are made on top of SiO_2/Si

substrate, graphene is deposited on top of it, and then a 2 μm thick gold layer is deposited. The proposed antenna has a width of 100 μm, a length of 1000 μm and a gap of 50 μm, as displayed in Figure 18, and works at 120 GHz. The authors can use graphene to switch from a high to a low resistance state and turn the antenna "on" or "off", thus obtaining a directivity of 2.18 dBi in the "on" state, with a radiation efficiency of 94.61%. Since the radiation pattern can be controlled through the application of a gate voltage, the authors have used this for the THz antenna, scaling this effect to an antenna array and controlled the array's radiation pattern.

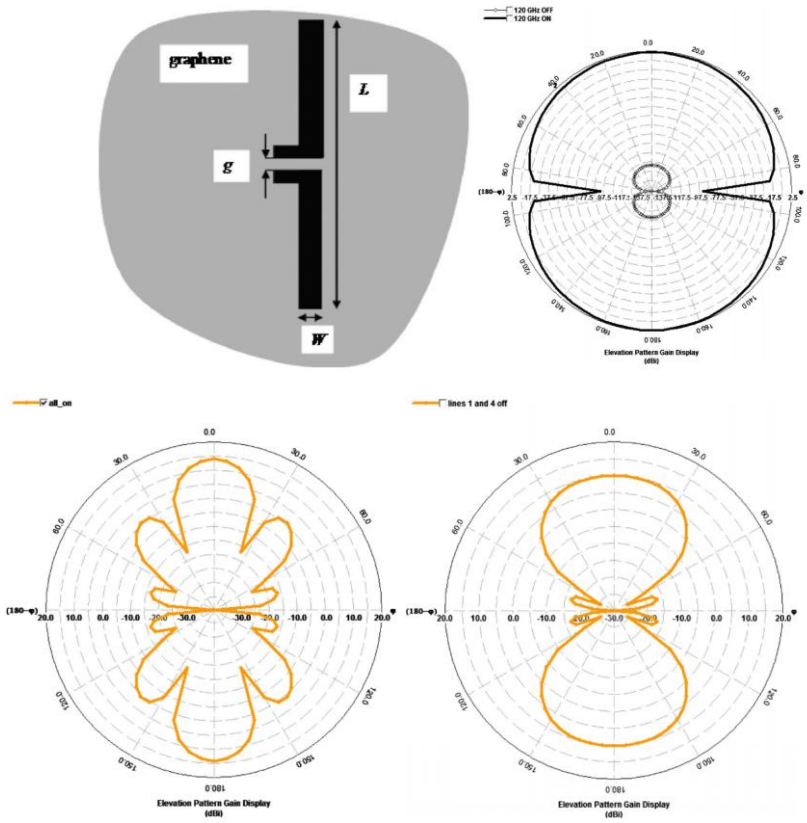


Figure 18 - Proposed dipole (top left) and its on and off radiation pattern (top right) for 120 GHz, and the THz antenna array's radiation pattern with all antennas turned on (bottom left), and with two lines turned off (bottom right) [36].

In further studies such as [43] and [44], a graphene antenna was proposed and simulated, considering a range of frequencies from 8 to 18 GHz, and then the antenna was fabricated and measured. The authors noted that antennas with high efficiency are not achievable at the micro to mm-wave range with graphene given its high impedance. However, it can be modified to obtain decent values, or else they can be used where low efficiencies are acceptable. Through the measurement of the fabricated antennas, it was possible to tune the reflection parameters through a DC voltage, shifting them up or down. Afterward, the antenna's directivity was measured from 8 to 12 GHz. The authors noted that

the radiation efficiency of these antennas is lower when compared to its metallic counterparts, however, they also claim that graphene antennas can be more advantageous due to the material's wideband properties, since its counterpart metallic antennas are mostly narrowband.

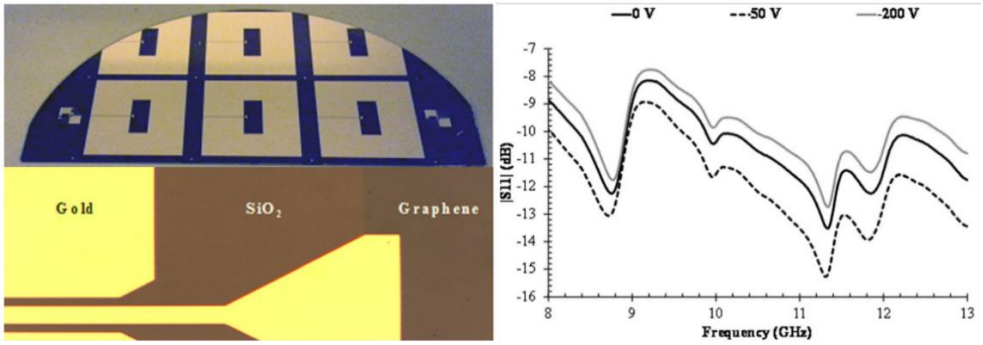


Figure 19 - Fabricated graphene antennas on the left side, and S11 with different DC bias on the right side [44].

In [45] graphene was used with the aim of developing a transparent antenna. The authors have used various monolayers of graphene as well as doping to reduce graphene resistance. This resulted in a three-layer stack that could be transferred onto a quartz substrate.

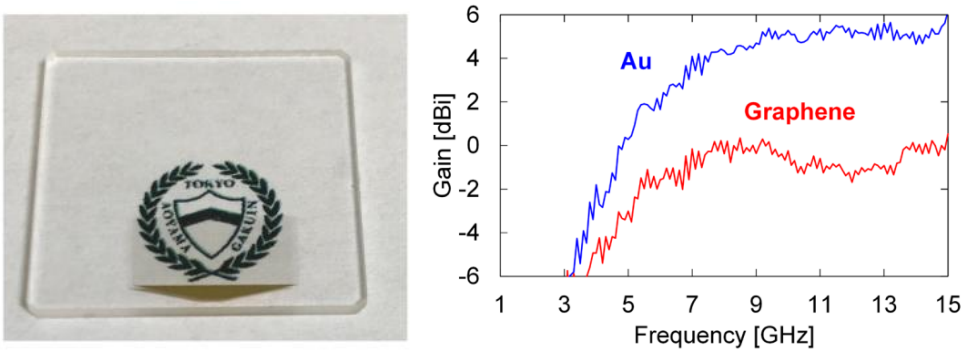


Figure 20 - Fabricated graphene antenna on the left and measured gain on the right [45].

It is possible to observe that the authors reported that the graphene antenna achieved a gain of 0.3 dBi at 8.5 GHz and -0.4 dBi at 9.8 GHz, while the Au antenna achieved 5.5 dBi at 11.5 GHz and 2.8 dBi at 6.3 GHz. The authors suggest that most of the difference is due to the difference in radiation efficiency. Furthermore, the Au antenna is significantly thicker and not transparent.

2.4 Device modeling

Designing graphene devices, fabricating them, and obtaining a device with the desired characteristics depends on the available models. Therefore, in this sub-section, an analysis of current developments on the modelling of graphene devices (inductors, capacitors, and antennas) will be undertaken.

2.4.1 Modeling of graphene inductors

For the modeling of the graphene inductor, in [15], the series inductance and resistance are obtained through the impedance modelling procedure developed in [46] and in [47]. In the previously mentioned works, the high-frequency behavior of graphene is reported and modeled, and according to the authors, an accurate model is proposed. According to the authors, this model not only allows for high-frequency, but also for low frequency and DC impedance extraction. Furthermore, according to the authors, this methodology can be applied in the analysis of high-frequency effects in multi-layer graphene ribbons. This can be used to investigate important implications in very large-scale integration interconnects and in inductor design.

In [26], the authors claim that currently available simulation tools are not able to use the intrinsic physical mechanisms of carbon nanomaterials, and then use them to model the impedance/inductance. Because of the unique properties of graphene, its impedance behaves differently when compared to conventional metals. In order to achieve some sort of prediction, the authors proceeded to analyze the performance of the inductors through FEM simulations in ANSYS HFSS. After that, the inductors were modelled as coils with electrical conductivities that incorporate grain-boundary and surface-scattering effects at micro and nano-scale for metals, and graphene conductivities that were extracted from DC measurements [26].

The properties of graphene were studied and modelled in [28], and in the same publication the structure was simulated with HFSS. However, the authors do not report on how graphene's simulations were performed. Still, the authors use the Launder's approach to calculate the kinetic inductance per unit length, which is given by:

$$L_k = \frac{2\pi^2\hbar}{e^2 v_F M} \approx \frac{81\ nH}{M}/\mu m \tag{1}$$

where M is the number of quantum modes ($M = \frac{\Delta E_F}{\pi\hbar v_F} W$), ΔE_F is the difference of Dirac point energies and Fermi level, and W is the width of graphene), e is the electron charge, $\hbar$ is the Planck's constant, and v_F is the Fermi velocity.

In [48], the modelling of the graphene inductors of [26] are reported. This model uses the multilayer graphene inductors as a reference and thus starts by determining the number of conducting layers through the thickness and spacing of graphene. In this case, the spacing of graphene is between each layer and depends on the type of doping that is used in the fabrication process. Finally, the authors the authors claim that the kinetic inductance can be calculated and added in series. The authors claim that the conductivity of graphene doesn't change with the width, thus apparently using this as a bulk

constant for the resistance modelling which appears to be used directly in the simulator. This modelling method was developed for the simulation of multilayer graphene inductors.

2.4.2 Modeling of graphene capacitors

An interdigital graphene quantum capacitor was proposed in [31], and in [49] further details are reported. In the presented model, the capacitance between the metal fingers was not included since it is in the order of femtofarads and was considered negligible. The simulations were carried out with HFSS, and it was determined that these values were lower than 0.08 pF, without taking the effect of graphene into account. With graphene, the maximum measured capacitance was higher than 1 pF. It is reported that inter-finger capacitance is also an overestimation of the value, since the introduction of graphene causes the distribution of the electric field to be mostly between the graphene and metal finger. The expression for the quantum capacitance is reported as [31]:

$$C_q = \frac{2e^2 k_B T}{\pi(\hbar v_F)^2} \ln\left[2\left(1+\cosh\frac{eV_{ch}}{k_B T}\right)\right] LWN \tag{2}$$

where e is the electron charge, $\hbar$ is the reduced Planck's constant, and v_F is the Fermi velocity, k_B is the Boltzmann's constant, N is the number of gate fingers, and L and W are the length and width of the finger.

In [32], the authors propose that their tunable quantum capacitor is equivalent to two capacitors in series, one capacitance corresponds to the geometric capacitance of the parallel plates, and the other is the quantum capacitance of graphene. This quantum capacitance is then defined as $C_q = dQ/dV_{ch}$. The tunable quantum capacitance effect is more pronounced near the Dirac point of graphene when the quantum capacitance becomes comparable or smaller than the geometric capacitance [32].

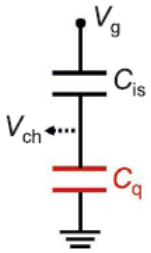


Figure 21 - Equivalent model of a graphene quantum capacitor.

MLG graphene with hBN is used to theoretically predict and propose a tunable THz resonator in [38]. It is a configuration that could be attractive for a capacitor, however, it presents a very high fabrication complexity, and it may not even be possible to be fabricated with current fabrication techniques. In this case, numerical predictions are also used. It is reported that the density functional theory

calculations predict that intercalating graphene with hBN changes the energy dispersion of MLG, approximating each graphene layer by a single conductor, where the conductivity of graphene is given by:

$$\sigma_{AC} = \frac{\sigma_{DC}}{1 + j\omega\tau} = \frac{2e^2 k_B T\tau}{\pi\hbar^2(1 + j\omega\tau)} \ln\left[2\cosh\frac{E_F}{2k_B T}\right] \quad (3)$$

where σ_{DC} is the DC conductivity of graphene, e is the electron charge, k_B is the Boltzmann's constant, τ is the momentum relaxation time, and T is the temperature. If the anomalous skin effect occurs at high frequencies, the Boltzmann equation cannot be simplified to the Ohm's law and therefore a critical ratio is used:

$$CR = \lambda_{mfp}/\sqrt{2/\omega\mu_0\sigma}.\,[1 + (\omega\tau)^2]^{-(3/4)} \quad (4)$$

where λ_{mfp} is the mean free path, ω is the angular frequency ($2\pi f$), μ_0 is the free-space permeability, and σ is the in-plane conductivity, which is the DC conductivity, divided by the spacing between two layers. To determine the resistance and skin effect, the authors have resorted to:

$$R_S = \sqrt{\frac{\omega\mu_0}{2\sigma}}.\sqrt{\left[\sqrt{1 + (\omega\tau)^2} - \omega\tau\right]} \quad (5)$$

$$\delta = \sqrt{\frac{2}{\omega\mu_0\sigma}}.\sqrt{[1 + (\omega\tau)^2].\left[\sqrt{1 + (\omega\tau)^2} - \omega\tau\right]} \quad (6)$$

It was concluded that the surface resistance of intercalated MLG and hBN is much smaller than only MLG, making it more suitable for passive applications. In addition to this, the skin depth of intercalated MLG and hBN is smaller than MLG due to its higher conductivity, thus making it a better candidate to outperform MLG for passive elements. The authors have also delved into the modeling of hBN and intercalated MLG, where the per unit length of its series impedance, scattering resistance and kinetic inductance is given by:

$$Z_{SLG} = R_S + j\omega L_k = \frac{1}{\sigma_{DC} W_{GR}} + j\omega\frac{\tau}{\sigma_{DC} W_{GR}} \quad (7)$$

The quantum capacitance is calculated in a similar way in equation (2), but in this case, the authors have not taken into consideration the dimensions of the metallic contacts.

2.4.3 Modeling of graphene antennas

A patch antenna for terahertz is proposed by the authors in [33]. Its surface conductivity is dependent on properties such as its chemical potential, frequency, and scattering rate. According to the authors, graphene can be characterized as a two-sided surface characterized by a complex conductivity ($\sigma(\omega, \mu_c, \Gamma, T)$) that is described by the Kubo formalism. It can be described through inter-band and

intra-band contributions, where the intra-band contributions dominate in f < 5 THz. The total conductivity is thus given by:

$$\sigma(\omega, \mu_c, \Gamma, T) = \sigma_{s,intra} + \sigma_{s,inter} \tag{8}$$

$$\sigma_{s,intra} = \frac{je^2(\omega - j2\Gamma)}{\pi\hbar^2}\left[\frac{1}{(\omega - j2\Gamma)^2}\int_0^\infty \varepsilon\left(\frac{\partial f_d(\varepsilon)}{\partial\varepsilon} - \frac{\partial f_d(-\varepsilon)}{\partial\varepsilon}\right)d\varepsilon\right] \tag{9}$$

$$\sigma_{s,inter} = \frac{je^2(\omega - j2\Gamma)}{\pi\hbar^2}\left[-\int_0^\infty \frac{f_d(-\varepsilon) - f_d(\varepsilon)}{(\omega - j2\Gamma)^2 - 4\left(\frac{\varepsilon}{\hbar}\right)^2}d\varepsilon\right] \tag{10}$$

where ω is the angular frequency, e is the electron charge, μ_c is the chemical potential, $\hbar$ is the reduced Planck's constant, T is the temperature, $\Gamma = 1/2\tau$ is the electron scattering rate, τ is the electron relaxation time, and $f_d(\varepsilon)$ is the electron's energy-dependent Fermi-Dirac distribution, which is expressed as:

$$f_d(\varepsilon) = \left(e^{(\varepsilon - \mu_c)/k_B T} + 1\right)^{-1} \tag{11}$$

The chemical potential of graphene and consequently its conductivity can be controlled through the application of an electrostatic bias and chemical doping. The authors have explored this property and used DC biasing to model and control their antenna, and finally they used CST to simulate the antenna. Similarly, in [39] a graphene dipole is proposed in which different substrates are used. The simulations were also carried out with CST, however, the authors do not delve into the modeling of the graphene behavior.

In [34], the authors propose another antenna for terahertz, however, it is simulated in HFSS. The authors simulate the antennas in HFSS, but they also reference another FDTD solver developed by themselves, where the models are further explored. The study presented in [40] is undertaken with five different structures for terahertz antennas. In this case, the five different structures were simulated using CST, and with graphene which had a thickness of 0.34 nm. The authors have also modeled the conductivity of graphene through the Kubo formula, where only the intra-band transition is considered:

$$\sigma(\omega, \mu_c, \Gamma, T) = \frac{2e^2}{\pi\hbar}\frac{k_B T}{\hbar}\ln\left[2\cosh\left[\frac{\mu_c}{2k_B T}\right]\right]\frac{-j}{\omega - j\tau^{-1}} \tag{12}$$

The chemical potential was considered 0.3 eV throughout the paper. In order to develop a reliable library for the simulation, a combination of the Drude model and the surface conductivity was employed to determine the plasma frequency:

$$\omega_p = \sqrt{\frac{2e^2}{\varepsilon_0 \Delta\pi\hbar}\frac{k_B T}{\hbar}\ln\left[2\cosh\left[\frac{\mu_c}{2k_B T}\right]\right]} \tag{13}$$

A beam scanning THz antenna in graphene that is electronically steerable is proposed in [35]. In order to model the graphene's conductivity, the authors have resorted to another form of the Kubo formalism, where the inter-band contributions are once again neglected. A DC bias was also applied, where the gate oxide was considered relatively thick, thus neglecting the quantum capacitance. The radiation patterns were obtained through HFSS simulations and leaky-wave antenna theory.

In [36], the IE3D simulation software was used to simulate a GHz and a THz antenna. In this case, the graphene properties used were constants. Two values were used for the resistivity: 0.15 Ωcm at a gate voltage of 0 V, 10^{-5} Ωcm at a gate voltage of 15 V, and have considered a permittivity ε_e of 5.

2.5 Discussion

In the previous section, the state of the art in the applications of graphene in RF passive elements was explored. Graphene has been shown to be a strong candidate for RF applications, with a high cut-off frequency of up to 300 GHz, applications on interconnects and passives, as well as being used in various applications [1], [15].

The application of graphene on inductors envisages the increase of the inductance density values, thus reducing the total area of integrated circuits [1], [15], [26], [27], [28]. Graphene can contribute on account of its high conductivity, as well as its large kinetic inductance, which contributes by increasing its series inductance and is influenced by the material's properties and not by the inductor design. It has been demonstrated that comparing to metal inductors, not only the inductance density but also the Q factor could be increased [26].

The reported graphene inductors in the literature claim that a 1.5 times higher inductance can be obtained in a two-turn inductor when compared with its metallic counterpart [26]. Although graphene is a promising material for inductors, it is still necessary to lower its resistance (although its conductivity is very high, its low thickness makes it have a high resistance, when compared to bulk metals) [26], [27]. In order to achieve this, doping has been proposed, for which bromine was used [26], and other compounds are being suggested, such as Li, Na, K, Cl_2, Br_2, ICl, BF_3, AsF_5, $AuCl_3$, and $FeCl_3$. Additionally, the contact resistance can also be improved since it is an important factor that negatively impacts the inductors' Q-factor [15], [26], [27]. Finally, in [15] the authors conclude that through substrate engineering (using low-loss substrates, SiO_2, and increasing its thickness, for example) it is possible to increase the Q-factor of the inductors, which can be done through using a low-loss substrate, as well as by increasing its thickness. On the other hand, there is very little research on the behavior of single-layer

graphene for inductors. Graphene shows a high resistance when long structures are required due to its extremely small thickness as is the case of the geometry of inductors. These usually require long traces, however, with the increase in frequency, it is apparent that it could be possible to outperform metallic inductors more easily. On the basis of this reasoning is the fact that the impedance of inductors increases with frequency, thus at higher frequencies lower inductances should be required. This leads to a smaller inductor, which could have dimensions similar to a metallic one, hence outperforming the latter – since graphene outperforms metals when similar, small dimensions are used [26], [28]. A summary of inductor characteristics is presented in Table 1, where graphene inductors are presented, as well as metal inductors for comparison.

Table 1 - Planar inductor characteristics of graphene and metal inductors.

Ref	Inductor type	Inductance (nH)	Frequency (GHz)	Q factor	Area (μm^2)	Density ($pH/\mu m^2$)	Material
[26]	Narrow square	1.2	5 – 40	11 @30 GHz	40000	0.03	Bromine doped MLG
[26]	Octagonal	1	10-40	10 @35 GHz	40000	0.03	Bromine doped MLG
[26]	Wide square	1.2	5-35	8 @25 GHz	40000	0.03	Bromine doped MLG
[15]	¾-turn	0.15	40.8	3	400	0.38	MLG, highly ordered pyrolytic graphite
[15]	2-turn	0.41	57	2.97	1225	0.33	MLG, highly ordered pyrolytic graphite
[15]	3-turn	0.33	57	3.52	1600	0.20	MLG, highly ordered pyrolytic graphite
[27]	¾-turn	0.34	67	2.36	2400	0.14	Graphite
[50]	4.5	6.29	4.6	13.3	35156	0.18	Metal
[51]	4	2.4	5	30	125663	0.02	Metal
[52]	4.5	35	1.5	17	810000	0.04	Metal
[37]	5-turn coil	520	0.04	30.3	28274000	0.018	Doped MLG and metal

The application of graphene capacitors relies mostly on their application in biosensors, where a graphene varactor is used to determine the concentration of the target molecule [29]. On the other hand, the development of such varactors can be useful for wireless biosensing. Graphene varactors have been proposed for RF and have shown that they can be a promising solution. When compared to RF MEMS, a capacitance that is 100 times larger has been reported, in addition to its low tuning voltage and simplified

fabrication process [30], with the potential of outperforming MOSCAPs at high frequencies [31]. Other authors [32] have presented a capacitor that achieved a tuning ratio of 1.53:1 with a voltage of 2 V, and claim that it can be over 8.3:1. These predictions also reinforce that graphene capacitors can outperform MEMS capacitors in tuning ratio and with a lower control voltage, although intricate, it is possible to fabricate CMOS compatible devices. A summary of capacitor characteristics is presented in Table 2, where graphene capacitors are presented, as well as metallic RF MEMS capacitors for comparison.

Table 2 - Capacitor characteristics of graphene and RF MEMS capacitors.

Ref	Type of capacitor	Capacitance (pF)	Frequency (GHz)	Q factor	Area (μm^2)	Density ($fF/\mu m^2$)	Tuning ratio	Tuning method	Tuning voltage (V)	Material
[29]	Interdigitated capacitor	120	0.001	-	30938	3.88	1.12:1	Glucose	-1 to 1	Graphene
[30]	Interdigitated capacitor	2.3	0.4	14.5	-	-	1.3:1	Voltage gating	-1.5 to 1.5	Graphene
[31]	Interdigitated capacitor	0.943	0.35	13.6	414	2.28	1.3:1	Voltage gating	-1.5 to 1.5	Graphene
[31]	Interdigitated capacitor	0.337	0.8	12	198	1.70	1.17:1	Voltage gating	-1.5 to 1.5	Graphene
[31]	Interdigitated capacitor	2.733	0.2	11.6	918	2.98	1.34:1	Voltage gating	-1.5 to 1.5	Graphene
[32]	Parallel plate	3.5	0.00145	-	1214	2.88	1.53:1	Voltage gating	0 to 2	Graphene
[53]	RF MEMS	1.57	0.8	118.5	591486	0.0027	1.01:1	Voltage gating	0 to 100	Metal
[54]	RF MEMS	0.25	1	39	1836000	0.00014	2.25:1	Voltage gating	0 to 100	Metal
[55]	RF MEMS	0.05	8	-	-		10:1	Voltage gating	0 to 30	Metal

The modeling of graphene inductors has not been established yet, with current modeling and simulation tools not prepared yet to predict the behavior of graphene structures [26]. The current best approach relies on the simulation of normal metallic structures to analyze their performance, and then try to include some parameters that can more closely replicate graphene's characteristics [26].

Current graphene capacitor modeling is not well established, with HFSS simulations being performed to predict the behavior of the metallic parts, without taking graphene into account [31]. Another approach, used in [38], relies on the theoretical prediction of graphene's conductivity, approaching it by a single conductor. In [32], the authors have included the quantum capacitance effect through the control voltage in their prediction, managing to fit their curve to the experiments. Although graphene capacitor modelling is not well established, there are currently various alternatives demonstrated in the literature. However, there is a lack of integration of such models, so that circuit design can be easier.

Regarding graphene RF antennas with monolayer graphene, the presented works are mostly focused in modeling and theoretical predictions, which are achieved through the Kubo formalism. Although graphene has high resistivity, this formalism states that the conductivity of graphene depends on its chemical potential. The previously presented works use current simulation software such as CST and HFSS and explore the tuning of graphene through DC biasing.

In conclusion, some limitations of graphene have already been defined, such as its resistance (for structures that require long traces, due to its extremely small thickness) and contact resistance [56], [57], [58]. On the other hand, its controllable conductivity is used to implement tunable components, which may perform better than current alternatives. Furthermore, current works don't establish a method to fabricate and to predict the behavior of the fabricated structures. Although Kubo's formalism is extensively used for antennas, the modeling of inductors and capacitors has not yet been established. Although some modelling attempts have been made, they may not reflect the characteristics of all fabricated graphene. Since the properties of graphene may vary according to its fabrication procedure and device integration procedure, it is currently necessary to characterize and extract the parameters of the graphene being used.

3 EXTRACTION OF GRAPHENE RF PARAMETERS

To perform RF characterization of any device, the first mandatory step consists of the vector network analyzer (VNA) calibration, to shift the measurement plane to the device under test (DUT). That can be achieved through other alternatives such as short-open-load-through (SOLT), line-reflect-match (LRM), and TRL [59]. The TRL calibration algorithm, when coupled with precision transmission lines, provides one of the highest calibration accuracies [60], [61]. It relies on the characteristic impedance of the designed transmission lines, on two transmission lines with different lengths, and one-port reflect termination [62]. Furthermore, for the measurement of graphene devices, it was demonstrated in [59] that not only is TRL the best candidate for such measurements, but the authors also claim that using SOLT could lead to erroneous values of graphene properties. Since the commercial SOLT solutions do not remove the contributions of the transmission lines even though the resistance of the 2D material can be extracted with small error (since the 2D material's resistance is much larger than the transmission line's resistance), the small inductance and capacitance values may have a similar order of magnitude, from which these errors may arise.

In this section, the issues of implementing the TRL calibration applied to the characterization of 2D materials, such as graphene, are presented. The impact on the RF parameter extraction due to the design of the calibration structures, such as contact thickness, substrate loss, contacting graphene, and backgate design, are analyzed through simulations.

3.1 TRL calibration implementation

The implementation of the TRL calibration focuses on the design of the calibration structures, their frequency span, and the characteristics of the substrate. In this case, coplanar waveguides were used so that it is possible to contact them with ground signal ground RF probes and fabricate the device in small dimensions so that it can be used with graphene. Then, the determination of the characteristic impedance is discussed since the calibration is related to the impedance of the transmission lines. For the extraction of graphene's characteristics, the pi model will be discussed.

3.2 Design of calibration structures

To explore this calibration, it was necessary to define the calibration structures as well as the device under test. The number of lines used depends on the frequency span for which the calibration is used. The optimal line length is ¼ wavelength, and each thru/line pair has a usable bandwidth of 8:1 (frequency span/start frequency) [60], [63]. Since 3-line standards cover a bandwidth of 512:1, for this calibration spanning from 1 to 65 GHz, 3-line standards are required. To determine the length of the lines, a geometric segmentation of the bands can be used. For the three-line standards, the crossovers FT1 and FT2 are:

$$f_{T1} = f_L * 10^{\log\left(\frac{f_H}{f_L}\right)*(1/3)} \tag{14}$$

$$f_{T2} = f_L * 10^{\log\left(\frac{f_H}{f_L}\right)*(2/3)} \tag{15}$$

where f_{Tn} is the crossover frequency, f_L is the lower frequency, and f_H is the higher frequency. Then, the center frequency is determined through the arithmetic average of the crossover points. To determine the length of each line, since the optimum is one-fourth of the wavelength, the dielectric constant is used:

$$l = \frac{\mathrm{c}}{f_C\sqrt{\varepsilon_r}} * \frac{1}{4} \tag{16}$$

where c is the speed of light, f_C is the center frequency of the line standard, and ε_r is the effective relative permittivity.

To develop the calibration structures, we considered that the measurement probe would have a ground signal ground configuration with a pitch of 100 µm, and the calibration frequency would be from 1 GHz to 65 GHz to validate the calibration from low GHz up to mm-wave. The substrate was silicon, 700 µm thick, with a 100 nm silicon oxide layer, a typical oxide thickness that allowed us to fabricate a buried gate. The silicon had a dielectric constant of 11.9 and a resistivity of 10×10^3 Ω.cm, and the silicon oxide had a dielectric constant of 3.9 and loss tangent of 0.01. The metal used was copper, with a conductivity of 5.8×10^7 S/m. The dimensions (Figure 22) of the coplanar waveguide (CPW) were calculated so that a 50 Ω impedance line was obtained: 50 µm signal width, spacing of 30 µm, and ground width of 90 µm. The length of the Thru was 350 µm to allow for an easier measurement probe placement and prevent crosstalk, equaling a 175 µm line for the measurement of the remaining structures. The calibration frequency was from 1 GHz to 65 GHz; however, to avoid resonance at higher frequencies in the longer lines and determine the line lengths, we considered that the frequency range was from 1 GHz to 70 GHz to shorten the lines and shift possible resonant frequencies outside the calibration range. Since the predicted effective permittivity of the substrate is 6.36, the length of the lines

was 11,614 µm, 2818 µm, and 683 µm. These calibration structures are presented in Figure 22 and are labeled Thru, Reflect, and Line. It was considered that the DUT occupied an area of 100 µm × 50 µm, allowing for a large area to build a device. In this case, it also allows us to characterize and extract the sheet parameters of graphene.

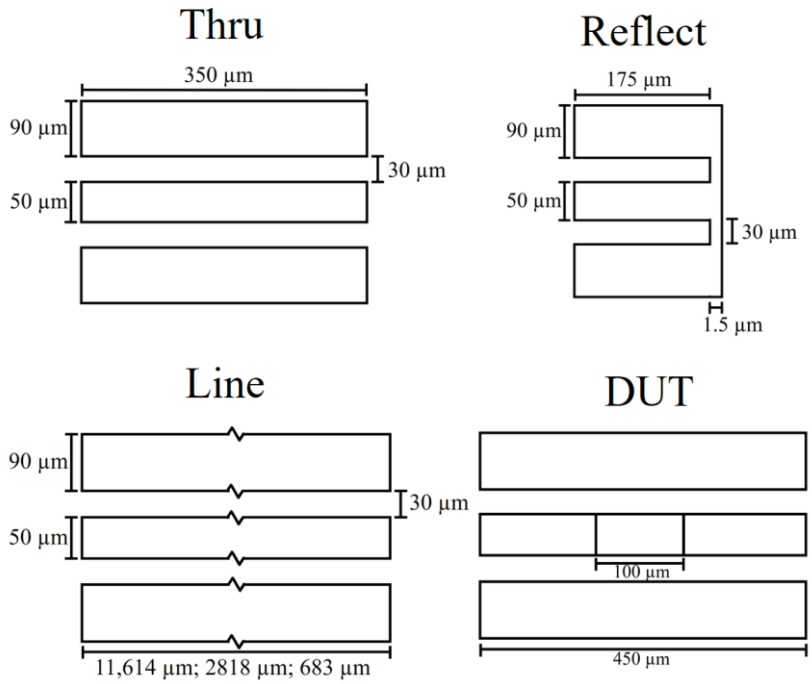


Figure 22 - Calibration structures and dimensions used in the implementation of the TRL calibration algorithm.

These calibration structures are tested to assess their viability for device parameter extraction, as well as their application on the measurement of graphene. Furthermore, some parameters, such as substrate conductivity, metal thickness, and inclusion of graphene-specific features, are studied through simulations.

3.3 CPW characteristic impedance measurement

The result from the TRL calibration involves the characteristic impedance of the transmission lines. Therefore, the S-parameters reference characteristic impedance and in most cases, should be converted to the typical 50 Ω reference impedance. To determine the characteristic impedance of the transmission line, the procedure proposed in [64] was undertaken. A previous calibration of the measurement setup, for example SOLT, must be performed to shift the reference plane to the beginning of the transmission lines. Afterwards, the TRL calibration can be performed, which allows us to extract the fabricated

transmission lines' characteristic impedance. When performing this calibration, the TRL calibration error terms represent the S-parameters of the transmission lines.

Three values obtained from the scikit-RF package [65] are used to build the S-parameter matrix and extract the characteristic impedance: forward reflection tracking (*FRT*), forward directivity (*FD*), and forward source match (*FSM*). It is now possible to obtain the S-parameter matrix [64]:

$$S_{CPW} = \begin{bmatrix} FD & \sqrt{FRT} \\ \sqrt{FRT} & FSM \end{bmatrix} \tag{17}$$

It is now possible to extract the characteristic impedance of the lines by transforming the S-parameters to T-parameters and through Equations (18) and (19) [64]:

$$G = \sqrt{\frac{T12 + T21^2}{4 + T12 + T21^2}} \tag{18}$$

$$Z = 50\frac{1+G}{1-G} \tag{19}$$

This method, however, is only accurate at lower frequencies. To obtain a more accurate approximation, the propagation constant that is given by the TRL calibration can be used by solving the capacitance and substrate conductance per unit length:

$$C = \text{real}\left(-\frac{j\gamma}{2\pi f Z}\right) \tag{20}$$

$$G = \text{real}\left(\frac{\gamma}{Z}\right) \tag{21}$$

The capacitance and conductance values are obtained from the lower frequency results of Equations (20) and (21), respectively, given that the method is more accurate in this range [64]. Since the propagation constant is given by the TRL calibration, it is now possible to determine the characteristic impedance through Equation (19). Since this impedance has been determined, it is now possible to calibrate and renormalize the TRL calibration results to 50 Ω by using the characteristic impedance values in the calibration procedure.

3.4 Two-dimensional materials TRL calibration methodology performance assessment

The validity of the proposed calibration method will be assessed in this section through simulations. Then, it is used to demonstrate different factors that can negatively impact, or even prevent, accurate measurements from being obtained. These are the metal thickness of the calibration structures and the substrate loss. Then, a calibration with thick copper contacts and high resistivity substrate is

demonstrated, as well as including thin gold contacts and a buried gate for the characterization of graphene. Since the inclusion of the gold contacts and the buried gate are a modification of the original TRL calibration, their influence on the characteristic extraction is reported.

The procedure of such calibration starts with a typical calibration (such as SOLT) of the measurement system to shift the measurement planes to the transmission lines of the TRL calibration. Then, the TRL calibration structures are measured, and their characteristic impedance is extracted through the steps described in the previous section. In this case, the simulation software is used to simulate only the calibration structures, mimicking the initial step (SOLT and structure measurement for characteristic impedance extraction). After obtaining the characteristic impedance of the transmission line, the calibration can be carried out without any pre-calibration of the VNA, and the desired RF characteristics can be extracted. This corresponds to including two 2 m long, 53 Ω coaxial cables in the simulation, one for each measurement port. This demonstrates that the calibration can be performed even with slightly mismatched coaxial cables.

Implementing this calibration with 2D materials can be a challenging task due to their physical dimensions and the 2D materials' characteristics such as tunability. Another constraint related to characterizing two-dimensional materials is their inherent high series resistance. Graphene has a sheet resistance of 0.5 kΩ to 1.5 kΩ [66]. Since the resistance of the device being measured is comparable, or higher, than the impedance between the measurement contacts (capacitance between both contacts), it is necessary to remove it. A similar structure, without the DUT, can be used to determine this capacitance, subtract it from the device's measurements, and correct the obtained values. In this section, this correction was used to show the results, and the constraints of measuring graphene are further explored and reported. The test structure used in the simulations is a lumped element of a 1 kΩ series resistance with 1 nH series inductance, which represents the resistance of a graphene sheet of 1 to 3 squares in length, which accounts for a device with inductive behavior.

3.4.1 Metal thickness effect on calibration accuracy

As described in [67], when graphene is transferred onto a substrate that contains a large step (such as a measurement contact), if this step is large enough, it may lead to a rupture in the 2D material. Therefore, to obtain a proper contact and avoid damage to graphene, it becomes necessary to fabricate contacts with a small thickness. On the other hand, this causes the contacts to have a large series resistance, which can compromise the reliability of the TRL calibration due to its dependence on transmission line characteristics [60], [61].

An example of graphene contact would be using a 20 nm thick Au contact, given that it allows for a small thickness to prevent graphene from rupturing and allows for a good contact resistance. In this case, to extract the RF characteristics, the TRL calibration method is evaluated through simulations. To test the effect of such small thickness on the calibration accuracy, the calibration was performed with 20 nm of Au. Figure 23 shows the results of performing the calibration and extracting the inductance and resistance of the lumped element.

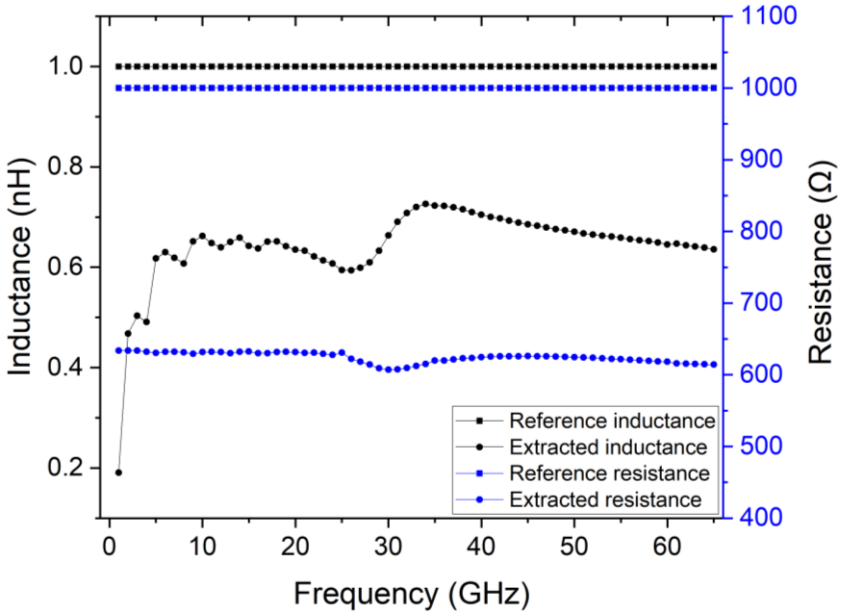


Figure 23 - Comparison of extracted inductance and resistance parameters of the lumped model when 20 nm thick gold contacts are used, and the expected reference values.

An accurate calibration would yield results close to 1 nH for the imaginary part and 1 kΩ for the real part. However, it is possible to observe that the inductance changes from approximately 0.2 nH to 0.7 nH, and the resistance is around 600 Ω. Therefore, it is possible to conclude that very thin contacts compromise the implementation of the TRL calibration and extraction of the device's properties.

3.4.2 Substrate loss effect on calibration accuracy

Since the characteristics of the transmission line can influence the accuracy of the calibration procedure, the substrate conductivity can be another inaccuracy source. To demonstrate the impact of the substrate conductivity, the properties of a standard clean room doped silicon wafer with 100 Ω.cm are used in the simulation. The measurement structures are as previously described, and the contacts are made of 5 µm thick copper to remove the previously described effect of the metallic resistance of the

calibration accuracy. Figure 24 shows the comparison between the reference values from the lumped element and the extracted values through the TRL calibration.

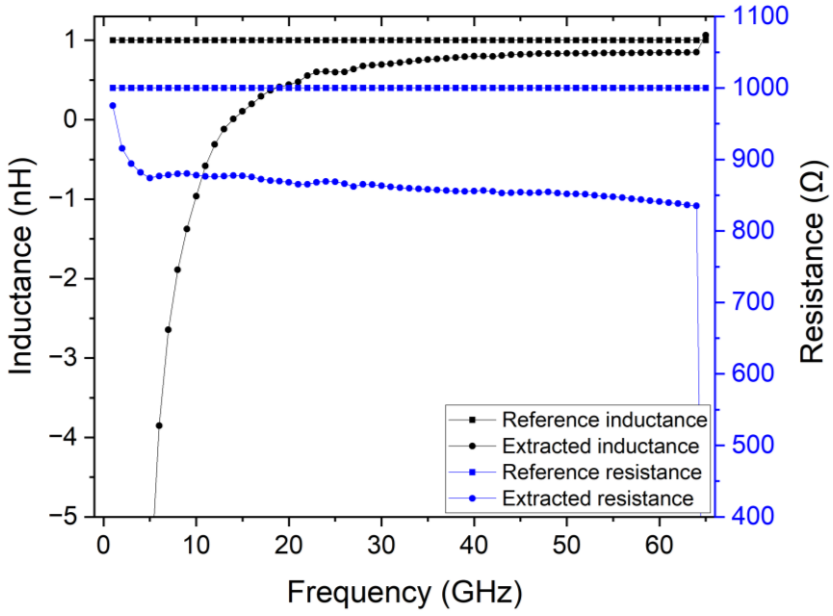


Figure 24 - Comparison of extracted inductance and resistance parameters of the lumped model when a substrate with 100 Ω.cm conductivity is used and the expected reference values.

It is possible to observe that the substrate loss impacts the extraction of the RF characteristics of the device. The series resistance is in the 800 Ω to 900 Ω range when it should be around 1 kΩ, and the inductance is in the −165 nH to 0.8 nH range when 1 nH is expected – the negative inductance arises since the formula for inductance was used to maintain coherent units and allow for an easier comparison with the remaining values, meaning that this shows a capacitive behavior. This is due to the increased transmission line losses that are induced by the substrate conductivity.

3.4.3 Effect of transition from metallic CPW to 2D CPW device interface

As demonstrated, the use of thin metallic contacts and lossy substrate causes the calibration to provide very unreliable results. This is due to the extremely high losses that are introduced in the transmission line. To overcome these issues, two approaches must be taken: reduce the contact resistance and reduce the substrate conductivity. To reduce the contact resistance, copper was used, which has one of the highest conductivities, and its thickness was increased to 5 µm to further improve the contact conductivity. For the case of substrate conductivity, a commonly available 10 kΩ.cm silicon substrate was used.

The problem of using 5 µm thick contacts is that these will break graphene (cf. Figure 25), and contact will not be made. Therefore, a 20 nm gold contact with a length of 35 µm is included to bridge the connection from the 2D material to the copper contact. Figure 25 depicts two scenarios where a gold contact is used, and a gold contact is not used. For the case where the gold contact is not used, Figure 25 A, it is expected that graphene breaks and does not make proper contact with the measurement contact, Figure 25 C. For the case where the 20 nm contact is included, Figure 25 B, graphene breaks with the height of the copper contact but still contacts the gold contact since its height is very small to break graphene. In this case, it may either lay flat, Figure 25 D, or roll back, Figure 25 E.

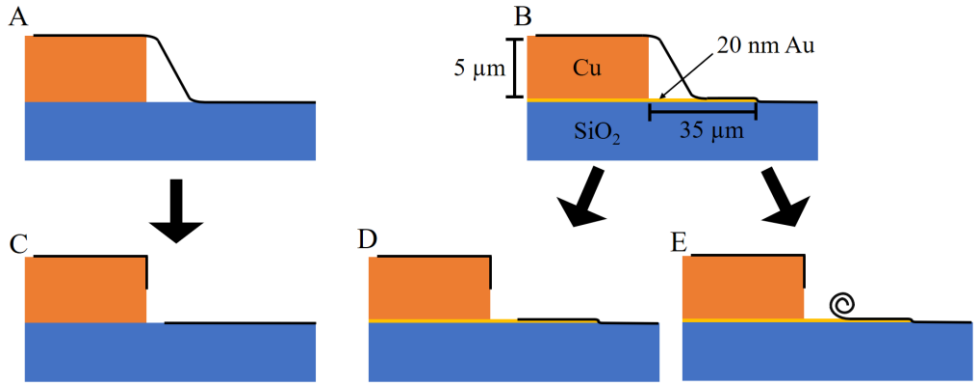


Figure 25 - Metallic contact between copper and the 2D material: (A) the case where the material is contacted directly to copper; (B) the case where the material is contacted with a 20 nm thick gold contact; (C) the consequence of undertaking scenario A and demonstrating the 2D material breaking and not making contact with copper; in (D) the consequence of scenario B, where the contact between the copper and 2D material is mediated through a 20 nm thick gold contact and the 2D material lays flat; (E) the consequence of scenario B, where the contact between the copper and 2D material is mediated through a 20 nm thick gold contact, and the material breaks and rolls back.

Figure 26 displays the results of the simulated calibration when performed with 5 µm thick contacts and 10 kΩ.cm silicon substrate conductivity and the results of the calibration when these structures include the 20 nm gold contact with a length of 35 µm.

It is possible to observe that the accuracy of the measurements has increased when compared with the scenario where the structures have thin contacts, and the scenario where the substrate has a high conductivity. The extracted inductance is now around 0.9 nH to 1.1 nH, and the resistance is between 900 Ω to 1 kΩ, when 1 nH and 1 kΩ were expected, respectively. For example, when comparing with the high conductivity substrate scenario, where the inductance was much lower than 0.6 nH for frequencies lower than 25 GHz and the resistance was between 800 Ω to 900 Ω, this demonstrates that using 5 µm thick copper contacts and 10 kΩ·cm silicon substrate provides a reliable calibration for measuring 2D materials. Furthermore, 20 nm gold contact with the length of 35 µm and with a

conductivity of 4.1×10^7 S/m was included. These structures were simulated, and the characteristics of the lumped model were extracted. Figure 5 shows the results of the calibration where the extracted inductance was around 0.9 nH to 1.1 nH and resistance was between 900 Ω to 1 kΩ when 1 nH and 1 kΩ were expected, respectively. It is possible to observe that the impact of including these contacts is negligible and allows us to obtain a working device.

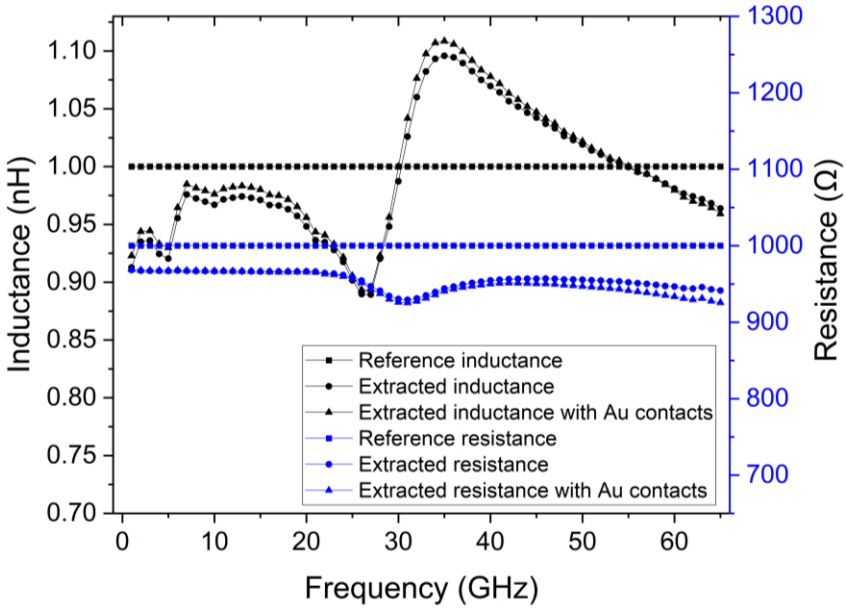


Figure 26 - Comparison of extracted inductance and resistance parameters of the lumped model when the contacts are made of 5 µm thick copper and the substrate has a conductivity of 10 kΩ·cm, and when 20 nm thick gold contacts are included, with the expected reference values.

3.4.4 Effect of back gate on the extracted graphene's characteristics

Most graphene applications rely on the control of its conductivity that depends on its chemical potential. Such property can be modified through a voltage gating and has been explored for tunable applications [68]. Therefore, it is a material that benefits from a characterization for different chemical potentials. This can be achieved through a buried gate that can be included in the described calibration structures. Figure 27 shows the calibration structure used to determine the DUT's characteristics, with a buried gate to control the graphene's chemical potential through tuning the gate voltage. This structure was simulated and was used to extract the lumped element's inductance, extracted inductance, and resistance. These values are shown in Figure 28 and have not changed significantly from the previous scenarios, obtaining an extracted inductance of 0.9 nH to 1.1 nH and a resistance from 900 Ω to 1 kΩ, when 1 nH and 1 kΩ were expected, respectively.

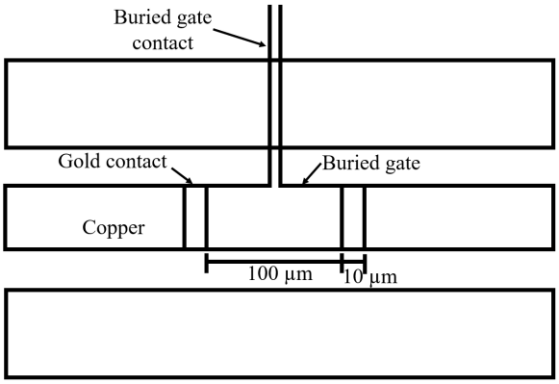


Figure 27 - Diagram of the DUT measurement structure with the buried gate, with a contact width of 3 µm, length of 437 µm, and a square contact pad with a side of 150 µm.

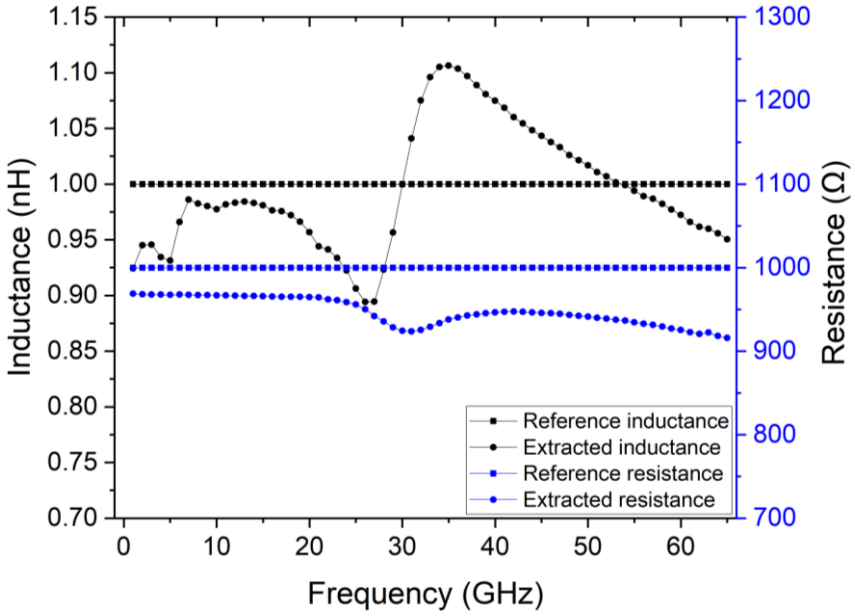


Figure 28 - Comparison of the lumped element's inductance and resistance and the extracted parameters of the lumped model when the contacts are made of 5 µm thick copper, the substrate has a conductivity of 10 kΩ.cm, 20 nm thick gold contacts are included, and a 10 nm thick back gate is introduced.

3.4.5 TRL validation for 2D material properties extraction

The previous simulations used a lumped element to mimic the extraction of the properties of graphene. That approach, however, does not account for the signal propagation in the device as well as its interaction with the backgate contact. Therefore, to mimic graphene, the lumped element was replaced by the best possible approach allowed by the simulator—a material with 1×10^5 S/m and a thickness of 20 nm, resulting in 500 Ω/square. The DUT area corresponds to two squares in series, which totals 1 kΩ series resistance. To determine the characteristics of the mimic device, the simulated TRL calibration

without the backgate was performed as well as with a backgate made of gold. Figure 29 shows the results of the extraction of the DUT's characteristics for both cases. It is possible to observe that including a gold backgate impacts the extraction of the device's characteristics, making it impossible to extract the correct values.

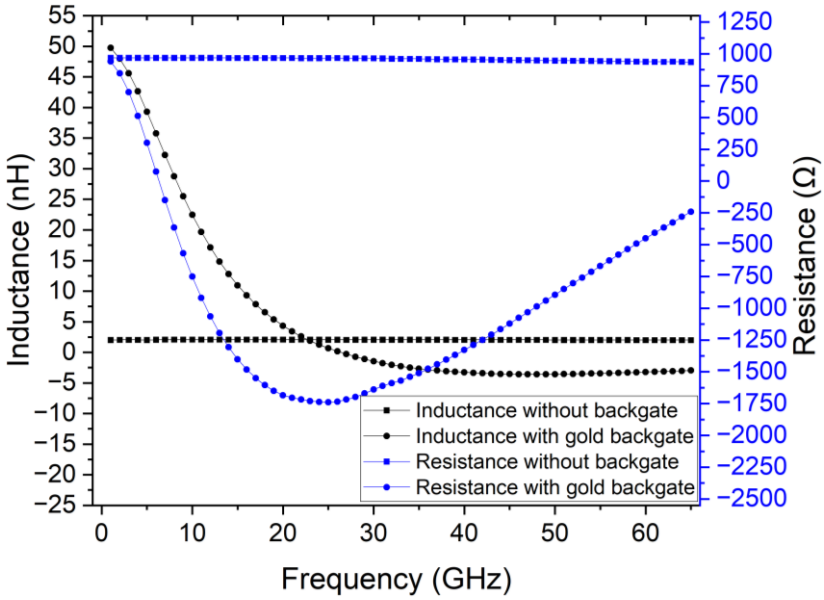


Figure 29 - Comparison of the simulated and extracted DUT's characteristics without the backgate and with a 10 nm thick gold backgate.

An alternative could be implementing a backgate design that has a high impedance, which would prevent the RF signal propagation from being influenced by the backgate. However, this design would need to be fit for a frequency range from 1 GHz to 65 GHz. Since the purpose of the backgate is transmitting a DC voltage to gate the 2D material, a simpler solution would be to increase its resistance. The only constraint is that the gate oxide must be much more resistive than the series resistance of the backgate itself, so that the applied voltage at the gate is close to the applied voltage at the gate contact. Therefore, the same backgate design can be used if the material's conductivity is modified. Since the highly conductive backgate contact impacts the parameter extraction, by reducing the backgate conductivity, it is possible to circumvent this problem. The extraction structures, with the same backgate design were simulated with a material with a conductivity of 2×10^4 S/m. Figure 30 shows the result of the simulation with the low conductivity backgate and the result without the backgate. It is possible to conclude that to obtain an accurate extraction method, a low conductivity backgate is necessary. Alternatively, to accommodate the structure to different materials, there is still room to change the backgate dimensions, such as using a thinner backgate contact or reducing the contact width.

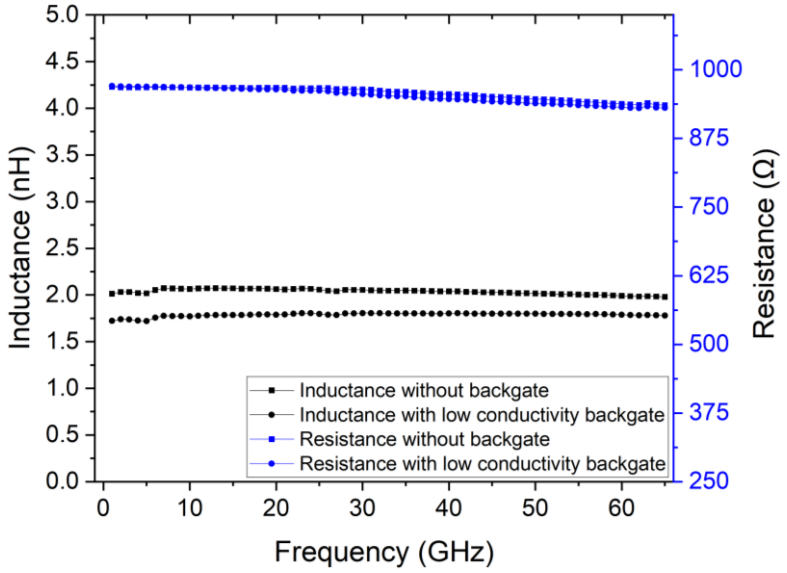


Figure 30 - Comparison of the simulated and extracted DUT's characteristics without the backgate and with a 10 nm thick backgate made of custom material with a conductivity of 2×10^4 S/m.

3.5 DUT parameter extraction methodology

The goal is to extract the series resistance, quantum capacitance, and kinetic inductance of graphene, since that information is necessary to develop interconnects, components, devices, and systems. Depending on the device geometry and number of graphene layers used, it is expected that the graphene device can have a capacitive or inductive behavior. To perform the TRL calibration, the NISTMultilineTRL procedure from the scikit-RF package [65] was used. After performing this calibration to extract the parameters, i.e., calculating the inductance (L) or capacitance (C) and resistance (R) of the DUT, the Y-parameters were used. To obtain the desired values, the real and imaginary parts of the $Y_{2,1}$ of the DUT were used:

$$L = -1 \times 10^9 \times \frac{\text{imag}\left(\frac{1}{Y_{2,1}}\right)}{2\pi f} \tag{22}$$

$$C = \frac{1 \times 10^{12}}{2\pi f * \text{imag}\left(\frac{1}{Y_{2,1}}\right)} \tag{23}$$

(24)

To perform a more detailed analysis on the extraction of graphene's characteristics, extracting and modelling can be performed with the support of the pi model.

3.5.1 Pi-model

Extracting the properties of the DUT directly through the equations (22), (23), and (24) allows to determine the DUT's characteristics. However, it is not possible to determine other properties such as contact capacitance. To further improve the extraction of such properties and model graphene's RF characteristics, a pi-model can be used, as shown in Figure 31. This is used as a simple and efficient way of representing equivalent circuit models and has also been proposed in [69], [70]. Then, to extract the components of the pi-model, the parameter extraction methodology proposed in [71] was used.

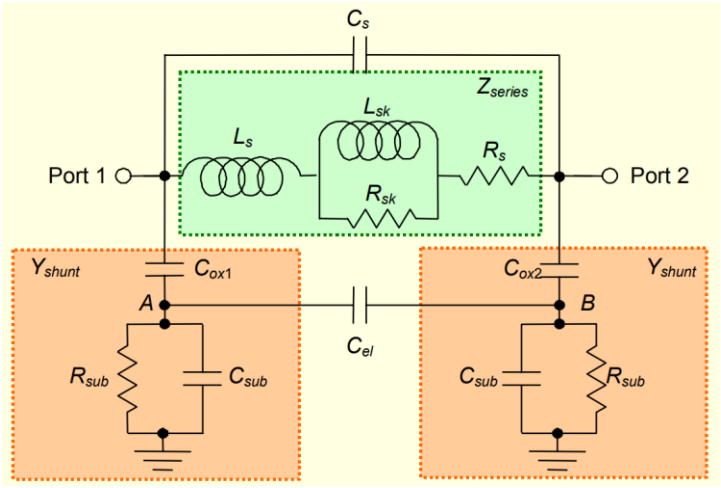


Figure 31 - Pi-model proposed in [71].

In this model, the R_{sub} and C_{sub} are the substrate resistance and capacitance, respectively. The C_{ox1} and C_{ox2} are the oxide capacitance, which together with the R_{sub} and C_{sub} form the Y_{shunt}, which is the shunt admittance. The authors have used the C_{el} to represent the lateral substrate capacitance and C_s the port-to-port series capacitance. The authors have used the R_s and L_s to represent the series resistance and inductance, respectively. In a similar manner, the R_{sk} and L_{sk} represent the resistance and inductance model the skin effect and proximity effects. These four elements, R_s, L_s, R_{sk}, and L_{sk}, form the Z_{series}, which is the series impedance.

As proposed by the authors, the Y_{shunt} and the Z_{series} can be extracted through [71]:

$$Y_{shunt} = Y_{11} + Y_{21} \tag{25}$$

$$Z_{series} = -\frac{1}{Y_{21}} \tag{26}$$

Through this method, it is possible to determine the R_{shunt} and C_{shunt}, which according to the authors are equal to R_{sub} and C_{sub} near DC. The C_{el} and the C_s are the lateral substrate coupling capacitance and the port-to-port series capacitance, respectively. These parameters are determined by fitting the model to

the measurement. Finally, the Z_{series} allows to determine the characteristics of the device, which are L_s, and R_{sk}, corresponding to the series inductance and resistance, to which L_{sk}, and R_{sk} were added, to represent skin and proximity effects.

To model the R_{sub}, C_{sub}, and C_{ox}, the equivalent R_{shunt} and C_{shunt} were calculated (represented as R_s and C_s in the schematic), corresponding to the model shown in [70]. To model the C_{el} and the C_s, structures without graphene were fabricated, and then, these values were extracted through the Y_{21}. The corresponding capacitance was represented as C_p in the schematic. Finally, to extract graphene's characteristics, model it, simplify the modelling process, and allow for an easier analysis and interpretation, a simple series RLC circuit was implemented. Although graphene conducts in DC and placing a capacitor in series is apparently counterintuitive, this is a high frequency model. Through performing several simulations analyzing the different configurations, it was determined that the modelling error for the frequencies used was lower when using series RLC. The updated pi-model is shown in Figure 32.

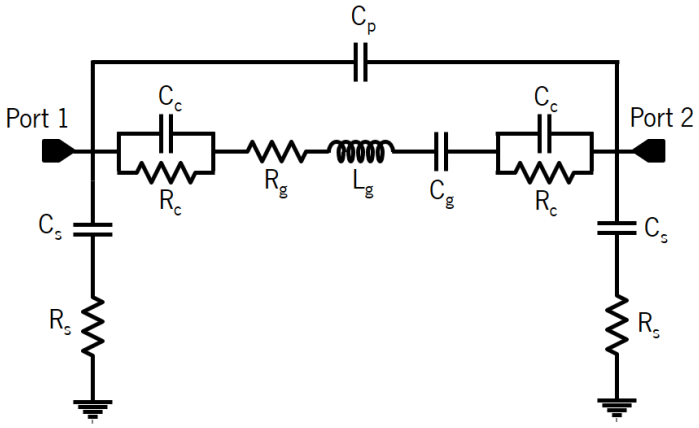


Figure 32 - Pi-model used to model the measured graphene devices.

It is possible to observe the previously described R_s and C_s, which correspond to the shunt resistance and capacitance, and C_p corresponds to the inter-port capacitance. These implemented RLC circuit correspond to graphene's characteristics, where the R_g corresponds to the series resistance, the L_g corresponds to graphene's kinetic inductance, and C_g corresponds to graphene's quantum capacitance. Finally, since graphene's contact with metal is not negligible, a contact resistance (R_c) and contact capacitance (C_c) was included.

The contact resistance and contact capacitance of graphene with metal are variable and can be modelled with a parallel RC, as analyzed in [72], as well as other works that have focused on modelling graphene [9], [73], [74]. Therefore, variable parallel R_c and C_c were included in the schematic. The

modelling of the graphene sheet in [9] is based on a high mobility 2D electron gas system. The authors have placed an R and L in series and a capacitance in parallel with that R and L, and the contact R and C. However, there is no explanation for that, the authors say that the graphene impedance is modelled with the R and L, and only mention the quantum capacitance once. In [74], the authors have used the transmission line model, and in [73], the authors have used a parallel RC. Although there are few examples, it is possible to observe that graphene has been modeled with a simple RLC circuit. In this work, graphene will be modelled similarly to these works with a series RLC, since it was the configuration that led to less error on the determination of its parameters.

3.6 Discussion

The TRL calibration provides one of the highest calibration accuracies. In this section, the application of the TRL calibration for the extraction of the RF characteristics of graphene was explored. The implementation of the calibration was described and simulated, as well as the parameters that negatively affect its accuracy such as thin contacts and lossy substrate. To obtain an accurate calibration, thick contacts and low loss substrate should be used to reduce the losses in the transmission line. In this case, considering the characteristics of the transmission line, the series resistance is around 0.8 Ω, the substrate conductivity 10 kΩ·cm, and the backgate contact around 730 kΩ, which can be used as a reference point for the calibration. Since thick contacts will damage graphene, a short length thin contact was added, and its impact on the extraction of the RF characteristics of graphene was demonstrated to be negligible. Furthermore, since graphene's conductivity changes according to its chemical potential, a backgate was added to characterize it for different potentials. The development of such calibration procedure to characterize graphene will allow us to further improve the knowledge of graphene's RF characteristics, paving the way to obtain tunable electronics either through biasing or biological functionalization. Through the calibration it is also possible to further extract and model graphene's RF characteristics making use of the pi model. Finally, the proposed calibration and extraction method are not limited to graphene and can be used with other 2D materials.

4 FABRICATION OF GRAPHENE DEVICES AND CALIBRATION STRUCTURES

4.1 Cleanroom facilities

A cleanroom is a facility that is designed and dedicated to the development of micro and nano-fabrication processes. It has various characteristics that must be controlled such as the purity of the air, humidity, and temperature. At International Iberian Nanotechnology Laboratory (INL), there is a 700 m^2 class 1000 cleanroom, with some areas being class 100, meaning that there are less than 1000 particles (≤0.5 μm) per cubic meter of air, with some areas where there are less than 100 particles (≤0.5 μm) per cubic meter of air.

The INL cleanroom is mostly equipped with machines that are destined for industrial processes development. It is possible to develop processes that include lithography, deposition techniques, etching techniques, and metrology and characterization techniques. More specifically, these are: nanolithography, photolithography, sputtering, CVD, dry etching, wet chemical etching, optical microscope, and scanning electron microscope. It is also equipped with a CVD dedicated for the growth of graphene and carbon nanotubes. The existing processes are optimized for the fabrication of 200 mm wafers, however, it is also possible to work with samples with sizes as low as a few mm. Therefore, the development of the fabrication process must take the existing conditions, recipes, and limitations into account.

4.2 Fabrication requirements from simulations

The simulation and implementation of the TRL calibration, as well as graphene's characteristics allow to define requirements for the fabrication of the calibration and measurement structures. Since RF measurements will be performed, to obtain an accurate measurement, it is necessary to have high resistivity substrate (for example, >10 kΩ.cm), and contacts with low resistance The calibration structures require that the signal trace of the longest transmission line has a resistance of around 0.8 Ω. In these devices, to attain this resistance, 5 μm thick copper contacts will be used, since such trace with the copper resistivity (1.7 μΩ.cm) will correspond to a resistance of around 0.8 Ω. The dimensions of the transmission line have been defined as a signal width of 50 μm, with a spacing of 30 μm to the ground plane which in turn has a width of 90 μm. The length of the calibration lines is 683 μm, 2181 μm, and 11614 μm.

Since the material of the DUT will be graphene and the contacts are 5 µm thick copper, it will be necessary to extend these contacts in length, with approximately 30 nm thick gold contacts. Furthermore, since graphene's conductivity is different for different chemical potentials, a backgate was included to characterize it for different gating voltages (and therefore chemical potential). It was determined that this backgate must have a minimum series resistance of 730 kΩ.

4.3 Backgate conductivity evaluation

The backgate contact must have a high series resistance, therefore, to avoid fabricating complex structures with extremely small width and thickness, a bad conductor is necessary. From the materials available in the cleanroom, it was determined that indium tin oxide (ITO) would be the best alternative, since it has a conductivity of 17 µΩ.cm. Since the exact conductivity of the INL's cleanroom is unknown, it was necessary to assess structure dimensions that allowed to obtain the desired resistance of 730 kΩ. Therefore, a simple fabrication process was undertaken as shown in Figure 33. To assess the dimensions needed, the structures were comprised of two square pads with a size of 150 µm, connected with a line with a length of 437 µm. The width of this line was changed from 0.5 µm up to 5 µm in 0.25 µm increments.

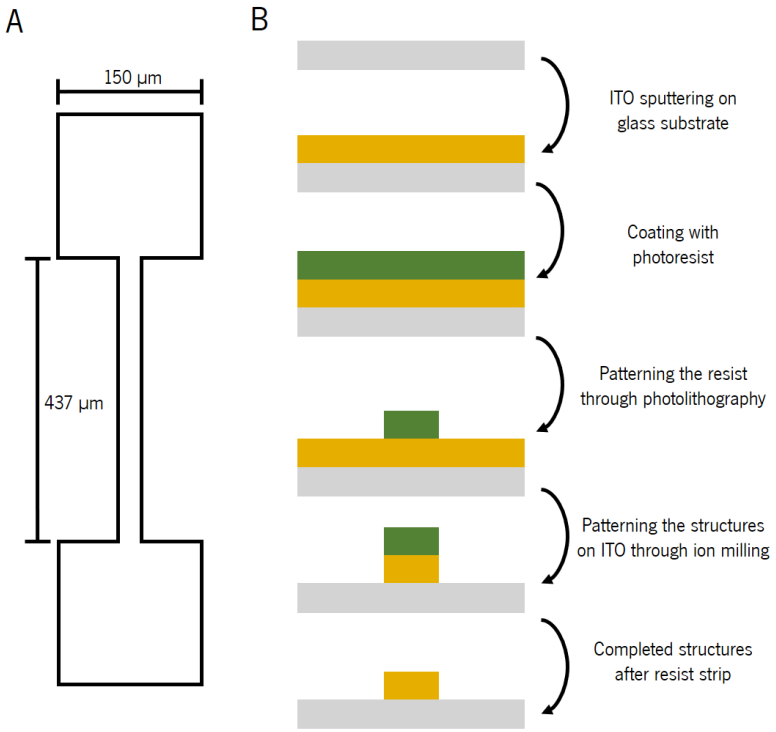


Figure 33 - Fabrication of ITO conductivity measurement structures: in (A), the structure's dimensions are shown, and in (B) is shown the fabrication steps as well as the corresponding cross section.

This process starts with glass substrates, since glass is not conductive and doesn't require an additional SiO_2 deposition. The substrates were cleaned with acetone, then isopropyl alcohol (IPA), then deionized (DI) water, and dried with compressed an N_2. Then, the ITO was deposited through sputtering in the Kenosistec Multitarget, where two samples were processed with a thickness of 10 nm and 20 nm. Then, the substrate was dehydrated in vacuum and treated with HDMS in the Vapour Prime Oven and coated with 600 nm of the AZ1505 resist in the SÜSS Microtec resist track. The resist was then patterned in the Heidelberg 2000 Direct Write Laser lithography (DWL) and revealed with the AZ400 developer in the the SÜSS Microtec track. The ITO was then patterned through physical etching in the Nordiko Ion Milling, which was performed at an angle of 130° for 120 seconds (240 seconds for the 20 nm thick sample), and at 165° for 45 seconds. Finally, the resist was removed in one low temperature cycle of O_2 plasma for 13 minutes in the PVA Tepla Plasma Asher. Figure 34 shows the fabricated structures as well as the measured resistance for each width.

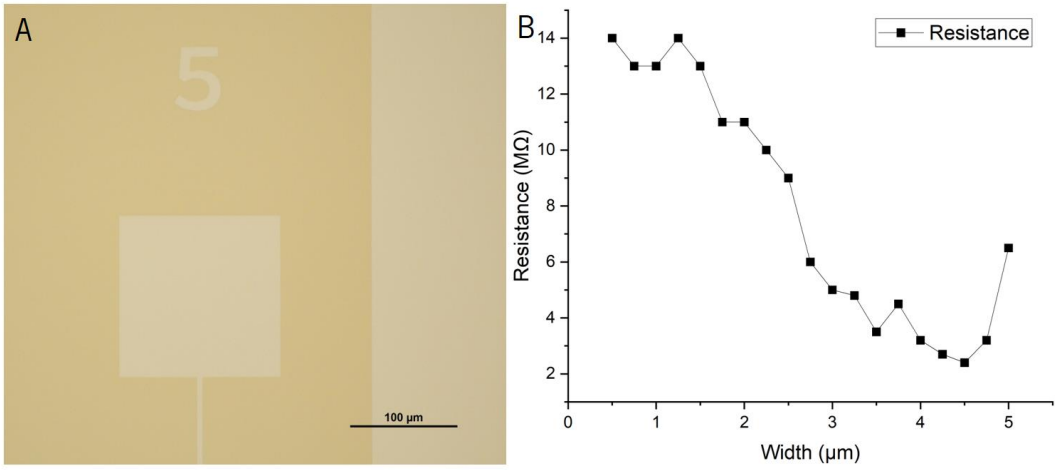


Figure 34 - Fabricated ITO contacts on glass substrate in (A), and measured resistance for the thickness of 20 nm for each width in (B).

After the fabrication of both 10 nm and 20 nm thick ITO structures, their resistance was measured. When measuring the 10 nm sample, its resistance unexpectedly high, overloading the multimeter. Therefore, to avoid complicating the measurement setup, the 20 nm thick sample was measured instead, and the results are shown in Figure 34 B. Taking the 3 µm wide device, its resistance is of approximately 5 MΩ, which is much higher than expected (would correspond to 1.2 kΩ, for the theoretical conductivity of ITO). This large increase in resistance can be explained by the exposure of the ITO, which is an oxide, to the O_2 plasma to remove the photoresist, which may have further oxidized the metal, increasing its resistance. This width corresponds to a higher than required resistance (5 MΩ when 730 kΩ were

required), however, it was used to fabricate the device, since it allows for the resistance to be further reduced due to the involuntary annealing of high temperature processes.

Since these were samples used to measure the characteristics of ITO, they weren't submitted to all fabrication steps. Therefore, the line of the backgate had a width of 3 µm and length of 437 µm, which was used in a test run with all the fabrication steps of the final device. The wafer was fabricated and the resistance of the backgate trace was measured and 22.8 kΩ were obtained. This means that the processes that the wafer is submitted to are reducing the resistance of the ITO. Among the various high temperature processes, an annealing at 500°C is performed to improve the copper conductivity, which may be affecting the ITO resistance. This means that the ITO resistivity is around 313 µΩ.cm, meaning that it is necessary to account for this change in resistance and update the backgate layout. A meander was designed with the acquired data with a width of 3 µm, 24 turns corresponding to a length of 20827 µm, and interconnects corresponding to a length of a length of 2191 µm, corresponding to a total length of 23018 µm, and is shown in Figure 35.

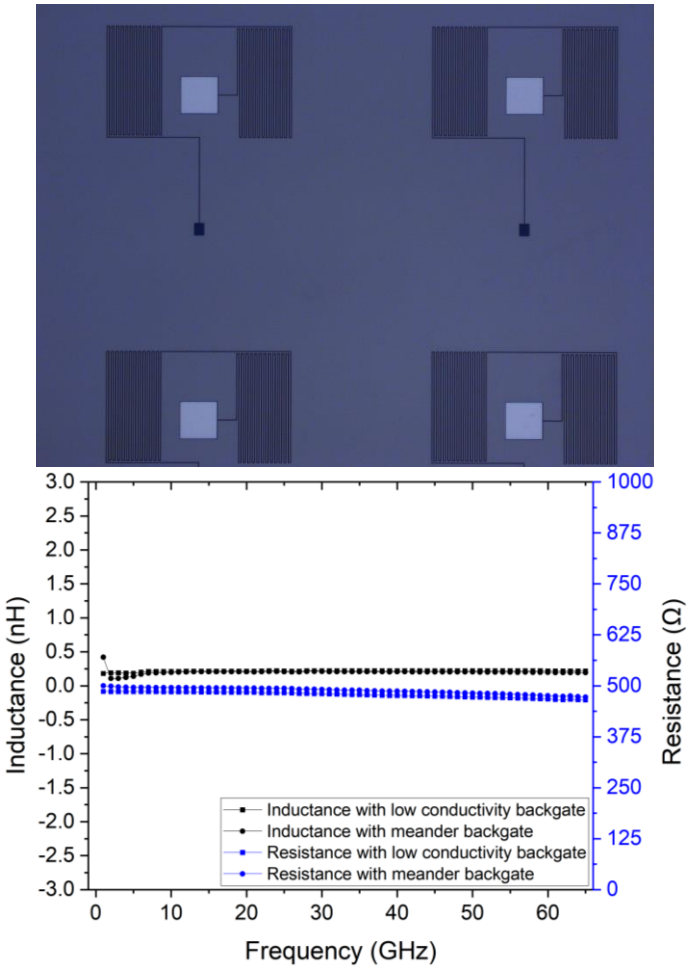


Figure 35 - On top is shown an optical microscope picture of the proposed meander with an aluminum contact, and on the bottom is shown the comparison between having a low conductivity backgate contact and a meander backgate.

Through the measured resistivity, and the meander dimensions, it is possible to conclude that a resistance of approximately 1.2 MΩ is obtained. This resistance is higher than required to take into account possible process and inter-device variations. After the fabrication of the new layout, a resistance of 1.94 MΩ was obtained, which fulfills the requirements. Furthermore, it is possible to observe that the differences between using a direct, low conductivity backgate and using a meander backgate with the available ITO are negligible. Therefore, the meander was used for the fabrication of the graphene devices.

4.4 Electroplating growth of copper

The sputter deposition of copper at the INL facilities has a very low deposition rate, meaning that sputtering 5 µm thick copper contacts takes a very long time. However, to obtain such large copper thickness, electroplating of copper can be used. This process is done through the A.M.M.T. electroplating system, which allows to deposit thick copper films. In Figure 36 A is shown the wafer holder which is designed for 8 inch wafers (approximately 20 cm), in B is shown the electrical spring loaded contacts that establish electrical contact with the wafer edges (while allowing for a diameter of 194 mm of the wafer to be exposed), and in C is shown the electrical current path of the holder.

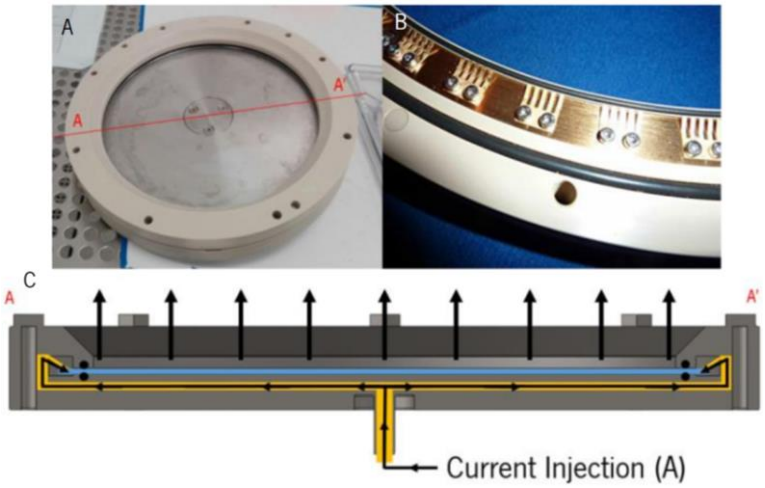


Figure 36 - In (A) is shown the wafer holder, in (B) is shown the electrical spring-loaded contacts, and in (C) is shown a cross section view of the electrodeposition wafer holder with the arrows depicting the electrical current path. Adapted from [75].

While in operation, the holder is connected to the machine, constantly rotating and placed inside a chemical solution that is constantly circulating to obtain a uniform deposition. Before starting the deposition and after it is completed, it is important that the wafer remains as little time as possible in solution, otherwise the metal will be etched. The fabrication process required for the electroplating of copper is shown in Figure 37.

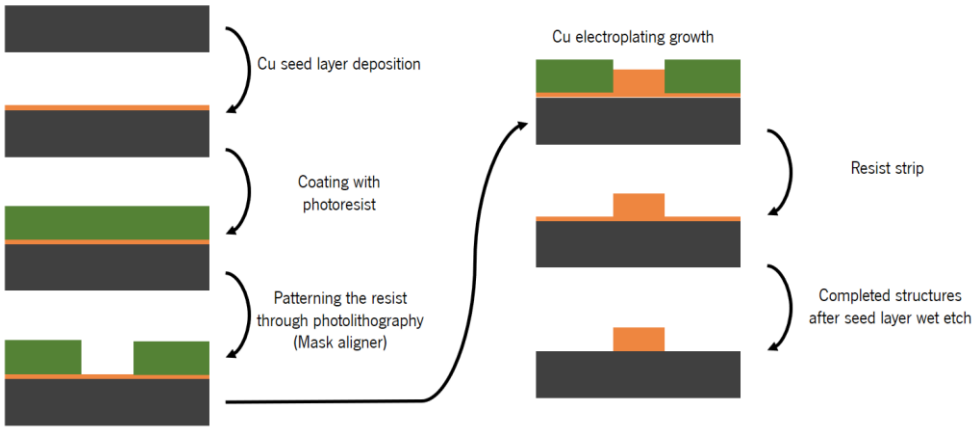


Figure 37 - Fabrication process for the electrodeposition of copper.

This process starts with a silicon wafer that has a silicon oxide layer (which is not shown for the sake of simplicity). Then, a 200 nm thick copper layer is sputtered which will be the seed layer and provide electrical contact throughout the whole wafer. Then, the wafer is coated with 10 µm thick AZ10XT photoresist which is loaded with a syringe in the SÜSS Microtec resist track, and an edge beam removal (EBR) is performed to make the electrical contacts available. Afterwards, the patterning is performed in the SÜSS MA6 mask aligner with a broadband exposure of 23 seconds and developed with AZ400K, and is shown in Figure 38 (the fabrication of the hardmask is described in Annex 1). Then, the wafer is placed in the A.M.M.T. for the copper electroplating, growing approximately 5 µm of copper. Then, the resist is removed, and the wafer is placed in copper wet etch for approximately 10 minutes, which provides an isotropic etch. This removes approximately 200 nm of copper in the whole wafer, which removes the copper layer and slightly etches the 5 µm thick copper trace.

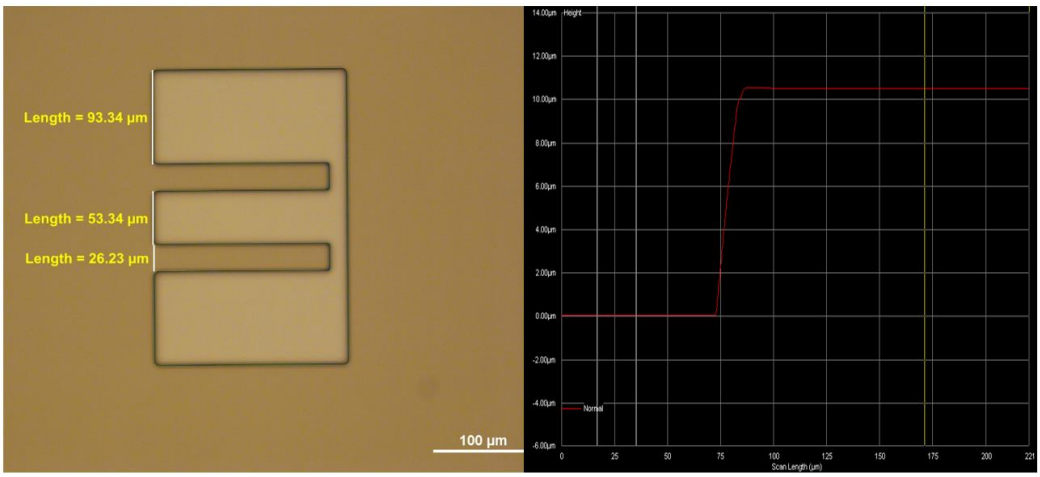


Figure 38 - On the left is shown the short standard after the lithography and developing as well as its dimensions, and on the right is shown the profilometer measurement of the resist thickness.

After performing the patterning of the resist, it is possible to analyze its characteristics. Through the optical microscope, shown in Figure 38 (left), it is possible to observe that the dimensions appear to be approximately 1.5 µm larger than intended. This can be due to a microscope measurement inaccuracy and, since the resist is very thick (and requires a longer exposure time), it may have walls that are not vertical but in a "V" shape. This can cause a slight change in the transmission line impedance, however, it is corrected in the calibration procedure. The thickness of the resist can be verified in the contact profilometer, shown in Figure 38 (right), and a thickness of around 10 µm is obtained, as expected. In Figure 39 it is possible to observe the results of electroplating growth of copper after performing the lithography.

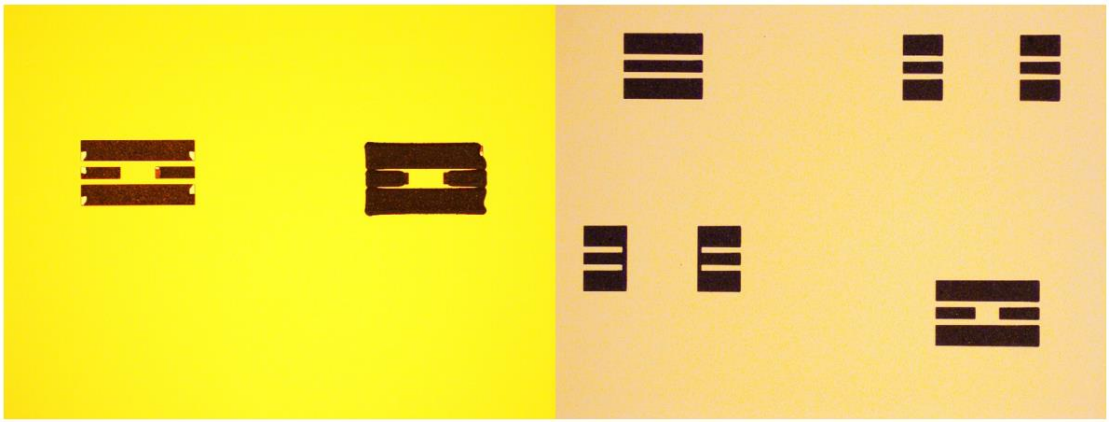


Figure 39 - Optical microscope images of the electroplating growth of copper before (left) and after (right) O_2 plasma treatment.

The Figure 39 shows optical microscope pictures of electroplating copper growth. It is possible to observe that on the left picture, there are zones where copper didn't grow and zones where the growth was higher than intended. To resolve this issue, 30 seconds of O_2 plasma were performed in the SPTS Pegasus, which is a deep reactive ion etcher, to remove possible photoresist residues and to increase the copper wettability. The results of the growth after this process step can be observed on the right picture of Figure 39, where the copper was grown as intended.

To perform the electroplating it is necessary to define its deposition conditions. Although the copper growth solution in which the substrate is submerged is controlled and replaced in regular time intervals, it can slightly change its properties over time. However, to control the copper growth rate, only the electrical current and process time can be tuned. To define these values, a recommended amperes per square decimeter (ASD) of 4 was used. Calculating the growth time is possible through:

$$Time = \frac{4At}{5I} \tag{27}$$

where A is the exposed area in dm², t is the target thickness in µm, and I is the current in mA. Since the exposed area was very small, a predicted a current of 2 mA for 360 seconds was necessary to grow 5 µm of copper. The profilometer measurement after this growth is shown in Figure 40.

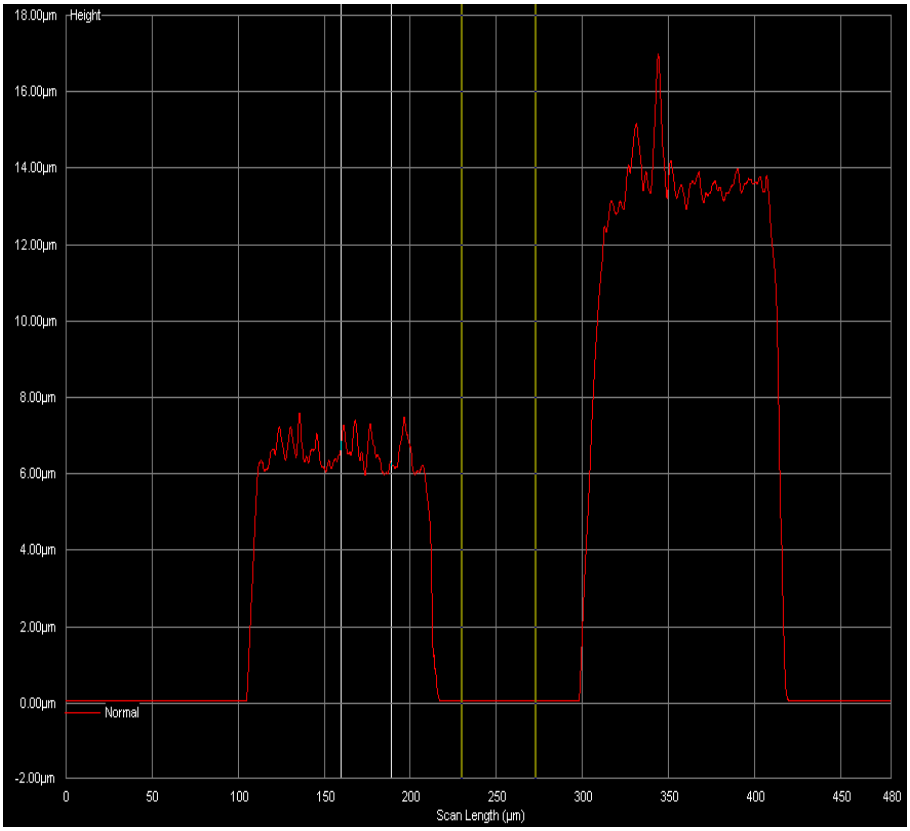


Figure 40 - Profilometer measurements after performing the growth of copper with 2 mA for 360 seconds.

Although the recommended 4 ASD was used, it is possible to observe that the deposition was irregular. Not only the grown height varied, in this example, from around 6 µm to around 13 µm, but the copper surface had a high roughness (larger than 1 µm grains).

These results can be originated by two characteristics: the minimum electroplating current, and the deposition area. Since electroplating is usually performed at higher currents (due to larger areas), the accuracy of the equipment in the mA range is limited, measuring 7 mA instead of the desired 2 mA. Furthermore, since the deposition is extremely small, it can cause different deposition rates in different places, since small differences/changes in the conductivity in different places can compound and result in large differences. To overcome these issues, it was necessary to increase the growth current and the total exposed area of the wafer (which in turn also increases the deposition current or time). To increase the exposed area, the EBR step of 3 mm was increased to 20 mm, while maintaining the same deposition rate, and the result is shown on the left picture of Figure 41.

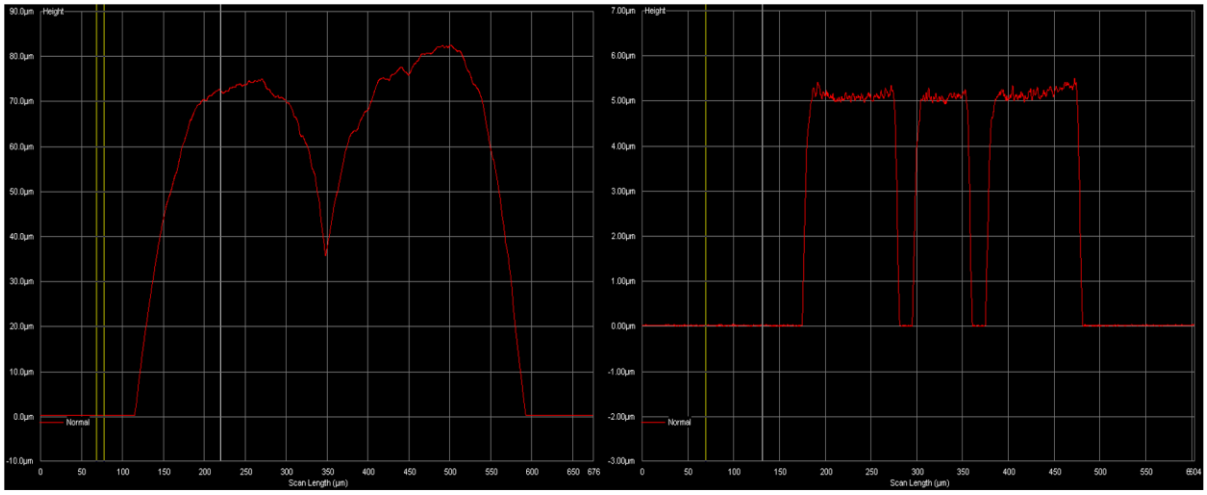


Figure 41 - Profilometer measurement after increasing the exposed growth area with an EBR of 20 mm (left), and after updating the growth parameters while maintaining the 20 mm EBR (right).

The thickness was much larger than expected, therefore, it was necessary to reduce the time and/or the current. After performing four more iterations of modifying the current and deposition time, the target thickness of 5 µm to 5.5 µm was obtained as shown on the right picture of Figure 41. To obtain a low roughness, a current of 100 mA was used, which is easily sourced and measured by the electroplating equipment, while being low enough to have a low roughness.

4.5 Etchant compatibility

The sputtering of gold on SiO_2 requires a previous deposition of another material such as chromium to serve as adhesion layer. For the deposition of the copper seed layer for the electroplating, chromium was also deposited to serve as adhesion layer between the gold and copper layers. This means that, upon the wet etch of the copper seed layer, chromium must also be wet etched. Upon verification of the wet etch part of the fabrication process, it was verified that the etchant that is usually used to remove chromium, chrome etch 18, also has a high copper etch rate. On the left picture of Figure 42, it is possible to observe the effects of performing the wet etch of chromium. It is possible to conclude that the etchant also almost completely removed the copper structures. One example of a proper etch are shown on the right picture of Figure 42, where it is still possible to observe the desired copper structures remaining intact in the center of the wafer.

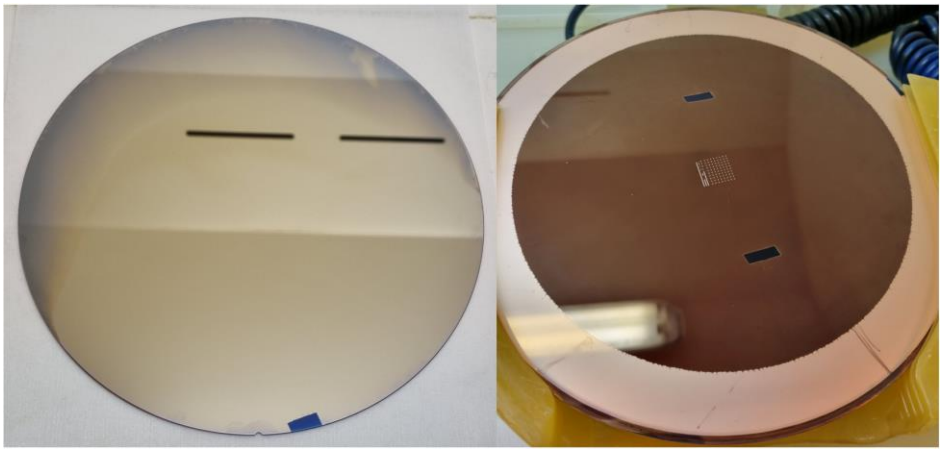


Figure 42 - Result of wet etching the chromium adhesion layer with chrome etch 18 on the left, and etching the seed and adhesion layer after updating the wet etching process on the right.

These results allow to conclude that it is necessary to update the fabrication process to allow the removal of the seed layer and the adhesion layer without damaging the fabricated structures. One possible solution would be to change the chromium etchant with another one that is compatible with the other metals, however, there was not another etchant available. Another alternative would be to change the adhesion layer to another material, and the corresponding etchant chemical. Titanium was chosen to test as the chromium replacement, which required to test the wet etch chemicals compatibility between the metals. The titanium etchant commonly used is H_2O_2 in which the three metals were submerged as shown in Figure 43.

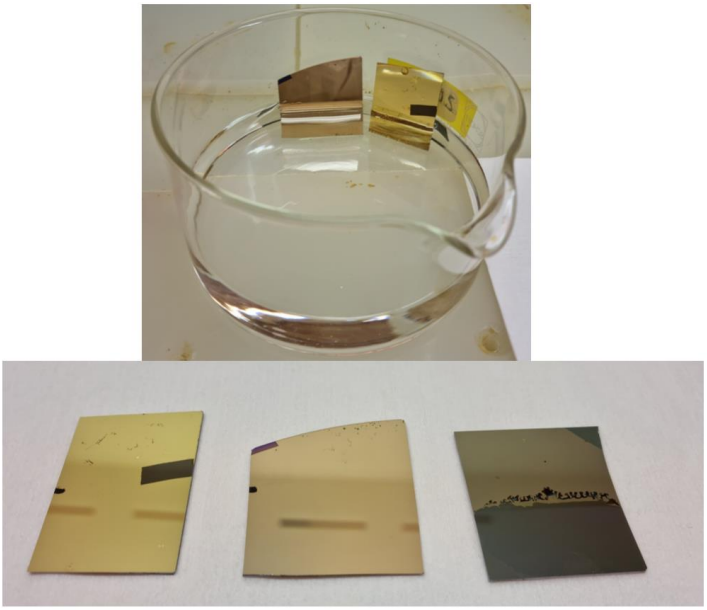


Figure 43 - Photograph of the H_2O_2 compatibility test on top, and the results for the three metals (gold, copper, titanium) on the bottom.

The duration of the test was 10 minutes, meaning that both gold and copper aren't etched by H_2O_2. It was possible to determine the approximate etch rate of titanium, which was around 2.5 to 5 nm/minute in ambient temperature. This allows to conclude that using titanium can be a solution to replace chromium as well as it is good etchant compatibility. The etch rate in ambient temperature also allows to etch the titanium adhesion layer in a controlled manner. However, it was later determined that it was slower, which was probably caused by sputtering copper on top of it. The last test necessary was the compatibility between the copper etchant and gold and titanium, which is shown in Figure 44.

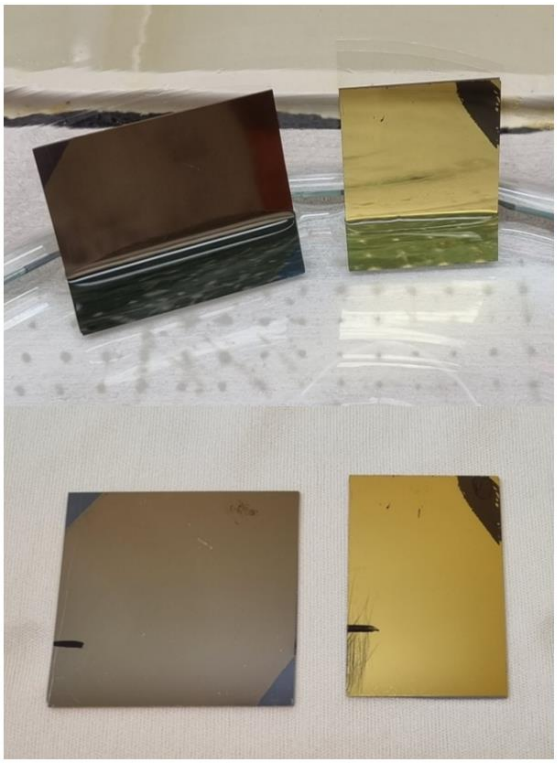


Figure 44 - Photographs of the compatibility test of copper etchant 49-1 with the metals (titanium and gold), showing the metal samples submerged (top) and after the test (bottom).

The etchant used is the copper etchant 49-1, in which titanium and hold were submerged, as shown in the top picture of Figure 44. It is possible to observe that none of the metals were etched by the copper etchant. This test also allowed to have a rough estimate of the copper etch rate. This was tested with a wafer that had the seed layer and grown structures on it. The wet etch was performed, and the resistance was measured between two points. After around 10 minutes of etching, the resistance had stabilized, meaning that an approximate etch rate of 0.33 nm/s were obtained.

These tests allowed to establish an adhesion layer that was compatible with the wet etch steps that were intended in the fabrication process. Since the titanium etchant only etches titanium, the copper

etchant only etches copper, and the gold is not etched by either, it is possible to conclude that titanium can be used as an adhesion layer in the fabrication process.

4.6 Graphene fabrication and techniques

4.6.1 Graphene growth

Graphene can be obtained through mechanical exfoliation of highly oriented pyrolytic graphite or through CVD growth [76]. Although the mechanical exfoliation produces graphene flakes in the 20 to 1000 μm range, with impressive performance, it is necessary to identify single-layer flakes, and it has got a throughput of a small number of transistors per sample [76]. Therefore, methods that allow to synthesize large areas of graphene have been extensively researched, with one of the most used techniques of obtaining graphene being the CVD growth on metal foils or SiC substrates [77]. Growing graphene on SiC substrates, however, is a technique that has a high cost, making it a big drawback to obtain large area graphene. Therefore, the preferred technique to obtain graphene is the CVD growth on metal foils, which allows to grow it in large areas, and to control the number of graphene layers by using a different metallic foil (for example, copper is used to grow monolayer graphene, while nickel allows to grow multilayer graphene). A drawback of this method is that it is necessary to transfer the graphene from the metal foil to the target substrate, which can introduce defects and degrade the graphene quality. Moreover, this usually requires a polymer assisted wet transfer which may leave some residues on graphene, thus also contributing to the reduction of graphene quality and mobility. Summing up, it is necessary to have a scalable production of graphene so that large scale fabrication of RF graphene devices and circuits can be obtained. Therefore, CVD grown graphene is the preferred method of obtaining graphene for RF applications [77], [78].

The equipment used for the growth of graphene to fabricate the devices is the EasyTube3000 CVD from FirstNano. It is a low-pressure CVD that uses a quartz tube and allows to grow graphene in a graphite box with a metal foil area up to 10 cm × 10 cm. The graphite confinement box is used to increase the growth rate and to protect the sample from contaminants originating from reactions with the quartz tube [79]. Since it is targeted to have monolayer graphene, a 25 μm thick copper foil (Alfa Aesar, purity 99.8%). This metal is used due to its low carbon solubility, making it easier to grow homogeneous single-layer graphene, due to its self-limited growth nature [80], [81], [82].

The growth process starts with an annealing at 1040 °C in an Ar (500 sccm) atmosphere at a pressure of 4.5 Torr. Afterwards, the deposition starts, which is done through a methane, hydrogen, and argon mixture, at 1040 °C and pressure of 4.5 Torr. The flows of the gases used in this process are 300 sccm of Ar, 100 sccm of H_2, and 1.5 sccm of CH_4, although they can be adjusted. Finally, after the growth time is finished, the quartz tube and samples are cooled down with a flow of 500 sccm of Ar until the room temperature is reached. The results of graphene growth can be observed in Figure 45.

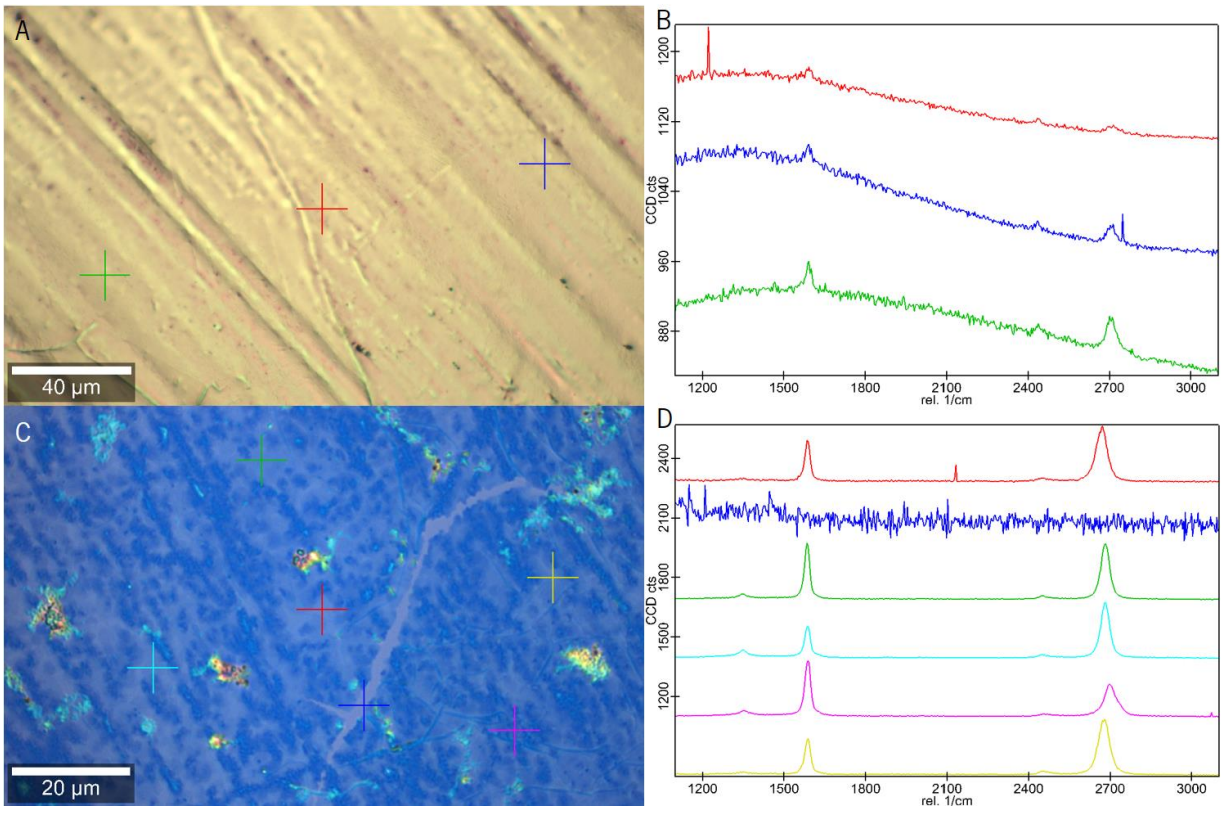


Figure 45 – Graphene images obtained with the optical microscope, and the respective Raman spectra: (A) shows the optical microscope image of graphene on copper, (B) shows the Raman spectra of the graphene on copper, (C) shows the optical microscope image of graphene on silicon, and (D) shows the Raman spectra of the graphene on copper.

After the growth of graphene on copper foil it is possible to analyze it through the optical microscope, where it is hard to observe the presence of graphene as shown in Figure 45 A. Through the acquisition of the Raman spectrum as shown in Figure 45 B, it is possible to determine wether graphene is present or not, although the reflectivity of copper makes it hard to acquire the Raman spectrum and determine the graphene quality and number of layers. As shown in Figure 45 C, by transfering graphene to a silicon substrate with silicon oxide (100 nm), it is possible to observe much easiliy the presence of graphene, where it is ruptured, where there are multiple layers. Through the Raman spectrum shown in Figure 45 D, it is possible to observe that there is no graphene in the dark blue measurement spot; there is

monolayer graphene in the red, yellow, and light blue spots; there is a bilayer in the green spot; and multilayer in the purple measurement spot. It is also possible to observe some residues that are most likely PMMA residues that result from the graphene transfer. The graphene growth used at INL produces monolayer graphene and is performed in the same equipment where nanotubes are grown.

4.6.2 Large graphene crystal flakes

Using metals as catalysts to grow high-quality large-area graphene through CVD is believed to be one of the most promising ways to achieve large-scale production [79], [83], [84]. However, this method usually produces a polycrystalline film that results from coalescing many graphene grains with a lateral dimension of 10-100 μm [85], [86], [87]. Although polycrystalline CVD graphene is continuous, it has grain boundaries (edges between adjacent graphene flakes) that increase the defects of the film, which degrades the thermal and electrical properties of graphene [88]. However, it is possible to reduce the number of defects of the film by increasing the graphene flake size and improve the mobility of devices such as transistors [89]. To achieve larger flake size and reduce the number of graphene boundaries, various methods and techniques have been proposed to improve graphene quality and reduce the nucleation during graphene growth [80], [81], [82], [88], [90], [91], [92], [93].

One of the techniques is oxygen-assisted CVD growth [94]. This technique introduces trace amounts of oxygen, which not only boosts graphene growth rate, but also allow to grow larger graphene flakes. Their dimensions can range from millimetre to centimetre scales, which reduces the nucleation density of graphene. Through this technique it is also possible to grow large-area graphene films by increasing the growth time and coalescing the graphene flakes [91]. A representation that was inspired in [95] is shown in Figure 46, where the copper foil with copper oxide is shown, as well as the effects of hydrogen and oxygen.

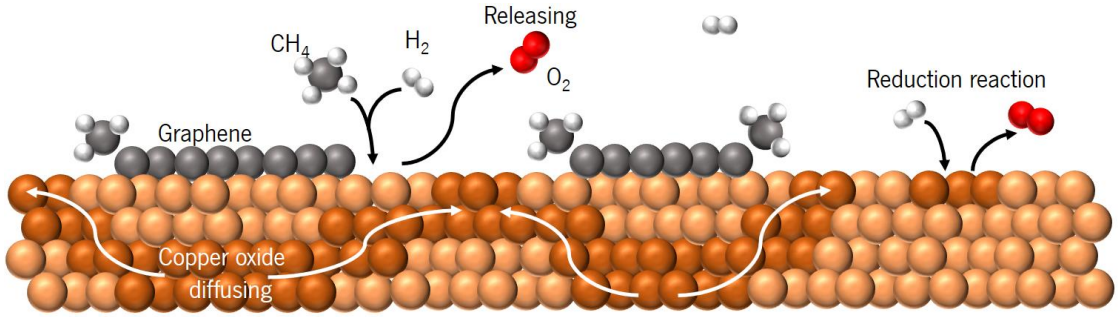


Figure 46 - Illustration of the copper foil with copper oxide, depicting the growth of large graphene single crystals, as reported in [95].

This process starts with the treatment of the copper foil, since it is comprised of grains with different orientations, which can reduce the quality of graphene through the introduction of defects in its lattice and determines the number and size of graphene boundaries [84], [88]. Furthermore, as discussed in [95], and show in Figure 47, the roughness of the copper foil can influence the transferred graphene, meaning that the copper topography is partially transferred to the target substrate and will collapse after removing the PMMA.

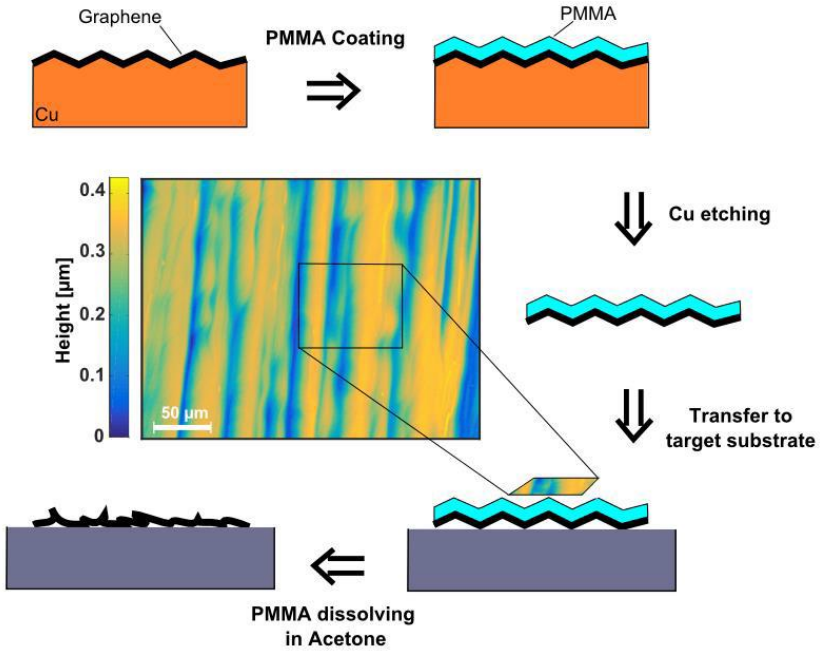


Figure 47 - Effect of the copper foil roughness on the transferred graphene [95].

A method to improve the quality of the copper foil is through using acidic and corrosive chemicals, which treats and homogenizes the roughness of the copper surface and cleans hydrocarbon matter residues, which has been confirmed in [92] to reduce the number of defects in graphene. The oxidized copper blocks carbon nucleation spots, which increases the distance between nucleation spots, and increases the available area for the growth of graphene flakes, thus allowing to obtain large graphene flakes [95]. This also allows to increase the methane concentration during growth, which increases the graphene growth rate.

Hydrogen is a co-catalyst for graphene growth its role is to activate the surface bonding of hydrocarbons so that graphene can grow, increases the graphene growth rate, and is an etcher that can be used to control the size and morphology of the graphene flakes [90]. However, it also influences the oxygen assisted CVD growth by reducing the oxidized copper and approaching it to a conventional graphene CVD process when it is exposed to hydrogen for a long period [90]. Since it is beneficial to

preserve the oxidation state of the copper oxide during the graphene growth, to maintain the CVD growth with trace amounts of oxygen, an oxygen source can be added such as a sapphire wafer (Al_2O_3). It was introduced in the graphite containment box on top of the copper foil with two graphite spacers to keep the disk from touching the sample. Through using the sapphire disk together with the graphite confinement box, it is possible to locally increase the oxygen concentration, protect the sample from SiO_x particles that may be released from the quartz tube, and keep the Cu vapor pressure. A schematic showing the placement of the sapphire disk, the copper foil, and the graphite spacers inside the graphite confinement box is shown in Figure 48.

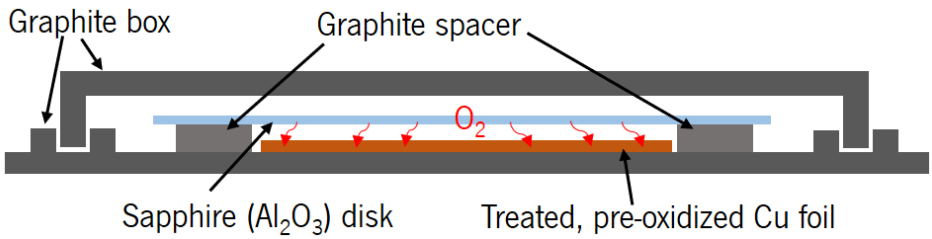


Figure 48 - Cross section of the graphite box with the copper foil inside, with the sapphire wafer (source of oxygen), and the graphite spacers.

Taking this information into account, it is possible to define and summarize the treatment and oxidation of the copper foil process, as shown in Figure 49. It starts with an ultrasound bath of the copper foil in a mixture of 10 ml 0.5 M of $FeCl_3$, 10 ml of 37% HCl, and 280 ml of DI H_2O. The foil is treated through this process for 1 minute, rinsed in a DI water bath for a few seconds, and dried with N_2. Afterwards, the foil is oxidized in air through a hotplate at 250°C for 30 minutes, with an ambient temperature of 20°C, and humidity of 50% (conditions of a class 100 cleanroom). Then, the copper foil is placed inside the graphite box and covered with a sapphire wafer, as depicted in Figure 48, to introduce trace amounts of oxygen and have an oxygen assisted growth. Then, graphene growth is undertaken, and large single crystal graphene can be obtained. The growth parameters can be tuned so that the size and morphology of these flakes can be controlled.

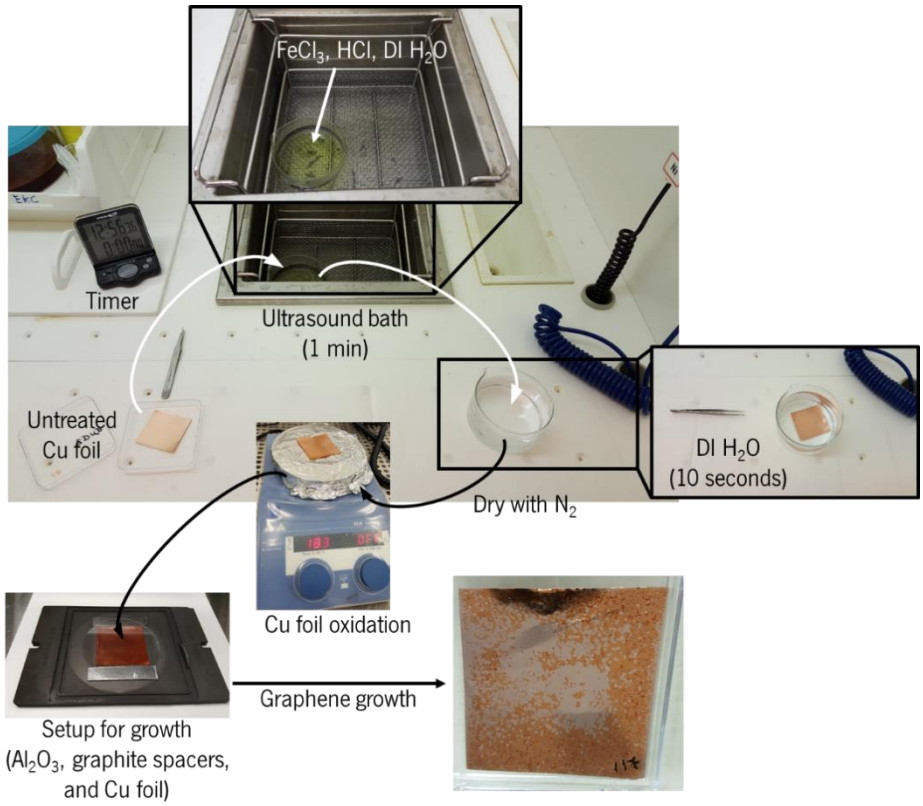


Figure 49 - Pre-treatment of the copper foil, oxidation process, and setup for the growth of graphene flakes.

After the growth of graphene, the copper foil can be oxidized to more easily measure and determine the size of the graphene flakes. Since graphene forms a protective layer and prevents the copper from oxidizing, it can be placed in a hot plate in air so that a color contrast can be obtained. Furthermore, it is possible to perform Raman spectroscopy to determine that graphene was grown. Figure 50 shows an optical microscope image obtained with the Raman spectroscopy equipment, and the Raman spectrum of the sample, where it is possible to observe the graphene peaks and confirm its growth.

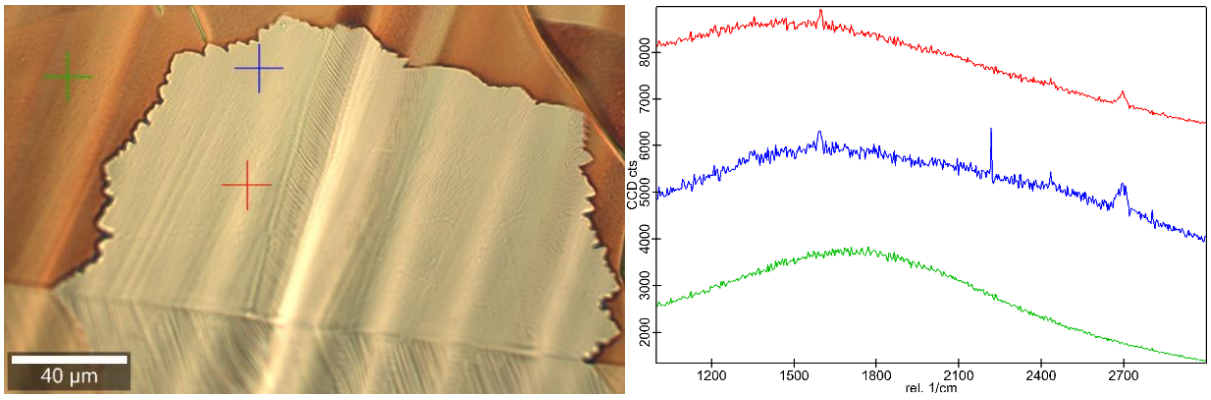


Figure 50 - Optical microscope image obtained with the Raman system on the left, and Raman spectrum obtained on the right.

Through tuning the flow of the gases used in the graphene growth, it is possible to tune the nucleation density, size, and shape of the graphene flakes. The influence of methane can be observed in Figure 51, where the size of the graphene flakes is shown. Increasing the methane flow allows to increase the size of the graphene flakes, however, it is at a cost of increasing the nucleation density [96], [97], meaning that the methane flow can't be increased too much. The increased size of the graphene flakes is due to a larger amount of available reactive species, which will allow for more flakes to achieve larger thermodynamically stable sizes [98].

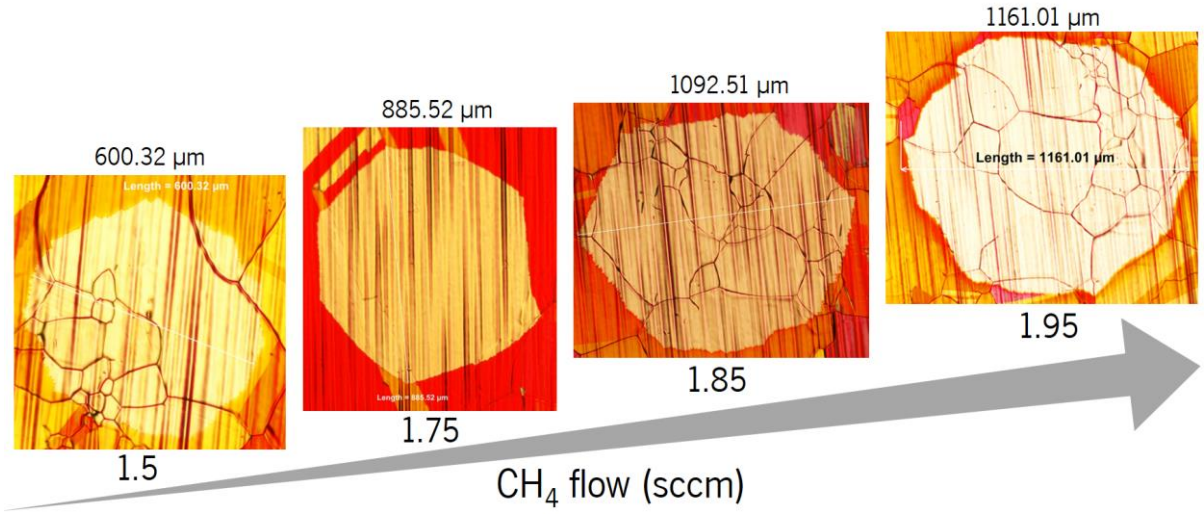


Figure 51 - Optical microscope images showing the effect on the size of graphene flakes when the CH_4 flow is increased in the growth of graphene.

The Figure 51 demonstrates the increasing size of the flakes with the increasing flux of methane, as reported in the literature. The recipes used for growth used a flow of 300 sccm of Ar, 350 sccm of H_2, a pressure 4.5 Torr, and a growth time of 90 minutes. Through increasing the methane flux from 1.5 sccm to 1.95 sccm, it was possible to increase the size of the graphene flake from 600.32 µm, to 1161.01 µm.

The influence of the flow of hydrogen can also be studied as shown in Figure 52, since it acts as a surface activator and etchant. The H_2/CH_4 ratio can be used to control the size and shape of the graphene crystals [90]. With an increasing H_2/CH_4 ratio, it is possible to change the shape of the graphene flakes from dendritic to hexagonal, however, if it is increased further, circular graphene flakes will be obtained.

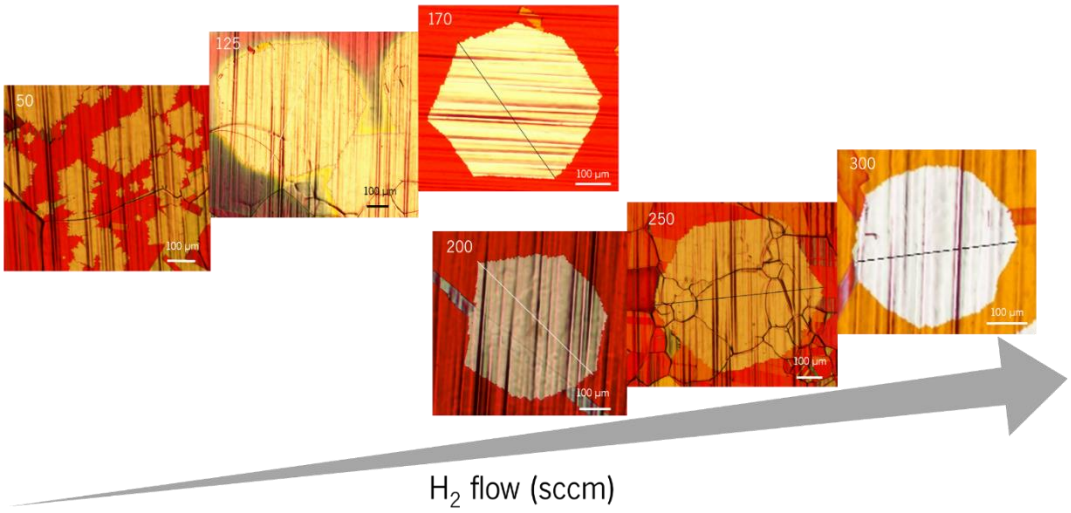


Figure 52 - Optical microscope images showing the effect on the shape of graphene flakes when the H_2 flow is increased in the growth of graphene.

In Figure 52 it is possible to observe this effect, where different samples were grown and the hydrogen flow was changed from 50 to 300 sccm. In these cases, the recipe used 1.5 sccm of CH_4, 300 sccm of Ar, a pressure of 4.5 Torr, and a growth time of 90 minutes. In the lowest hydrogen flow (50 sccm) the graphene shape was dendritic and through increasing the hydrogen flow, hexagonal shapes were obtained in the 125 to 200 sccm range. When the flow was further increased above 200 sccm, the graphene flakes became round. This behavior is expected since the etching effect of hydrogen is increased and attacks the flakes edges, as observed in the literature [90], [93].

However, obtaining stable optimal deposition parameters is very difficult, since these will change over time. This is caused by the condition of the CVD, which changes over time, as well as its cleanliness therefore it is not possible to define a graphene flake growth recipe. Finally, although large crystal flakes could be advantageous, monolayer continuous graphene was used. This is due to the lower coverage area of the graphene flakes, which would reduce the device yield, and due to the growth of carbon nanotubes after the previously reported graphene flakes growth process, which changed the deposition conditions of the CVD, which together time constraints, led to using continuous monolayer graphene.

4.6.3 Graphene transfer

The literature suggests several approaches for graphene transfer [99]. One of the most commonly used relies on poly(methyl methacrylate) (PMMA), which is very soluble in organic solvents such as acetone or toluene. Instead of using polymers, dry transfer approaches can be used to avoid using solvents to remove those polymers [99]. For example, thermal release tape and polidimethilsiloxane

(PDMS) can be used in dry transfers, which are removed through thermal heating [99]. However, not using solvents to remove the polymers can cause some residues to remain attached to the graphene surface. Approaches such as using hBN as a protective layer, or gold as a support layer have also been proposed in the literature [100], [101].

Although several approaches can be used, the most reliable and most used approach remains the PMMA assisted transfer [102]. This polymer is used as a supporting layer to maintain the integrity of graphene during the wet etch of the copper substrate and to provide mechanical stability during the transfer [103]. The transfer process has two sources of graphene contamination: metallic particles originating from the copper wet etch, and PMMA residues. These contaminations not only cause p-type doping of graphene, but also deteriorate graphene's electrical properties [104], [105], [106], [107] and reduce graphene's mobility up to one order of magnitude [108], [109]. Rinsing the PMMA coated graphene in a DI water solution with 1-2% of HCl can reduce the effects of the metallic contamination from $FeCl_3$, which is the copper etchant used to remove the copper substrate [110].

The transfer is also affected by the PMMA, where several approaches have been proposed to remove its residues. Acetone has been heated to increase its PMMA dissolution power [111], and solvents such as anisole, chlorobenzene, and chloroform have been used, although it has been agreed that these residues can't be totally removed [112]. Other approaches have been proposed such as using two PMMA layers to reduce the residues [113], and reduce the number of cracks in graphene [114]. In other cases, laser cleaning [115] or thermal degradation [116] have also been proposed to decompose and remove PMMA.

According to [103], higher weight percentage PMMA solutions form thicker supporting layers and are preferred due to their mechanical robustness, however, leave significant residues on graphene. The authors have demonstrated, as shown in Figure 53, that the increasing PMMA residues with different weight percentages and different average molecular weight (AMW), increases the amount of residues after graphene transfer.

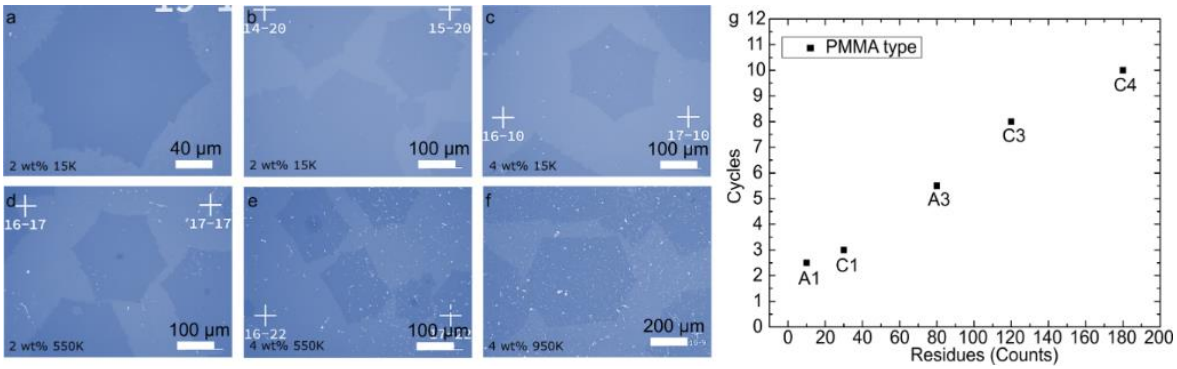


Figure 53 - Analysis of the PMMA residues after the graphene transfer for different PMMA mixtures [103].

Although annealing processes, or even UV radiation have been proposed to help remove these residues, the authors claim that it must be taken into account that thermal treatments can be counterproductive, since they can increase polymerization, harden the PMMA residues, thus making it harder to remove the residues [103]. Therefore, the authors propose optimizing the PMMA transfer through balancing the AMW of the PMMA mixture. The optimized PMMA mixture the authors obtained is comprised by a 2:1 ratio of PMMA-550k and PMMA-15k in anisole (3%wt), respectively. This mixture was used for the transfer and fabrication of the graphene devices, which is represented in Figure 54. It has a high mechanical strength and flexibility, allows to attain a "reliable transfer with negligible contamination level", while being easily dissolved, and allowing having no high temperature post-treatment.

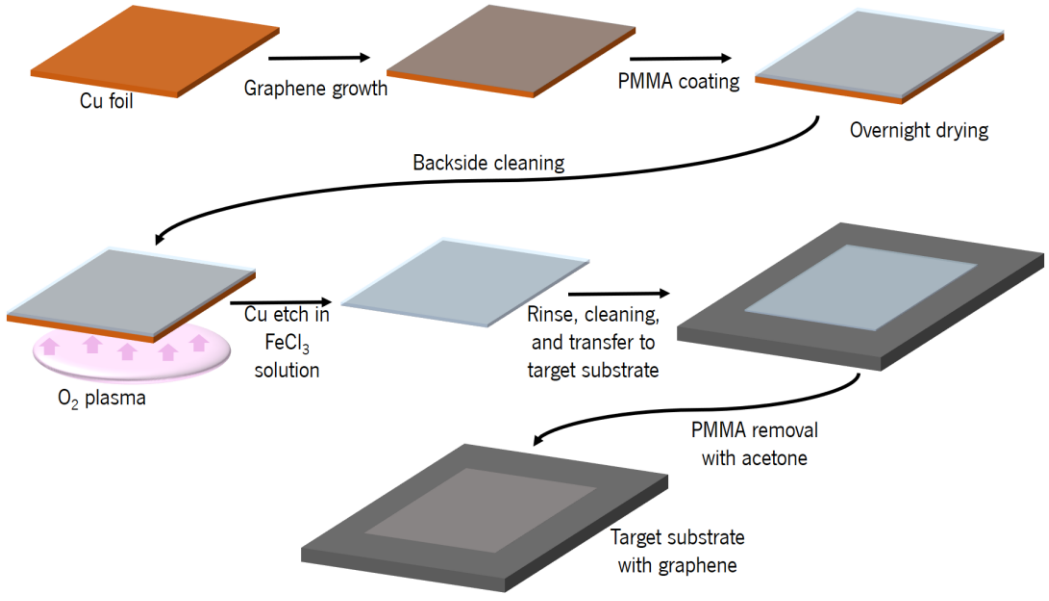


Figure 54 - Diagram of the graphene transfer procedure.

To perform the transfer shown in Figure 54, it is necessary to have previously prepared three solutions: the PMMA mixture, the $FeCl_3$ etchant solution, and the 2% HCl solution. Since the PMMA mixture

is 3%wt and has a 2:1 ratio of PMMA-550k and PMMA-15k, it is possible to weigh 2 g of PMMA-550k, 1g of PMMA-15k, and 97 g of anisole. This is then stirred with a magnetic mixer for 24 hours. The $FeCl_3$ etchant solution used is 0.5 M, which means that 326 g of $FeCl_3$ powder are diluted in 2 L of DI water. As for the 2% HCl solution, 108 ml of 30% HCl were diluted in DI water, making a total volume of 2L.

The diagram of the graphene transfer procedure shown in Figure 54 starts with the graphene grown on the copper foil. Afterwards, the graphene coated copper foil is spin coated with the described PMMA mixture in the SÜSS Microtec resist track. The PMMA is left to dry overnight, and then, the backside of the copper foil is cleaned to prevent graphene or other debris grown on the backside to be present in the target susbtrate after the transfer. To perform this cleaning, the copper/graphene/PMMA stack is placed in a wafer with the backside facing up, and submitted to 8 cycles of 30 s each, of O_2 plasma in the Roth & Rau Thermal CVD (200 W RF power, 250 sccm of O_2, 0.4 mbar). Afterwards, the wet transfer procedure starts with the wet etch of the copper foil by floating the copper/graphene/PMMA stack on the 0.5 M $FeCl_3$ solution with the copper facing the solution (PMMA) facing up. This step can usually take up to 2 hours, but to prevent fragilizing the graphene/PMMA stack, it should be taken out as soon as all the copper is dissolved. As soon as this step is completed, the graphene is picked up with a previously cleaned SiO_2 fishing tool and transferred to clean DI H_2O for an initial rinse. After around 5 minutes, it is transferred again to another clean DI H_2O, for 5 to 10 more minutes. Then, it is transferred to the 2% HCl solution for around 30 minutes. The 5 minute DI H_2O rinse and 30 minute 2% HCl solution are repeated 3 times. Finally, it is rinsed in DI H_2O and transferred to the target substrate (which was previously dehydrated in vacuum and treated with HDMS in the Vapour Prime Oven). The substrate is then left vertically drying overnight in the wet bench. The final step of the transfer is the removal of PMMA, which starts with a 2-3 hour acetone bath, an IPA rinse, and finally a water rinse and drying with N_2. These last steps must be performed carefully in order not to damage the graphene.

Another characteristic that must be taken into account when transferring graphene is the topology onto where it is being transferred to. In the case of performing the RF calibration as discussed, thick metallic contacts are required, meaning that graphene can break due to the large difference in thickness. Therefore, to take into account that graphene breaks, thin contacts can be used to extend these ones as shown in Figure 25. Two examples of transferring graphene for such type of contacts are shown in Figure 55, where for a contact thickness of 5 µm of copper, 30 nm thick gold contacts were extended 5 µm and 35 µm.

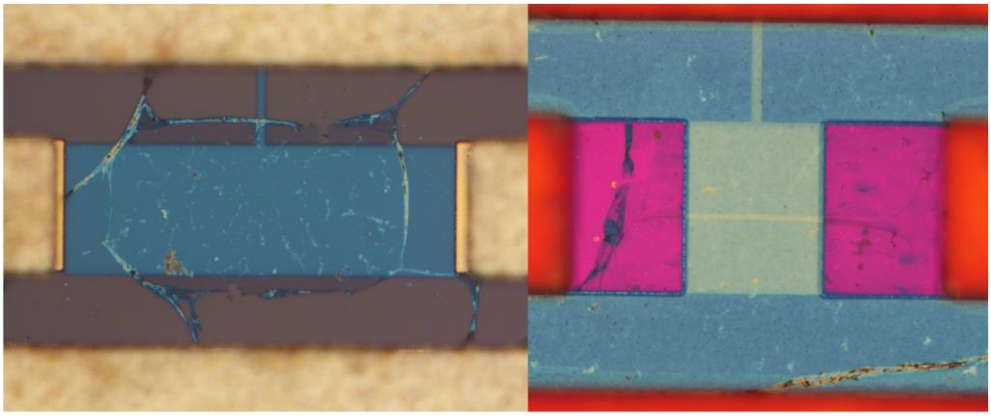


Figure 55 – Extending graphene contact length 5 µm (left) and 35 µm (right) and the difference in graphene contact.

Although there is aspect ratio of 1:1 for the 5 µm length gold contacts, it is possible to observe that graphene still breaks and rolls back to a distance of around 25 µm to 30 µm. To solve this issue, longer (around 35 µm in length) contacts were fabricated, where it is possible to observe that although graphene breaks and even rolls back, contact can still be made.

4.6.4 Reducing graphene contact resistance

Due to the physical nature of graphene, it is usually necessary to use extra metallic contacts to develop graphene devices. However, the contact resistance between graphene and the metal contacts is one of the most limiting factors for the performance of these devices. For the sake of example, in the case of graphene transistors, the factor that degrades their performance the most is the contact resistance [117], especially when the gate length decreases.

Several approaches have been proposed to reduce the contact resistance, such as engineering the contact work function [118], annealing the metallic contacts [119], cleaning graphene with UV or ozone plasma before contact deposition [120], antidot (holes in the metal/graphene intersection area) fabrication [121], introducing holes or stripes with different shapes in the metal/graphene intersection area [122], using gold as the support layer for graphene transfer [123], and even sandwiching graphene between two metals [124]. However, it has been reported that graphene's contact resistance depends on the contact width and not on the contact area, suggesting that there is current crowding at the edge of the metal contact with graphene [125]. Contact resistances of graphene with different metals have been reported in the literature and are shown in Table 3.

Table 3 - Graphene-metal contact resistivity, adapted from [77]

Metal/Graphene	ρc Ω μm	Reference
Ni	500	[126]
Ti	>1000	[127]
Ti/Pt/Au stack	100	[128]
Cr/Pd/Au stack (1D edge contact)	100	[129]
Cu (Cuts patterned)	125	[58]
Pd (Cuts patterned)	457	[58]
Pd	185-900	[130]

The technique that is typically used at INL for the fabrication of the graphene contacts is patterning the contacts and then transferring graphene on top of the contacts. This allows having a less complex fabrication process and avoids performing fabrication processes on top of graphene, thus preventing damaging it. The metal used is gold, since it provides one of the best contact resistances and is less prone to oxidation. Therefore, the devices fabricated in this work will have gold contacting graphene.

4.7 Fabrication process for graphene devices and calibration structures

According to the materials characteristics and the dimensions requirements reported in this section, the fabrication process was developed. This fabrication process was projected to use standard commercial 8-inch wafers processing equipment, and a representation of the targeted device is shown in Figure 56.

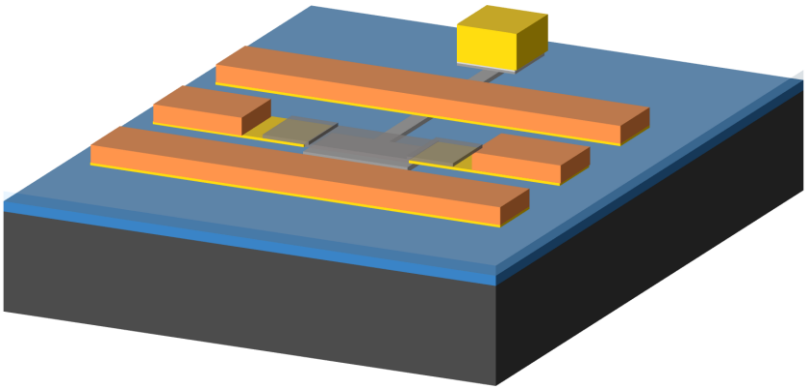
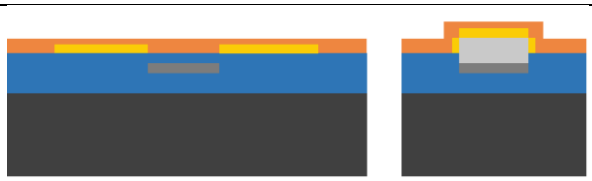


Figure 56 - 3D representation of the desired graphene device.

It is possible to observe that the device is comprised by a silicon substrate (with high resistivity), and 100 nm of SiO_2, in which a 20 nm thick ITO gate was fabricated (buried in 50 nm of SiO_2). This gate

has an external contact that goes through the oxide layer, and is made of thick metal, with gold plating. The contacts for the CPW are made of 20 nm of gold on top of which 5 µm of copper were grown. These leave around 35 µm of gold that is used to contact graphene that is placed in the middle of the device. The fabrication process of this structure is displayed in Table 4, where some steps were omitted.

Table 4 - Developed fabrication process

Step	Brief description	Cross section
1	Start with 10 kΩ.cm Si substrate; deposit 50 nm of SiO_2	
2	Lithography for lift-off and sputtering of 20 nm of ITO	
3	Perform ITO lift-off, lithography for lift-off, and sputter AlSiCu for back gate contact	
4	Perform AlSiCu lift-off, deposit 50 nm of SiO_2	
5	Remove SiO_2 from the gate contact, lithography for lift-off, deposit 20 nm of Au	
6	Perform Au lift-off, deposit 200 nm of copper	
7	Lithography for electroplating, perform copper eletroplating	

8	Remove the resist, wet etch the copper seed layer	
9	Graphene transfer	
10	Lithography for graphene patterning	
11	Pattern graphene with O_2 plasma, remove the resist	

This fabrication process starts with a silicon wafer that has a resistivity of 10 kΩ.cm on top of which 50 nm of SiO_2 are deposited. This process is performed in the SPTS PECVD and completes the step 1.

Afterwards, the wafer was coated with PMMA 617.03 1+1 679.04 to perform the lithography in the Vistec e-beam lithography, with an exposure of 850 $\mu C/cm^2$. The reasoning for the previously described PMMA types is that the first one (the lower layer) has a lower molecular weight, therefore shorter strands than the second one. The electrons used in the lithography will break up the bonds, meaning that the lower layer will be removed more easily, thus replacing lift-off resist. Afterwards, 20 nm of ITO were sputtered in the Kenosistec Multitarget, completing the step 2.

The lift-off was then performed by placing the wafer in acetone for 2 hours and then placing it for 5 minutes in the ultrasound bath. To maintain the ITO test conditions, the wafer was placed in the PVA Tepla plasma asher, performing one cycle of low temperature O_2 plasma for 13 minutes. Then, the backgate contact, a liftoff was performed. The process is started by priming the wafer with HDMS in the Vapour Prime, and coating the wafer with 600 nm of AZ1505 resist and performing the soak treatment for lift-off. Then, this layer is patterned in the DWL with 20% more intensity and developed with AZ400K. To deposit the contacts, 3 layers of TiW/AlSiCu/TiW with 15/100/30 nm thickness were deposited with a pre-etch treatment, which is performed in the Timaris FTM sputter, and concluding step 3.

The lift-off was performed with an acetone bath of 2h and 5 minutes of ultrasound bath, followed by 1h30 and 5 minutes of ultrasound bath, followed by a DI H_2O rinse to remove any remaining particles. Afterwards, to bury the gate, 50 nm of SiO_2 were deposited in the SPTS PECVD, concluding step 4.

Since the oxide is deposited throughout the whole wafer, it was necessary to remove it. This process was performed by priming the wafer with HDMS, coating it with 2200 nm of AZP4110, and performing the lithography. Then it was developed with AZ400K, and the SiO_2 was etched in the SPTS APS, the result is shown in Figure 57.

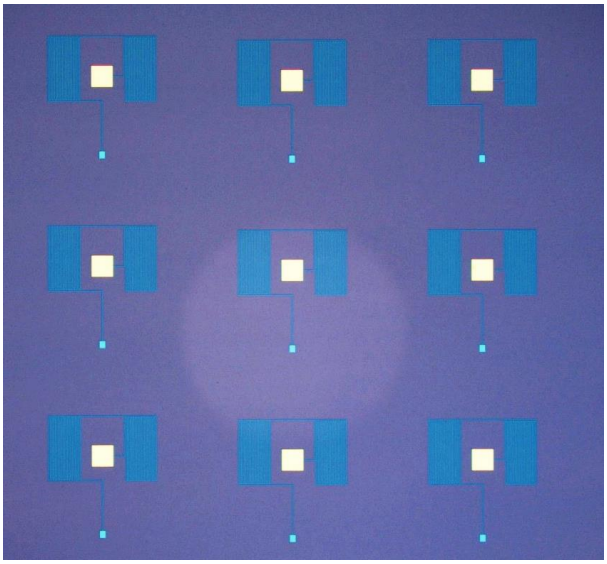


Figure 57 - Optical microscope image of the backgate, meander, and contact after depositing SiO_2 and opening the contact.

Although a predicted etch time of 6.07 seconds was necessary, a 25% increment was factored in and rounded up to a total of 10 seconds, thus performing some overetch. Since TiW would be below, it is a stop layer for this process step. The resist was then removed in the plasma asher with an O_2 plasma with the recipe Resist_strip_T110 for a total duration of 6 minutes and 2 seconds. Afterwards, to fabricate the gold contacts, a lift-off will be performed. This starts with the heating of the wafer up to 200°C in the Vapour Prime (without HDMS), and coating with Lor5b. Then, a coating with 600 nm of AZ1505 is performed, followed by the lithography, and revealed with AZ400K. Then, 10 nm of Ti are sputtered as adhesion layer, and 20 nm of Au are sputtered, both in the Kenosistec, completing the step 5.

To perform this liftoff, the wafer is placed in mrRem500 at 65°C for 1 hour, and then 30 more minutes in ultrasound. The result of this fabrication step is shown in Figure 58.

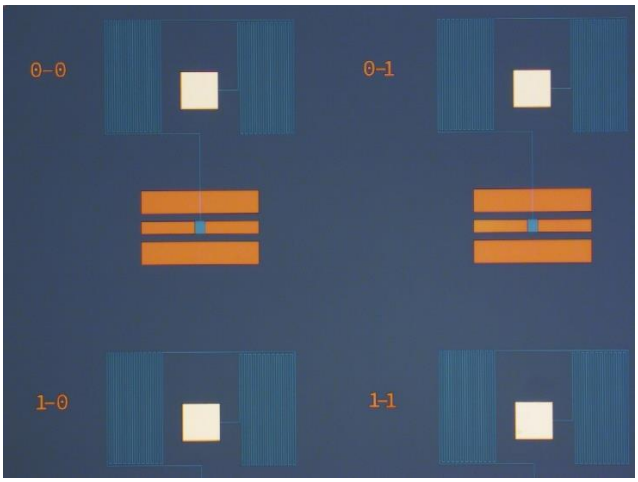


Figure 58 - Optical microscope image after completing the fabrication of the gold contacts.

To deposit the seed layer for the electroplating of copper, the alignment marks area were covered with kapton tape, and 20 nm of Ti and 200 nm of Cu were sputtered in the Kenosistec, completing the step 6.

Then, the wafer is primed with HDMS, and 10 μm of AZ10XT were coated. The lithography was performed in the mask aligner, with broadband light for 23 seconds, and developed with AZ400K. Then, 30 seconds of O_2 plasma were performed in the SPTS Pegasus to remove possible photoresist residues and to increase the copper wettability. Then, the copper electroplating was performed in the A.M.M.T., with a current of 100 mA for 8057 seconds, thus finishing step 7. The result of this step was shown in Figure 41.

The resist used for the electroplating of the copper contacts was removed with acetone, followed by an IPA rinse, which was followed by a DI H_2O rinse. Then, the wet etch of the seed layer was performed. The 200 nm of copper seed layer were removed by placing the wafer facing down for 10 minutes in copper etchant 49-1. The resistance between two points was measured throughout the etch procedure, which were used to determine that copper was completely removed and is shown in Figure 59.

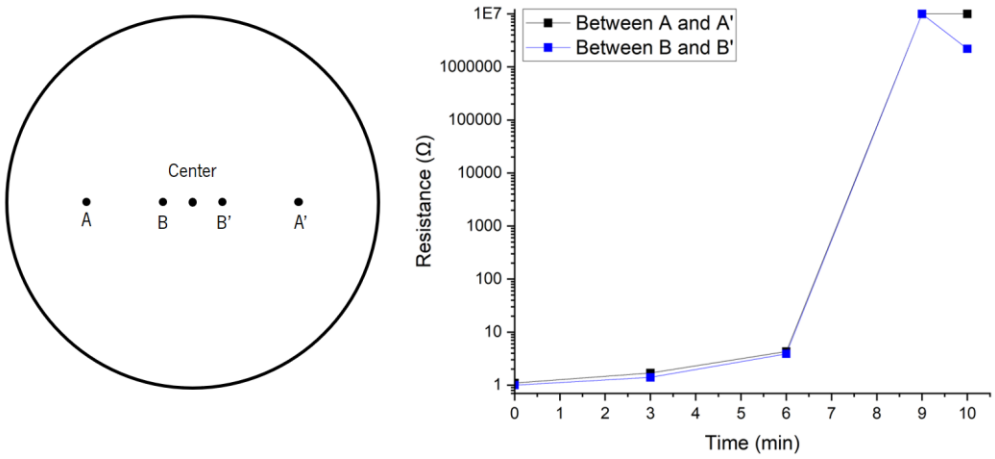


Figure 59 - Evolution of the resistance between two points: outside of the alignment marks between A and A' (approximately 4 cm from the center), and near the edges of the device between B and B' (approximately 1 cm away from the center).

It is possible to observe that the resistance increases with the etch of the copper seed layer as it becomes thinner. Two points were used to measure the evolution of the resistance: outside of the alignment marks which are approximately 4 cm from the center, totaling a distance of 8 cm, and near the edges of the device which are approximately 1 cm away from the center, totaling a distance of 2 cm. These points were measured with a handheld multimeter and measured by hand, however, it allows for an accurate enough measurement for this purpose. In the final minutes, some of the resistances were so high that the multimeter couldn't measure them, therefore, to plot these results, a resistance of 10 MΩ was plotted instead. In the last minute, the resistance dropped, which could be the titanium starting to be exposed (instead of copper oxide), or a measurement condition (since these were performed by hand) that allowed to measure a 2.2 MΩ resistance. In either case, it is possible to conclude that the copper was completely etched.

Then, the wet etch of the Ti adhesion layer (of the copper seed layer) was etched with H_2O_2 with the wafer facing down. This step took a total of 56 minutes, during which the resistance of that layer was measured to determine that the Ti layer was completely removed. These measurements are shown in Figure 60, where three different cases were evaluated. The first case is measuring the resistance between two points of the substrate which have the Ti adhesion layer and shouldn't be conductive after removing it. The second one is measuring the resistance between two adjacent copper lines, which have a measurable resistance between them due to the Ti layer and shouldn't have electrical connection when it is removed. Finally, the resistance inside of a gold contact should be very small, indicating a complete Ti layer removal.

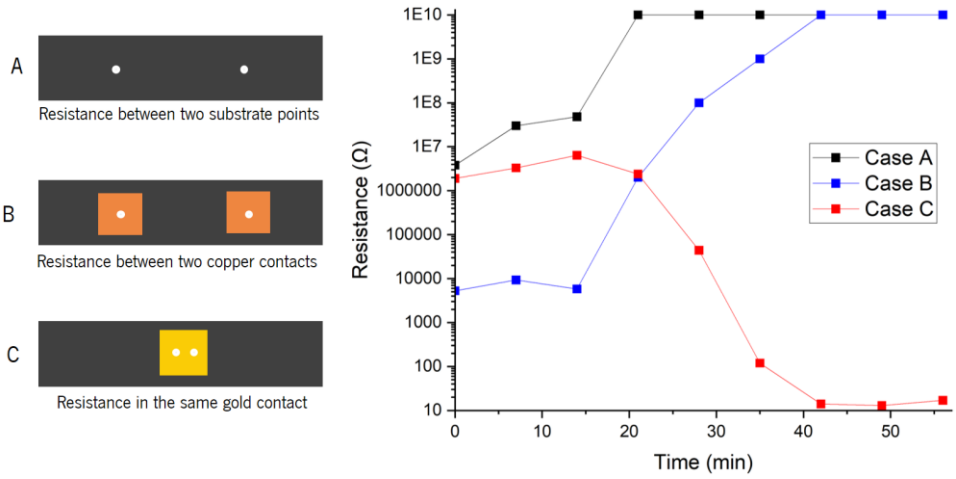


Figure 60 - Evolution of the resistance between two points in three different locations: in the substrate, two adjacent copper contacts, and the same gold contact (left); and the evolution of the resistance in those cases (right).

In this graph, when the multimeter was overloaded, a resistance of 10 GΩ was plotted for easier visualization. Analyzing the evolution of the resistance for each case, it is possible to conclude that titanium was completely removed. In the first case, there is a measurable resistance since the Ti layer is still present on the substrate and as it is etched the resistance increases, since the layer thickness reduces and SiO_2 (which is not conductive) becomes exposed. In the second case, a Ti layer connects two adjacent copper contacts, since it was used to fabricate them. The same as in the first case happens: there is a measurable resistance in the beginning but as the etch progresses, the resistance is increased up to the point that it can't be measured (since the copper contacts are not connected), thus suggesting that the Ti layer was removed. Finally, in the third case, the resistance was measured inside a gold contact that was covered in Ti. Since a strong oxidizer is used, it oxidizes the titanium, meaning that a higher resistance than expected is measured. When it is removed, only gold remains in the contact, meaning that a low resistance is expected. It is possible to observe this behavior in the evolution of the resistance measured, meaning that the Ti adhesion layer was completely removed.

Although there's also a Ti adhesion layer below the Au and Cu contacts, there is not a problem of under etching and causing these contacts to lift off. This is because this wet etch step removes 20 nm of Ti, meaning that a maximum of 20 nm of under etch would occur in structures that are several micrometers in width. Then, the wafer was annealed in vacuum at 500°C for 60 minutes, achieving the required resistance of 0.8 Ω for the long signal line (the resistance of the copper line was 5.4 Ω, the resistance of the measurement cables and probes was 4.6 Ω), concluding step 8, and shown in Figure 61.

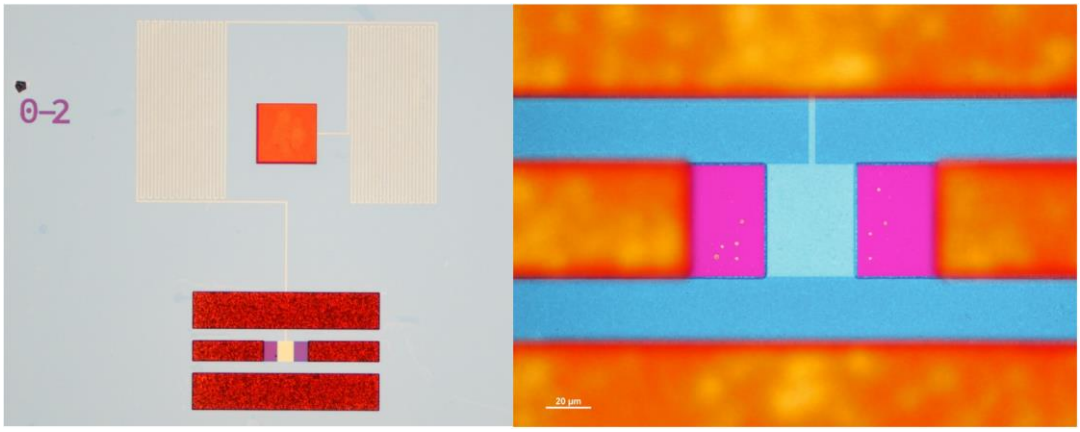


Figure 61 - Optical microscope image of the fabricated device after electroplating copper and etching the seed layer, before annealing (left) and a close-up after annealing (right).

Afterwards, graphene was transferred to the wafer with the previously described procedure, concluding step 9. Then, a coating with 1035 nm of AZ1505 was used to pattern resist. This thickness was used due to the large topography of the copper contacts. Since these are thick, the coating in the DUT area can become very thin in some places, causing it to be easily removed during the etching of graphene and making the devices inviable. The lithography is then developed using AZ1505, concluding step 10.

Finally, graphene is usually etched in the SPTS ICP. However, since this equipment was malfunctioning and under maintenance, it was patterned in the SPTS APS using O_2 plasma for 15 seconds. Then, the resist is stripped by submerging the wafer in acetone for 3 hours, followed by an IPA rinse and a DI H_2O rinse, concluding step 11 and the fabrication of the graphene device as shown in Figure 62.

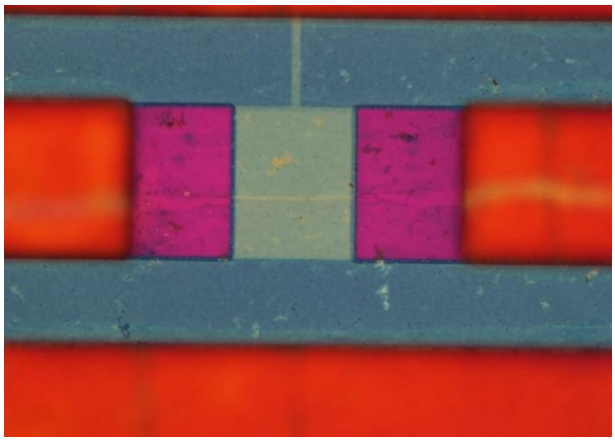


Figure 62 - Optical microscope image of one of the fabricated graphene devices.

4.8 Fabricated devices analysis

The described fabrication process and the layout of the devices allow to obtain them with the determined requirements. The required substrate conductivity of 10 kΩ·cm was obtained by using a 700 µm thick 10 kΩ·cm silicon substrate. The targeted series resistance of the long signal line was 0.8 Ω, having obtained around 0.8 Ω, considering the multimeter resolution. The intended backgate contact resistance had to be around 730 kΩ, and 1.94 MΩ was obtained.

After the fabrication process was completed, the devices were analyzed in the optical microscope. It is possible to observe the graphene in the DUT area in Figure 63.

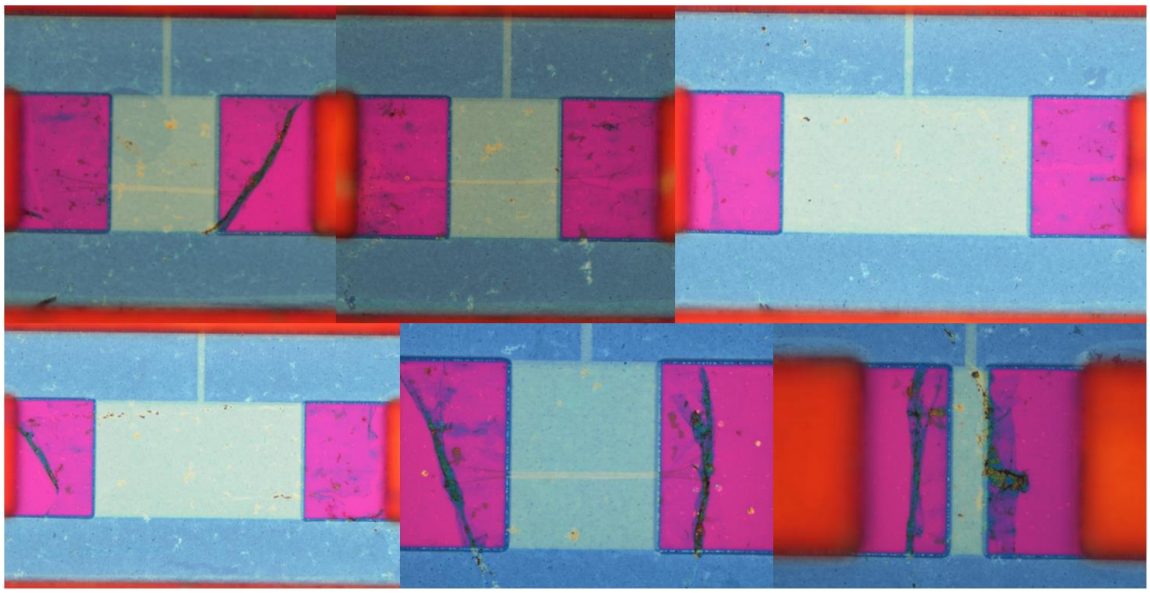


Figure 63 - Optical microscope images of the graphene in the DUT area of the fabricated devices.

As expected, the graphene breaks when transferred to a structure with a large thickness, and in several cases, it also rolls back several micrometers. However, it is also shown that extending the thin gold contacts works and allows the devices to be functional and the electrical measurements can be performed. After performing an optical microscope analysis, a Raman spectroscopy study was carried out as shown in Figure 64.

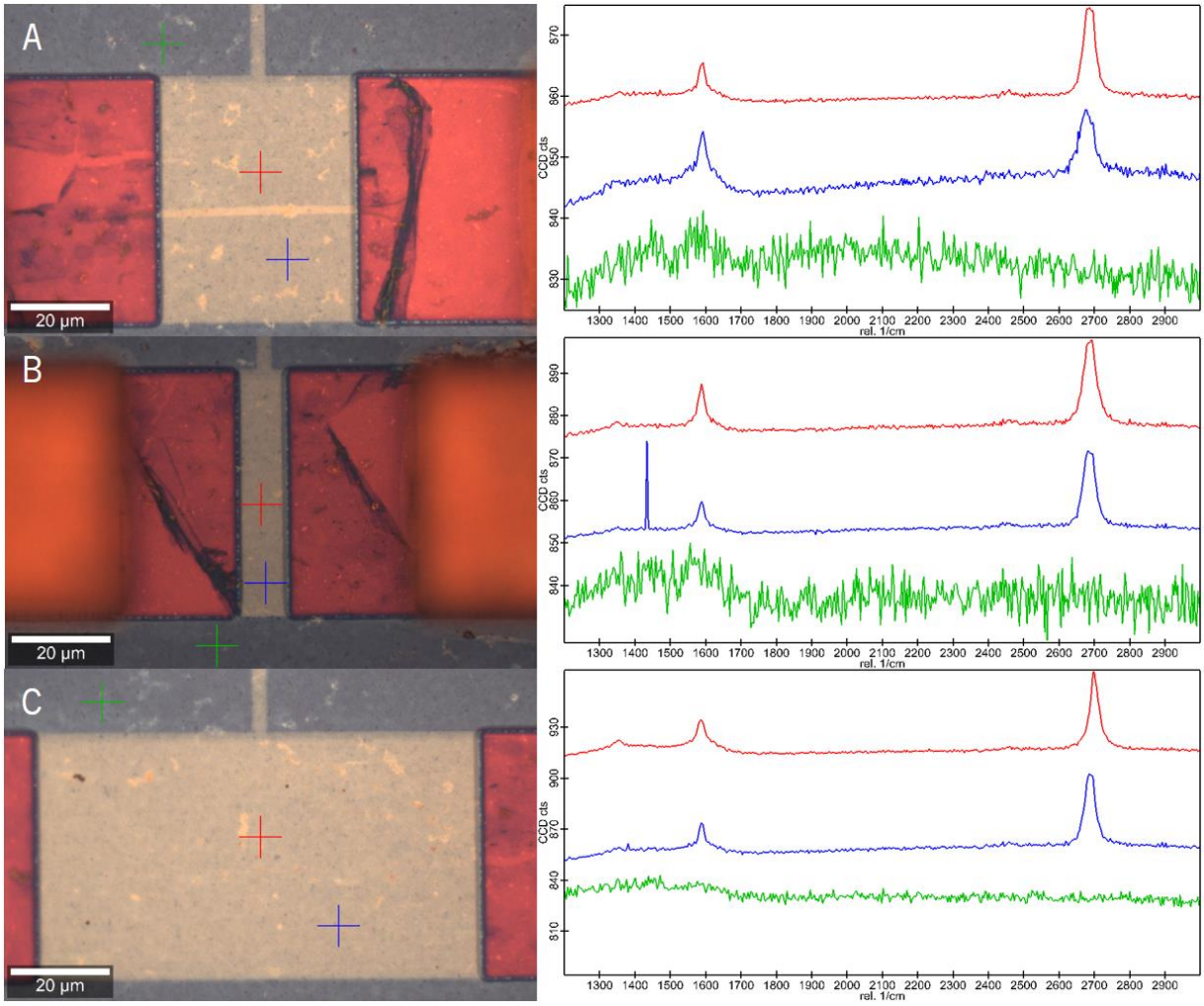


Figure 64 - Optical microscope images obtained with the Raman characterization system, and the respective Raman spectra for each device, where (A) has a device length of 40 µm, (B) has a device length of 10 µm, and (C) has a device length of 90 µm.

Three devices with different lengths were analyzed and the Raman spectra was acquired. This allowed to determine the quality of transferred graphene and further verify whether it was properly patterned. It is possible to observe through the green spectra that in all devices the graphene was not present outside the active (gated) area as intended. Furthermore, it is possible to verify through the Raman spectra as shown in blue and red that for all devices the graphene is monolayer since the 2D band peak is larger than the G band peak. Both optical microscope and Raman analysis confirm that the devices being analyzed are functional, are comprised of monolayer graphene, and can be analyzed electrically.

5 HIGH FREQUENCY CHARACTERIZATION OF GRAPHENE

5.1 Measurement setup

To characterize the graphene through the fabricated graphene devices, it was necessary to implement a measurement setup. A diagram of this setup is shown in Figure 65 as well as a photo of the implemented setup.

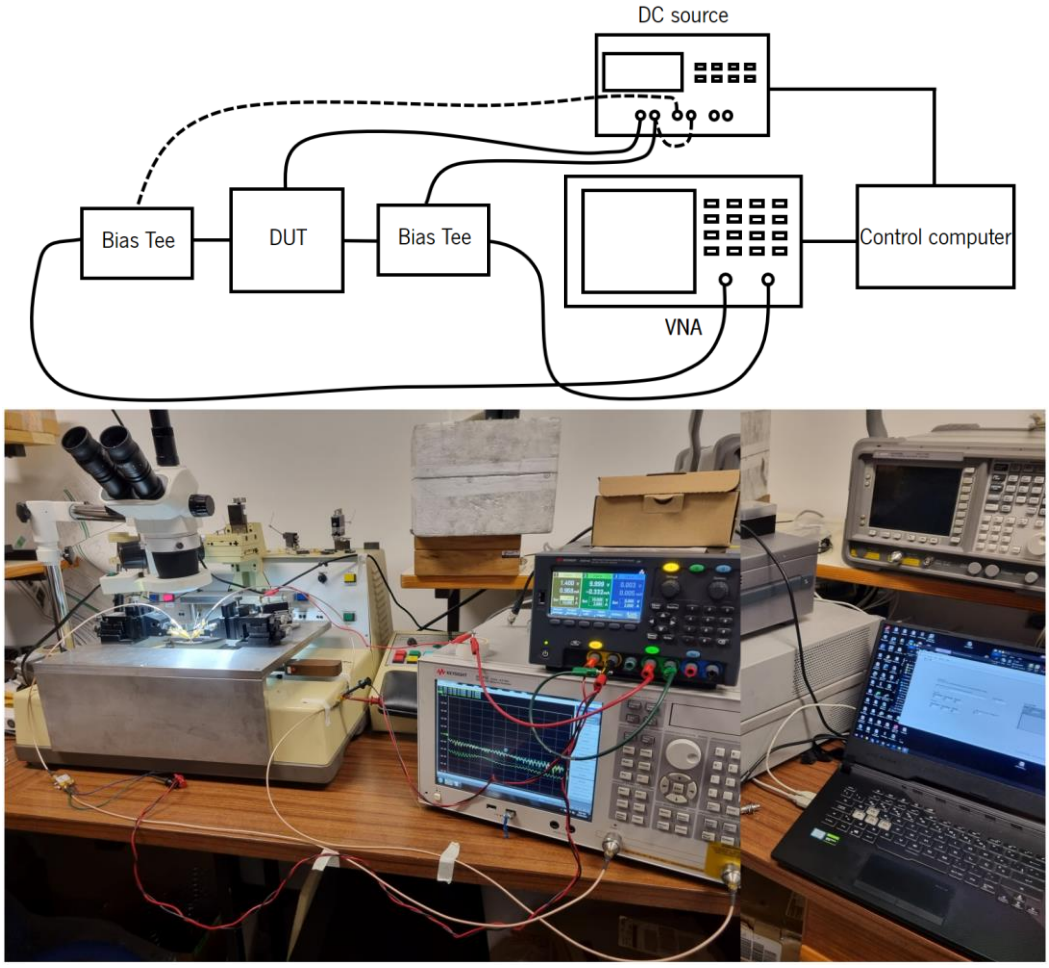


Figure 65 - Diagram of the RF characterization setup (top), and photo of the setup (bottom).

To develop this measurement setup, it must be considered that an RF characterization is intended, and that graphene's properties are different for different chemical potentials. Therefore, to perform the measurements that allow to characterize graphene, a vector network analyzer (VNA) and a DC voltage source are required. The Keysight E5071C VNA (Keysight technologies, Santa Clara, CA, USA) allows the RF characterization to be performed, and the DC source (Keysight E36313A 160W Triple Output Power

Supply) is used to control graphene's chemical potential through voltage gating. The DUT was placed in the probe station, as well as the positioners for the RF probes and DC bias needles. The RF probes used are the GSG |Z|-Probes (FormFactor, Livermore, CA, USA). To reference the DUT to ground, a bias-teeDC bias can be used. In this setup, two ZX85-12G-S+ bias-tees from MiniCircuits were used. Although only one would be necessary, two were used to act as protection for the VNA, preventing damaging this equipment through DC overvoltage in case of dielectric rupture/breakdown. Moreover, this setup also allows for the characterization of graphene FETs by applying a DC voltage to the other bias-tee, as represented in the dashed traces, allowing to apply a drain-source and a gate-source voltage.

To control the VNA and DC source to perform the measurements automatically, a LabView program was developed through NI LabView 2022 Q3. The interface of the program is shown in Figure 66.

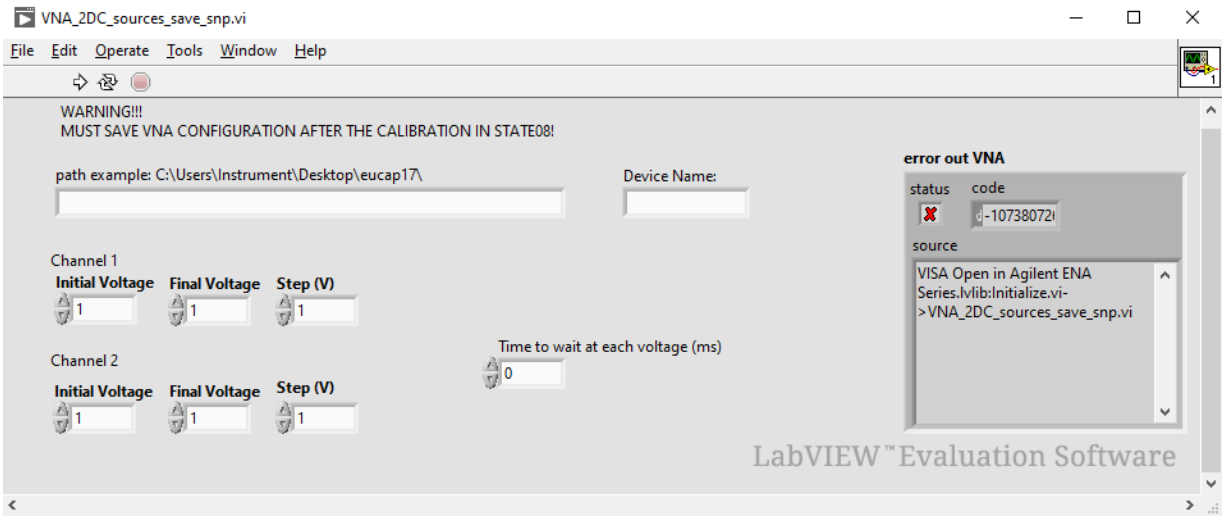


Figure 66 - Developed LabView interface.

The program allows to measure and save the S-parameters of a device for two different DC voltage channels where an initial voltage, final voltage and step size can be defined. These voltage ranges are limited by the equipment used. In this case, the Keysight E36313A was used, which limits the channel 1 to 6 V, and channel 2 to 25 V. A delay as low as 1 ms can be included for the measurement of each voltage step, allowing to apply a voltage during that period of time and perform the measurement afterwards. To perform the measurements, if necessary, the VNA can be calibrated and configured, only requiring to save the state. Finally, to perform the measurements it is necessary to input the device name and directory for the touchstone files to be saved.

5.2 Measurement of graphene's characteristics

The proposed measurement and calibration structures were fabricated, and an example of the device fabricated is shown in Figure 67. It is possible to observe the phenomenon reported in Figure 25, where the graphene breaks due to the large contact height, and the thin gold contacts bridge the contact between graphene and the copper contacts. Furthermore, after breaking, graphene also rolls back in some cases. In this structure, the height of the copper contacts is 5 µm, and the length of the gold contacts is 35 µm. The gated area of graphene has a length of 40 µm and width of 50 µm, where a meander was used to increase the gate resistance. This meander is 3 µm wide and has 24 turns, with a total length of 20,827 µm and a contacting 2191 µm interconnect length, resulting in a total length of 23,018 µm.

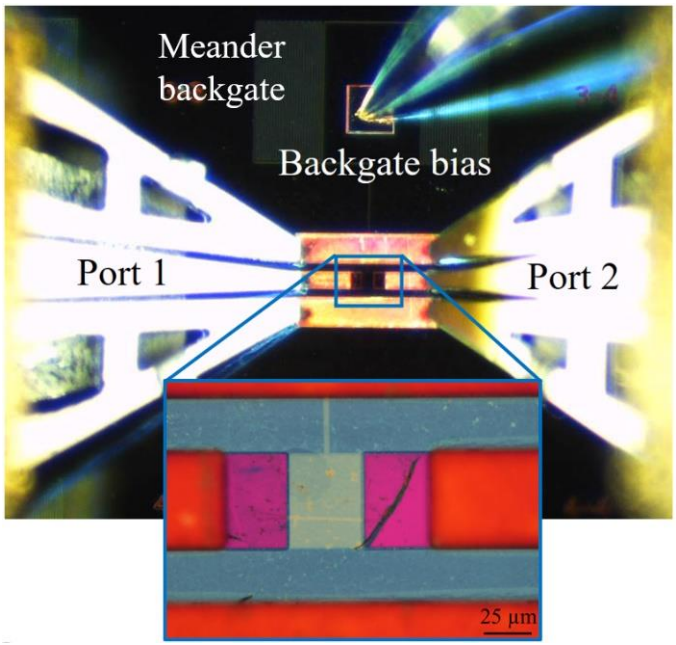
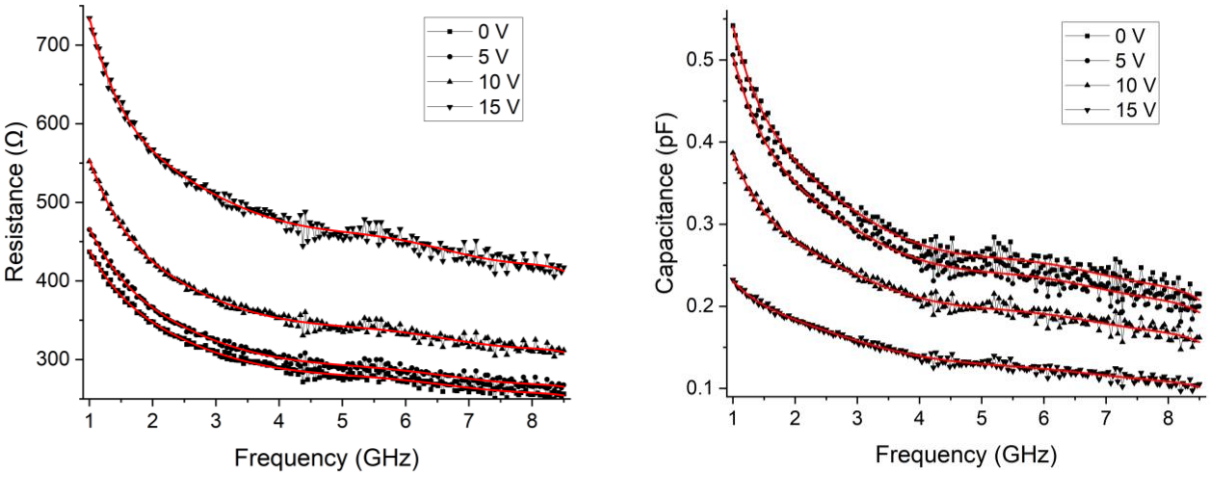


Figure 67 - Fabricated device for graphene characterization.

The fabricated structures were measured with the Keysight E5071C VNA (Keysight technologies, Santa Clara, CA, USA), the GSG |Z|-Probes (FormFactor, Livermore, CA, USA), and the CS-5 calibration substrate (GGB Industries, Naples, FL, USA). Then, the previously proposed calibration procedure was undertaken, allowing us to extract graphene's characteristics. These measurements were performed for 0 V, 5 V, 10 V, and 15 V of backgate bias. The extracted resistance and quantum capacitance of graphene are shown in Figure 68. This data was fitted and plotted in red lines to allow for an easier interpretation.



(a) (b)

Figure 68 – In (a) is shown the extracted resistance and in (b) the quantum capacitance of graphene for backgate bias voltages of 0 V, 5 V, 10 V, and 15 V. Fitted lines are shown in red for an easier interpretation of the results.

The extracted resistance changes from around 450 Ω at 1 GHz down to around 250 Ω at 8.5 GHz for the bias voltage of 0 V. It then increases with the increase of the back gate voltage up to a maximum resistance of around 750 Ω at 1 GHz to around 400 Ω at 8.5 GHz, obtained at 15 V. The quantum capacitance changes from close to 0.55 pF at 1 GHz down to around 0.2 pF at 8.5 GHz for the bias voltage of 0 V. This capacitance reduces with the increase in voltage, achieving a capacitance of around 0.23 pF at 1 GHz down to around 0.1 pF at 8.5 GHz for the bias voltage of 0 V. Such changes are caused by properties of graphene such as carrier mobility. Both resistive and capacitive behavior are as reported in the literature [9], [73], [74] where the graphene resistance and capacitance change according to the applied gate bias, and both reduce with increasing frequency.

5.3 Extracting graphene characteristics

To characterize graphene and to be possible to obtain its impedance characteristics, three devices with different lengths were fabricated, allowing to determine an approximate impedance per square. The width of graphene was 50 µm, while the lengths used were 10 µm, 40 µm, and 90 µm, corresponding to 0.2, 0.8, and 1.8 squares, respectively.

The extraction and modelling of graphene parameters uses the pi model shown in Figure 32. The first parameters to be extracted were the ones that are common to every structure, which are R_s and C_s, (shunt resistance and capacitance). It is possible to observe the extracted values for R_s and C_s in Figure 69.

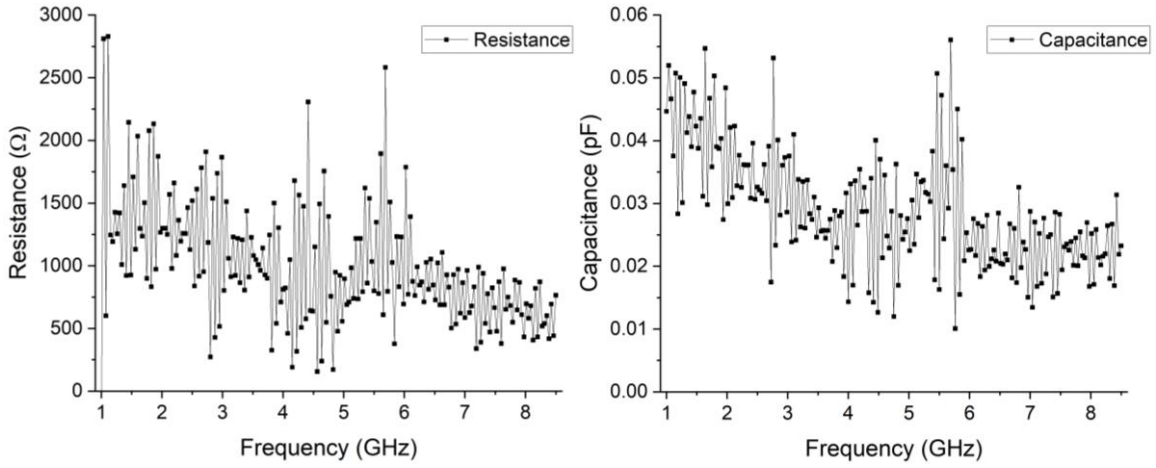


Figure 69 - Extracted substrate resistance and capacitance.

For this step, the equation (23)(24), and (25) were used to obtain the admittance of R_s and C_s, and which were used as the corresponding resistance and capacitance values. To simplify the schematic of the pi-model the resistance and capacitance around 1 GHz was used, meaning that R_s is 1.45 kΩ, and C_s is 0.04 pF. The obtained values have large swings since they were extracted from a single device and may also be affected from small setup movements that affect the calibration. Due to the high resistivity silicon wafer, the resistance value is within the expected range.

To determine the value of C_p, three open structures with different lengths were fabricated. These have the same dimensions and properties as the three device types with graphene, except they don't have graphene. This removes the contribution of graphene and allows to extract the value of C_p through the Y_{21}.

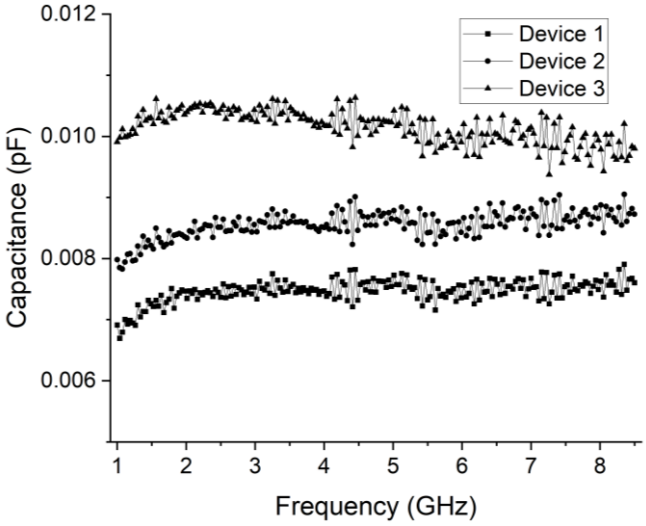


Figure 70 - Extracted paralel capacitance for each device.

Although this capacitance can be extracted, it was not used to extract the characteristics of graphene. Since it is in parallel with it, its admittance was subtracted to every device.

Having determined the values that are common to various devices, the next step is extracting the characteristics of graphene. To perform it, the devices to be used were selected. This selection was performed through checking whether graphene was present (through the resistance and capacitance measured), checking whether there was a resistance and capacitance variation through voltage gating, and checking whether the parameters of the device were far away from an apparent mean (indicating that the device would be functional while indicating that graphene was damaged. Through this selection process, proper working devices were chosen, which also allow to calculate a fabrication process yield. The number of working devices was 22 out of 40 (55%) for the type 1, 8 out of 20 for the type 2 (40%), and 11 out of 20 (55%) for the type 3, meaning that a total yield of 51.25% was obtained. To simulate, model, and extract the characteristics of graphene, a simulator was used where the schematic shown in Figure 32 was implemented using the previously determined components.

To extract, model, and simulate the parameters of graphene, the measurements of the selected devices were used. Then, the contribution of the extracted parallel capacitance (C_p) was subtracted from those measurements. Finally, the average of the Y-parameters for each device and each voltage level was calculated and used as an input parameter of the pi-model, as shown in Figure 71.

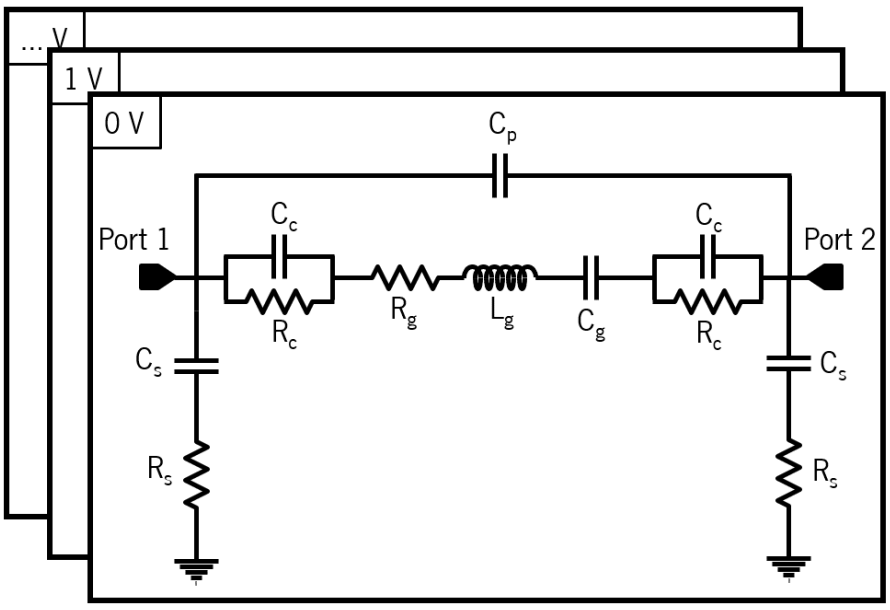


Figure 71 - Example of the implemented schematic for the extraction of graphene parameters.

Although the measurements are comprised of 201 points between 1 and 8.5 GHz, it isn't possible to automatically input every point in the simulator. Therefore, a compromise was needed to input the

values by hand. The values used were for the 3 device types, the real and the imaginary part, and corresponded to 9 frequency points (1 GHz, 2 GHz, 3 GHz, 4 GHz, 5 GHz, 6 GHz, 7 GHz, 8 GHz, and 8.5 GHz). These values were input in two "Goals" in the schematic: one to equal the simulated real part of Y21 with the targeted real part of the Y21, and the other to equal the simulated imaginary part of Y21 with the targeted imaginary part of the Y21. The Y-parameters of the schematic were simulated, and the optimizer was used to approach the simulated Y21 parameters to the measured Y21 parameters throughout the whole frequency range. The optimization type used was "Random", and the number of iterations was 100000, while maintaining all the points with the same optimization weight.

Through this optimization, it was possible to determine the values of R_c, C_c, R_g, C_g, and L_g in relation to the applied gate voltage. In Figure 72 are shown the graphs of the contact capacitance and contact resistance for the three devices, for the different voltage levels. In this analysis, it is not possible to observe the complete V-shaped curve that is a well know characteristic of graphene given that the applied gate voltage was not increased to prevent damage to the measurement equipment from occurring.

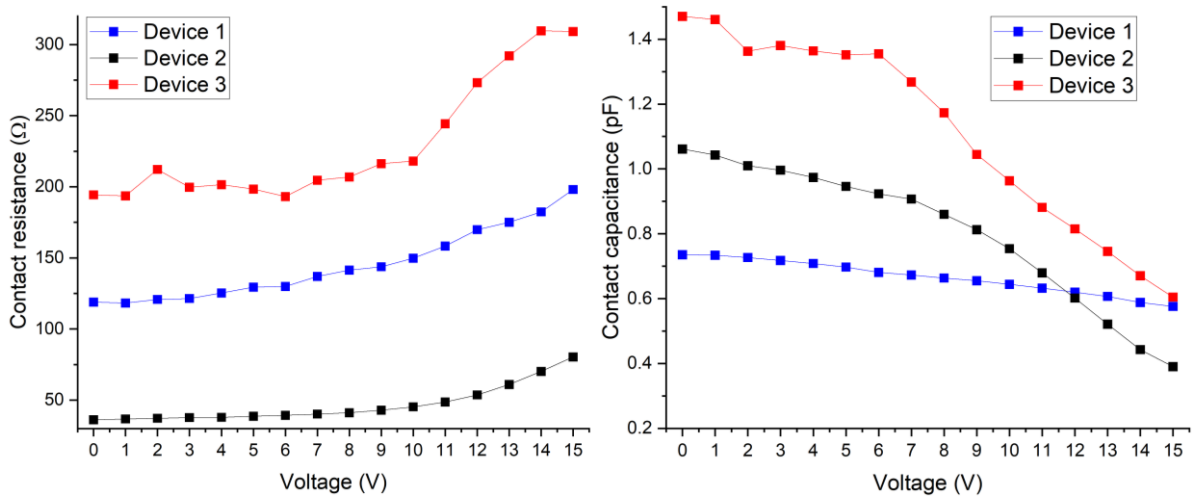


Figure 72 - Extracted contact resistance and contact capacitance of the three graphene devices, for the different voltage levels.

It is possible to observe that the contact resistance for the three devices starts at 119 Ω, 36 Ω, and 194 Ω at 0 V, for the device 1, device 2, and device 3, respectively; and increases up to 198 Ω, 80 Ω, and 309 Ω at 15 V for the device 1, device 2, and device 3, respectively. Through these results, it can also be observed that both contact resistance and capacitance change with the applied gate voltage. The range of these values is within the expected range since the contact of graphene with metals is not perfect [131]. Through the model it is also possible to extract and analyze the values of resistance, capacitance, and inductance of the graphene sheet as shown in Figure 73.

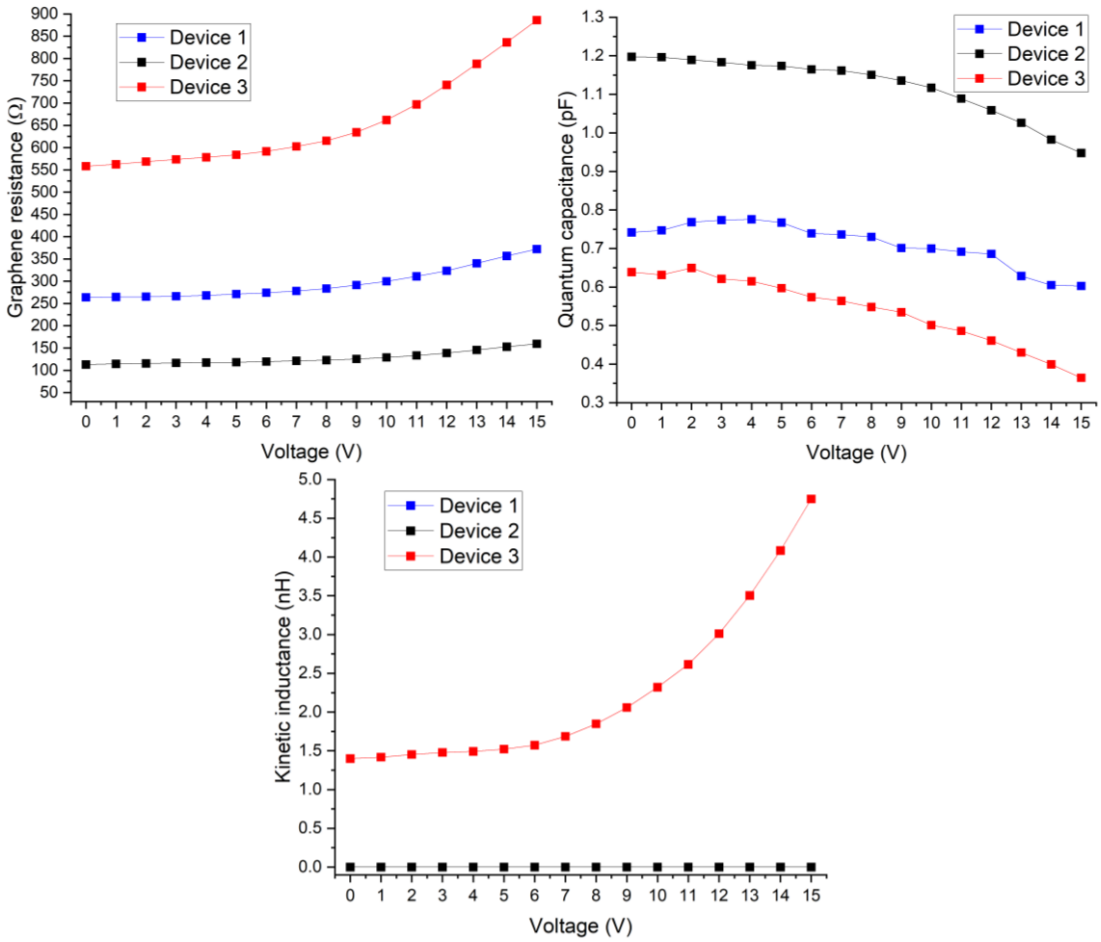


Figure 73 - Extracted graphene resistance, quantum capacitance, and kinetic inductance of the three graphene devices for the different voltage levels.

It is possible to observe that the resistance of the sheet of graphene is 264 Ω, 113 Ω, and 558 Ω at 0 V for the device 1, device 2, and device 3, respectively; and it increases up to 372 Ω, 160 Ω, and 886 Ω at 15 V for the device 1, device 2, and device 3, respectively. This behavior is expected for graphene, since its resistance increases as the applied gate voltage increases, approaching the Dirac point.

The extracted capacitance of the graphene sheet is 0.74 pF, 1.2 pF, and 0,64 pF at 0 V for the device 1, device 2, and device 3, respectively; and it reduces to 0.60 pF, 0.94 pF, and 0,36 pF at 15 V for the device 1, device 2, and device 3, respectively. This variation in the capacitance is due to the quantum capacitance of graphene, since it reduces as the applied gate voltage increases, approaching the Dirac point.

From the kinetic inductance graph, it is possible to conclude that extracting the kinetic inductance was only possible in the device 3. This is likely due to the small length of the device 1 and device 2, resulting in an extremely low – near zero – inductance, being the reason why the blue and black lines are

overlapped. The device 3, however, shows that graphene has an inductance of 1.4 nH at 0 V, which increases up to 4.75 nH at 15 V as expected, since the kinetic inductance of graphene increases with the voltage as it approaches the Dirac point.

Through the extracted values shown in Figure 72 and Figure 73, it is possible to plot the result of the modelling through using the determined component parameters into the pi-model, and comparing the obtained Y21 parameters with the measurements. The comparison between the measured data and the modelled parameters can be observed in Figure 74, where the measured data is plotted through scattered points, and the model is plotted in a line. This figure shows the measured and modelled data for the three device types. For an easier analysis and representation, the real and the imaginary part of the Y21 were plotted in two graphs.

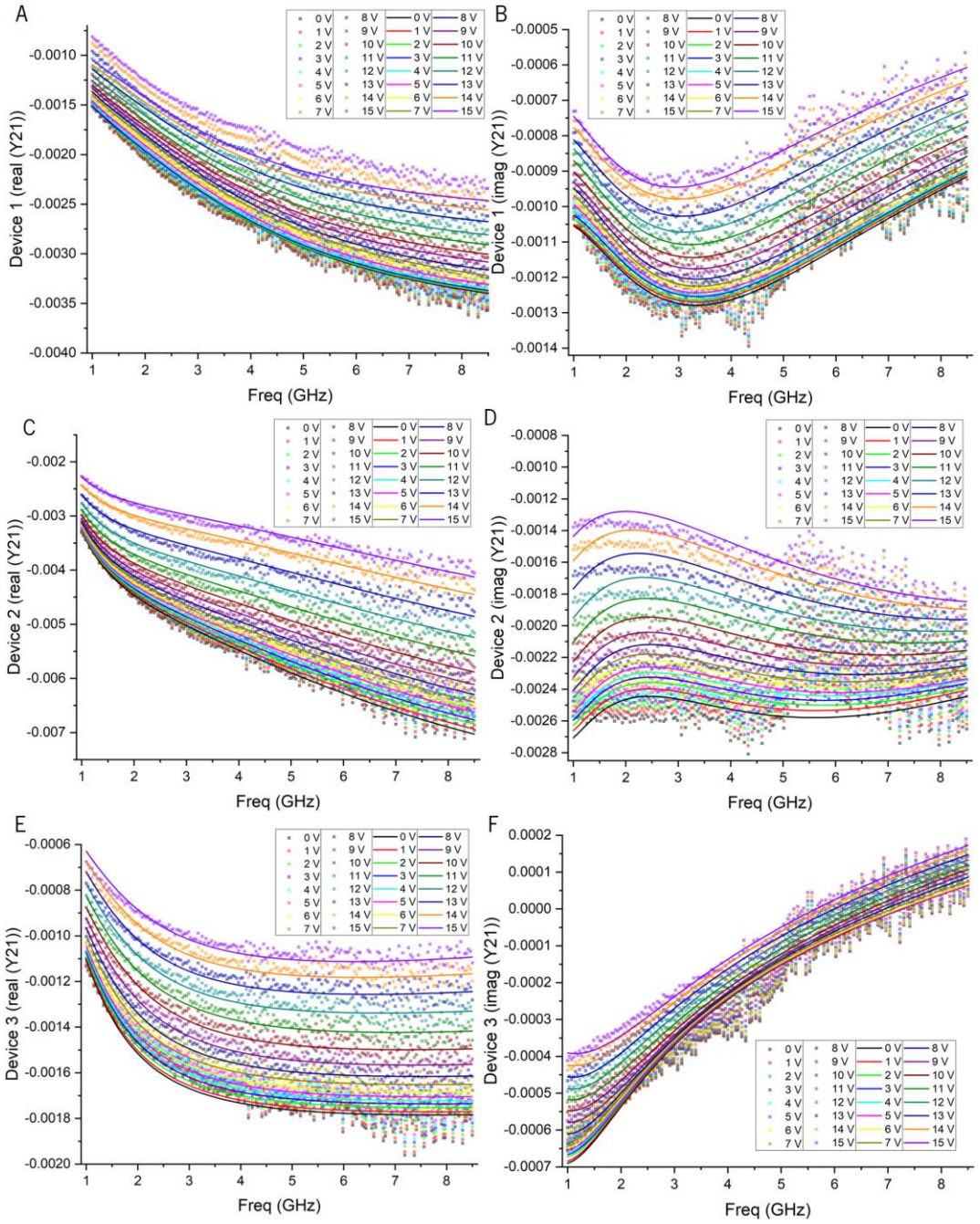


Figure 74 – Measured (dots) and modelled (continuous line, through the model in Figure 71) graphene Y21 real and imaginary parameters, in A is shown the real part of Y21 of the device 1, in B is shown the imaginary part of Y21 of the device 1, in C is shown the real part of Y21 of the device 2, in D is shown the imaginary part of Y21 of the device 2, in E is shown the real part of Y21 of the device 3, and in F is shown the imaginary part of Y21 of the device 3.

Through these graphs, it is possible to observe that both the pi-model used and the components' values of the pi-model allow to accurately represent the measured graphene devices. Although the modelled components are the ones that originate the lowest error through the optimizer, it is possible to observe that the model is not perfect. Although the Y parameters were used to perform this optimization,

it is possible to transform the obtained values into units that can be more easily interpreted. Therefore, the Y21 values were converted in the corresponding resistance and capacitance and are shown in Figure 75, being another form of showing the results shown in Figure 74.

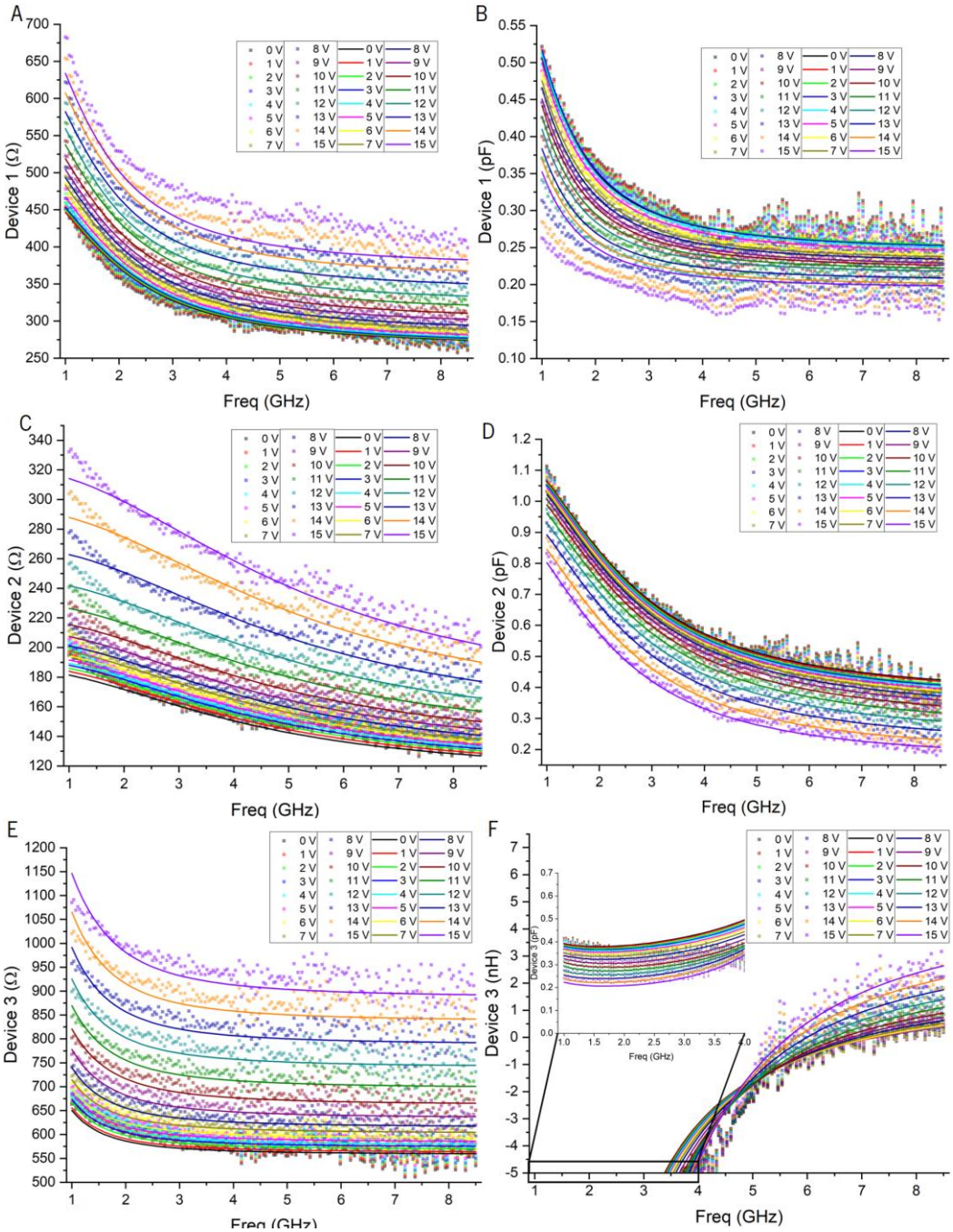


Figure 75 - Measured (dots) and modelled (continuous line, through the model in Figure 71) graphene resistance and capacitance (and inductance), extracted from the real and imaginary parts of Y21. In A is shown the equivalent resistance of the device 1, in B is shown the equivalent capacitance of the device 1, in C is shown the equivalent resistance of the device 2, in D is shown the equivalent capacitance of the device 2, in E is shown the equivalent resistance of the device 3, and in E is shown the equivalent inductance of the device 3 (with an inset showing the equivalent capacitance at lower frequencies).

This form of representing the measured and modelled parameters allows to more easily interpret the results. As expected, the resistance increases and the capacitance decreases as the gate voltage approaches the Dirac point [9], [73], [74]. It is also possible to observe that for high frequencies, the device 3 has an inductive behavior, which is indicative of graphene's kinetic inductance. It is also possible to conclude that graphene was modelled successfully, having represented the measured resistance, capacitance and inductance successfully. Moreover, the behavior of graphene was also accurately represented from 1 to 8.5 GHz.

Having obtained the lumped elements that represent a sheet of graphene, it is possible to also use them and analyze how increasing the length of the graphene sheet changes its resistance, capacitance, and inductance. In Figure 76 it is possible to observe the effect of increasing the length of the graphene sheet. The data is shown in relation to the number of graphene squares and since these values were extracted for the previously reported devices, it corresponds to a width of 50 µm. To fit this data, a regression was performed.

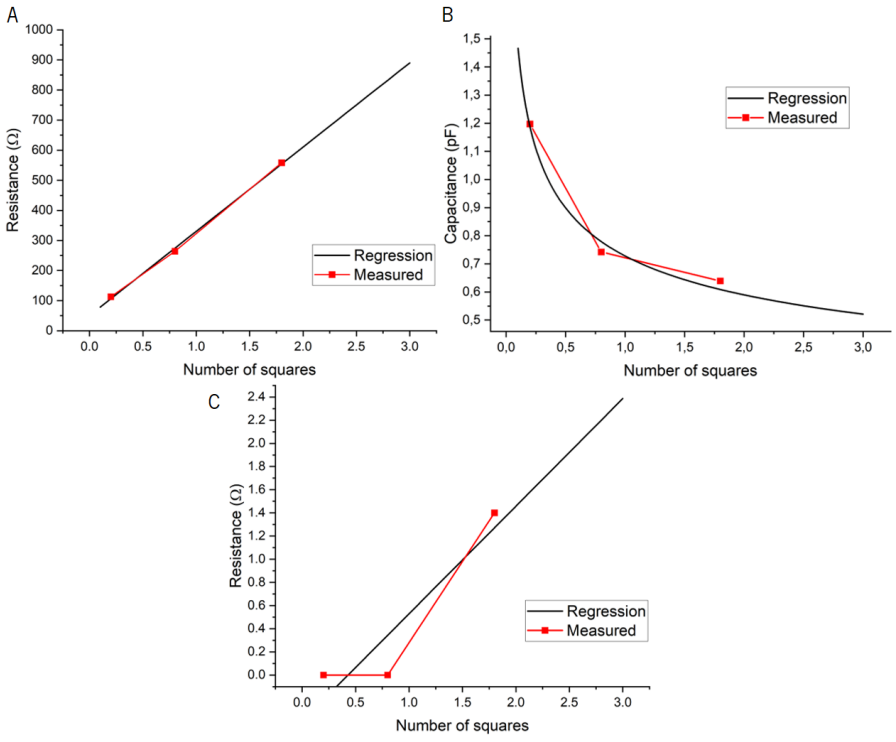


Figure 76 - Extracted resistance (A), capacitance (B), and inductance (C) of graphene at 0 V, per number of squares with a regression of the data.

The equations used, as well as the obtained constants to fit the curves to the extracted data are shown in Table 5.

Table 5 – Equations and calculated constants to fit the graphene elements values for 0 V and 15 V

		Resistance (Ω)	Capacitance (pF)	Inductance (nH)
	Equation	$y = ax + b$	$y = ax^b$	$y = ax + b$
0 V	a	279.9443	0,72812	9.2859e-10
	b	50.4673	-0,30417	-3.9997e-10
15 V	a	460.3144	0,50975	3.1496e-09
	b	43.0913	-0,39186	-1.3566e-09

This analysis allows to determine how graphene's characteristics change with increasing length. Graphene's resistance appears to increase in a direct proportion with the increase in length at a rate of approximately 279 Ω/square. The quantum capacitance of graphene, however, appears to have an inverse proportion with the length of graphene. This suggests that increasing the length of graphene is similar to adding a capacitance in series. The curve fitted to the inductance value suggests that the inductance increases at a rate of 0.93 nH/square. However, since the length of the two shorter devices is extremely small, and the measurement frequency is limited, none of these devices had an appreciable inductance that could be extracted in the modelling process, meaning that with the available data, it is difficult to obtain an accurate evolution of the inductance.

The reported values offer an insight on how graphene can be modeled through lumped elements, and according to its dimensions. This data and model, however, is currently only valid for graphene with a width of 50 µm, increasing length, and for a frequency range between 1 to 8.5 GHz. Since lumped elements are used, it should be possible to use these values outside this frequency range although the accuracy can't currently be guaranteed. Finally, these values are valid for graphene devices that are contacted by gold, and a Si substrate with an SiO_2 dielectric. It should be possible to transpose these values to other gate characteristics. Changing the thicknesses, for example, should be directly calculated through determining the corresponding graphene chemical potential. Modifying the material and thus, the dielectric constant doesn't guarantee that it is also a direct correspondence with the chemical potential and further testing is necessary.

6 GRAPHENE WIRELESS SENSOR READOUT

In recent years, biomedical engineering has experienced remarkable advancements which were fueled by the integration of emerging materials and wireless technologies. One of those materials is graphene, where in the area of biosensing, for example, using functionalized graphene has allowed to develop ultrasensitive biosensors [132], [133], [134]. These advancements can revolutionize the field through highly sensitive, real-time detection of biological analytes.

An application of functionalized graphene can be its implementation within antennas. Antennas are necessary for wireless communication, information exchange, and even wireless power transfer. Through the integration of functionalized graphene as the biosensing element in antennas, it should be possible to obtain a wireless biosensor. When functionalized graphene is exposed to a target analyte, that interaction leads to changes in its electrical properties. These changes, in turn, modulate the signal transmitted by the antenna, allowing for the detection and quantification of the target analyte. Through this technique, it should also be possible to combine the benefits of both and obtain a wireless backscatter biosensor. The development of such a system should allow to enable wireless, remote and non-invasive biosensing with high sensitivity and accuracy.

In this section, the development of a graphene backscatter antenna will be discussed. The design and fabrication of the device will be discussed as well as the underlying principles and shedding light on the future prospects of this such device.

6.1 Wireless readout working principle

As discussed, graphene is a material with tunable electrical properties that can be controlled by adjusting its chemical potential, allowing its impedance to be tuned as previously demonstrated and characterized. The interaction of graphene with the target analytes present in the surrounding environment changes its chemical potential, changing its impedance. This means that changing the chemical potential of graphene provides valuable information about the interaction between the analyte and the graphene surface. By monitoring the impedance change of the graphene biosensor, it is possible to detect and quantify analytes.

The tuning of graphene's chemical potential can be achieved through several methods. In this case, the most relevant ones are the target analytes coupling with graphene, and the voltage gating.

Therefore, the change in impedance of graphene biosensors can be effectively modeled or translated by a corresponding change in the gate voltage applied to the graphene layer. These changes in impedance can later be correlated so that a relationship between impedance and gate voltage through experimental calibration can be established, allowing to interpret the electrical responses of biosensors. This modeling approach is also a valuable method to understand and optimize the performance of graphene-based biosensing devices.

Using RF for wireless power transfer with the objective of powering a biomedical device or sensor and receiving a readout has been the focus of various research works [135], [136], [137], [138]. An example is shown in [136], where a solution of wireless power with tracking is presented. It should be possible to implement a biosensor readout through modulating the feedback signal.

In this work, the proposal is to implement an antenna (such as a dipole) with a load that is graphene. To mimic the graphene biosensing capability, it will be tuned through voltage gating. Since gating graphene changes its impedance, it should be possible to modify and control the reflected power. Therefore, since graphene is directly connected to the antenna, the amount of reflected power should change according to graphene's impedance.

To measure this variation in reflected power, the VNA will be calibrated with the 85033E SOLT calibration from Keysight. This calibration is performed in one port, using the provided standard short and open standards. To more easily measure the variation in the reflection of the DUT, the load standard was replaced by the antenna. The objective of this modification is to set the reference (the zero reflection) to the background environment, instead of the 50 Ω load. In this way, any change in the graphene load placed at the antenna port will be easily detected. Through this, it is expected to observe the change in the DUT's impedance through the measurement antenna's S11.

To have a resistance closer to 50 Ω, the extracted parameters can be used to calculate the required dimensions of graphene. According to the extracted resistance in Figure 76 A, and the corresponding equation values in Table 5, it is possible to conclude that a length of around 0 μm is necessary. Furthermore, when taking the values of contact resistance as shown in Figure 72, it is possible to conclude that a device with those characteristics is nearly impossible. Therefore, a device as small as possible was designed. In parallel with this work, another work on graphene transistors was being developed, with a fabrication process that allowed to fabricate devices with a very small length, thus reducing its resistance. The graphene in these devices had a length of approximately 800 nm, and a width of 35 μm. These dimensions were used in the fabrication of this device, since the fabrication

process allows to fabricate it with a high degree of repeatability, and has dimensions that make the resistance closer to 50 Ω.

6.2 Antenna design

To obtain a working prototype, a dipole antenna was used. Its operation frequency was chosen so that it could be measured by the laboratory equipment. Furthermore, its harmonic was also of interest so that it could be possible to perform other experiments and explore the multiplying and mixing capabilities of graphene. To prevent the antenna from becoming too large, the chosen operation frequency was 3 GHz, allowing it and its second harmonic to be measured by the laboratory equipment. To control the resistance of graphene through gating, at least 2 DC contacts are necessary: a reference, and a gate. A third contact was also added, allowing the graphene to be used for other experiments, if necessary. The antenna is shown in Figure 77, as well as its dimensions.

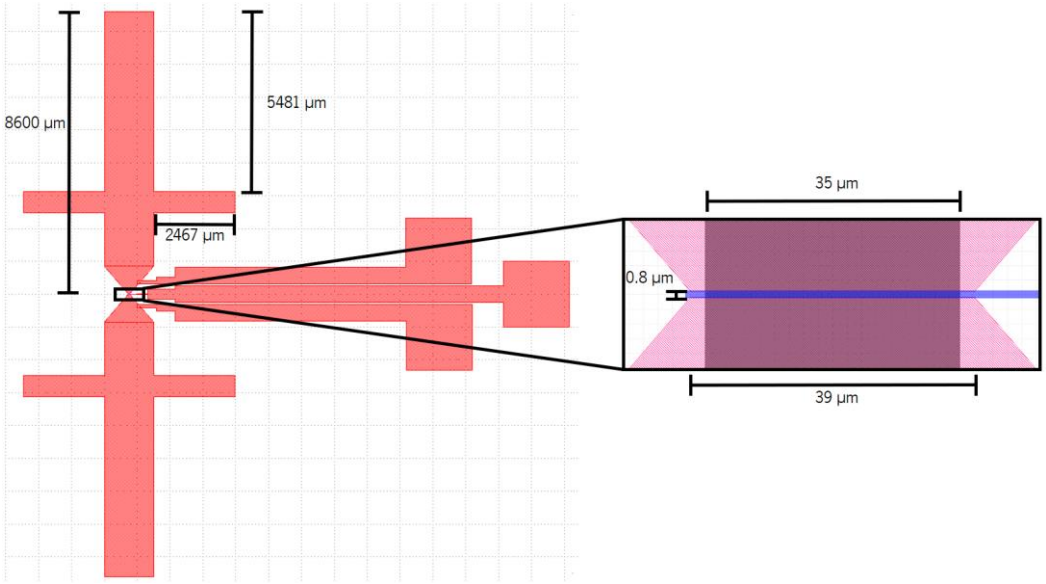


Figure 77 - Dipole antenna designed with graphene to obtain a backscatter readout; the inset shows the area with the graphene, as well as its gate and dimensions.

It is possible to observe the three DC contacts on the right of the antenna, which will allow to control the characteristics of the graphene. The inset zooms on the small gap between the dipole arms and shows the dimensions of the area with gated graphene. The dipole was initially simulated and designed to operate at 3 GHz. To allow it to operate at 6 GHz, two stub-like structures were added on each dipole arm. This dipole was simulated, allowing to determine its operation frequency. The results of the simulations are shown in Figure 78.

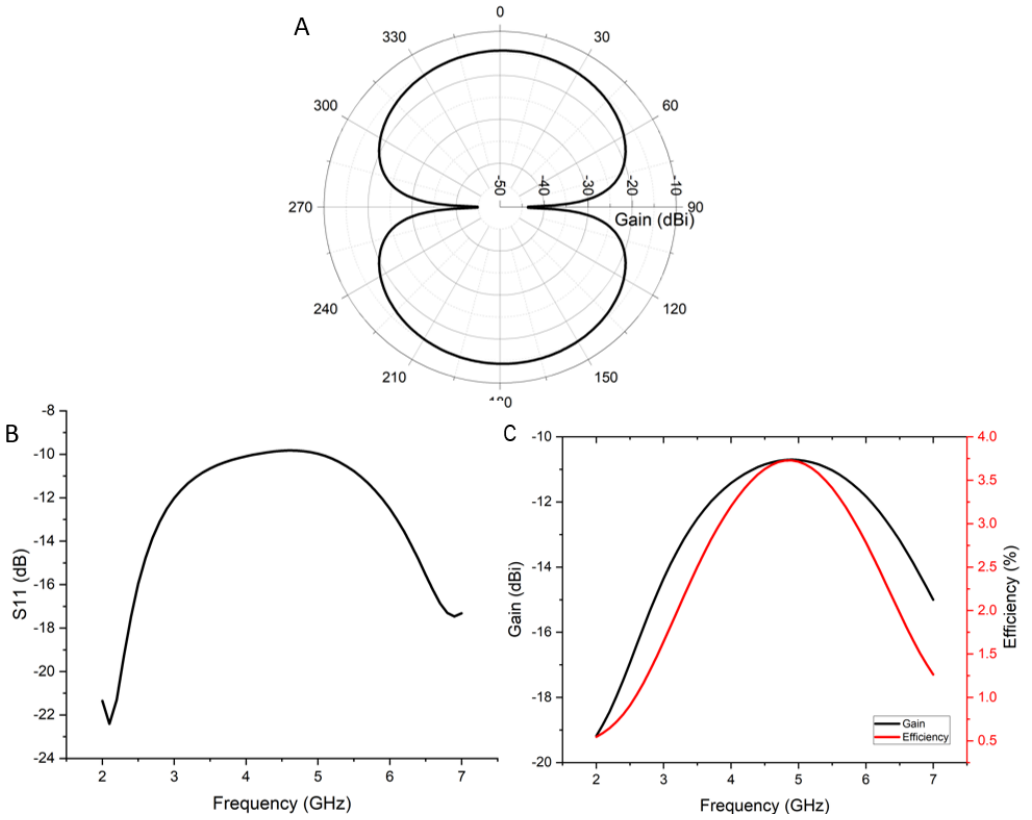


Figure 78 - Results of the simulated antenna showing in (A) the 2D representation of the radiation diagram, in (B) the S11 of the antenna, and in (C) the gain and efficiency of the antenna.

In Figure 78 A is shown the cross-section of the E-plane radiation diagram at 3 GHz A, where a maximum gain of -14.35 dBi (-11.827 dBi at 6 GHz) can be observed, while its directivity is approximately 3.5 dBi across the simulation frequency range. In Figure 78 B the S11 of the antenna is plotted, where it is -12.026 dB at 3 GHz and -12.510 dB at 6 GHz. In Figure 78 C the gain and efficiency of the antenna between 2 GHz and 7 GHz is shown, where it is possible to observe that at 4.9 GHz, the maximum gain and efficiency of this antenna is obtained, being -10.7 dBi and 3.73%, respectively. The antenna's characteristics demonstrate that a better performance can be attained, however, it should be possible for it to be used with the best efficiency at 4.9 GHz, while being able to operate at the desired 3 GHz and 6 GHz frequencies in case it is desired to implement a frequency mixer or doubler.

6.3 Wireless readout of graphene sensor

The previous device was fabricated using a similar fabrication process and using the dimensions shown above. The resulting difference of the devices is that the oxide was changed from 50 nm of SiO_2

to 10 nm of Al_2O_3. The gate metal as well as the top layer metal was modified to 50 nm of Au with copper serving as adhesion layer.

The measurement of the backscatter was performed as previously described. The standard SOLT calibration was used, and the load was replaced by the antenna in its location. The antenna used was the Pasternack PE9887-11 horn antenna which has an operating frequency from 4.9 GHz to 7 GHz. The fabricated sample was placed on a wooden table, the horn antenna was placed on top of it, and the DC pads were contacted with needles. This setup is shown in Figure 79 as well as the respective diagram.

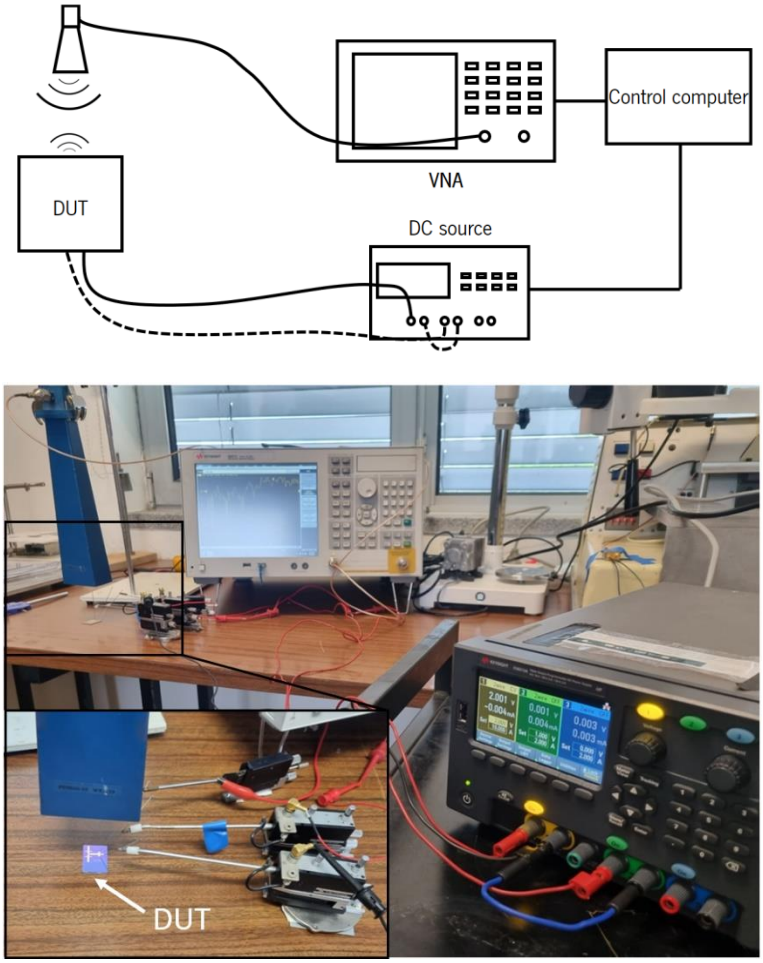


Figure 79 – Diagram of the measurement setup on top, and setup used for the measurement of the backscatter of the antenna with graphene on the bottom.

Then, the measurement was performed by changing the gate voltage and measuring the S_{11} through the VNA. The applied voltage ranged from 0 V to 4 V, and the measurement was performed in 1 V steps. The measured values are shown in Figure 80.

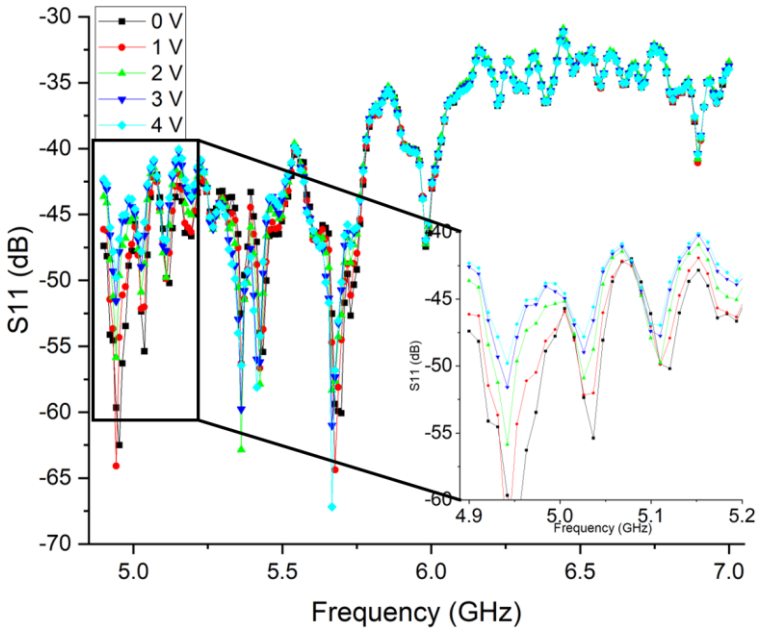


Figure 80 – Measured S_{11} in dB of the backscatter by changing the graphene voltage from 0 to 4 volts in the working range of the measurement antenna.

From these results it can be observed that it is possible to control the backscatter of the device by applying a gating voltage to graphene. In Figure 81 this variation is shown using the 0 V as a reference. One of the graphs shows the raw data while the other shows the same results but the data was smoothed for easier visualization and interpretation.

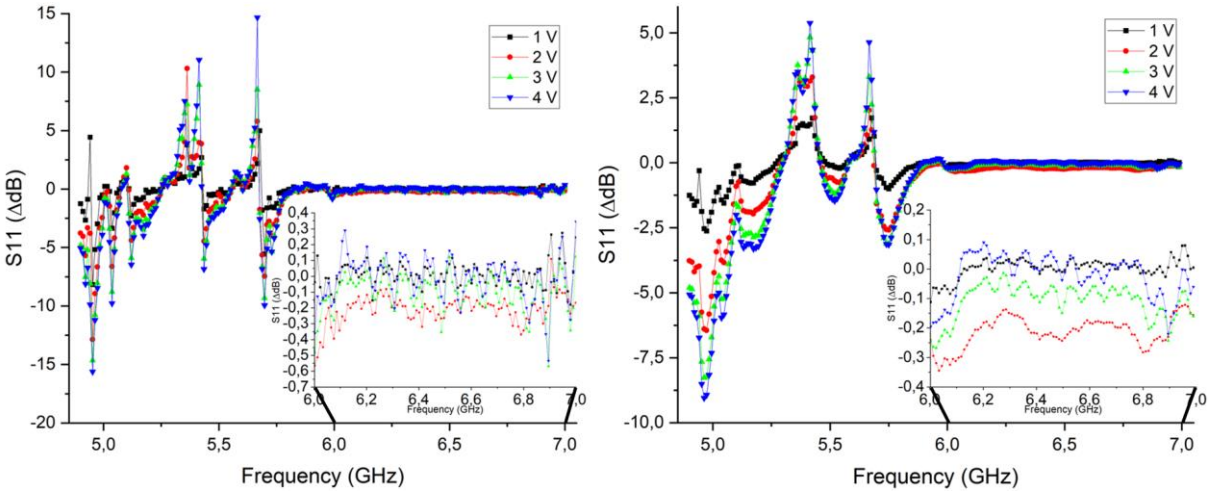


Figure 81 - Variation of the S11 for different gate voltages. The graph on the left shows the results for raw data while the graph on the right shows the smoothed (Excel exponential smoothing with a damping factor of 0.8) results for easier visualization.

It is possible to observe that, as expected, the measured S11 changes when different voltages are applied. This voltage variation changes the impedance of graphene which in turn changes the amount

of power that is backscattered and measured through the S11. For frequencies below 5.8 GHz it is possible to observe a very large change in the measured S11 between the 0 V and the remaining scenarios when voltage is applied. As expected, with the increasing voltage, the S11 increased which indicates that the impedance of graphene is increasing, as expected. For frequencies above 5.8 GHz it is possible to observe that the S11 variation is very small, making it harder to interpret the results. The 2 V measurement presents a larger deviation than the remaining scenarios, which is unexpected. This can be due to various causes such as: extremely small measured variations which are more prone to noise, the measurement setup which is prone to external interferences such as from other measurement devices, and to the measurement being performed in the near-field of the measurement antenna.

Through carefully choosing frequencies to plot the S11 over a voltage range allows to provide another form of plotting these results. These results can be observed in Figure 82.

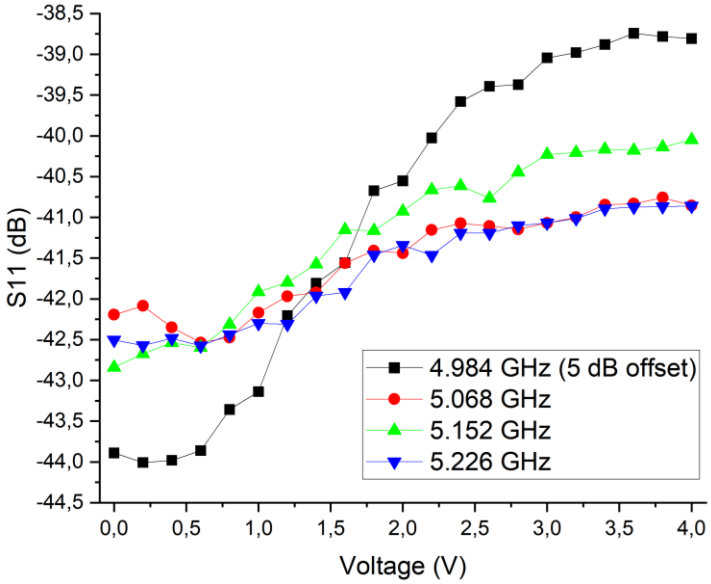


Figure 82 - Measured S11 in dB of the backscatter by changing the graphene voltage from 0 to 4 volts at 4.984 GHz, 5.068 GHz, 5.152 GHz, and 6.226 GHz.

The frequency points where there was not a very large or small change in S11 were plotted with the aim of avoiding resonant points or points were no difference could be measured. Through this analysis, it is possible to observe that the change in S11 through the applied voltage in those frequency points resembles the characteristic V shape of graphene. Thus, this change is due to the change in graphene's impedance.

In order to verify the validity of the models previously developed ín this work for graphene, a model was implemented for the full system. The block diagram of the simulated circuit shown in Figure 83 was simulated. This circuit consisted of a 50 Ω port, a coaxial cable, a balun, the simulated model of

the antenna, and the modelled graphene impedance which was obtained from the extracted characteristics. The coaxial cable was added as an attempt to emulate any losses and resonant effects originating from the propagation of the measurement signals over the air.

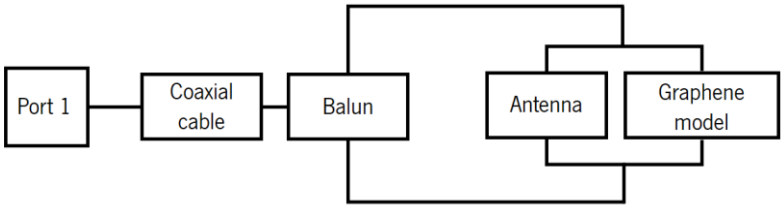


Figure 83 - Block diagram of the simulated circuit to attempt to model the measured values.

To model the measurements, the length and conductivity of the coaxial cable were adjusted. This was done in an attempt to model the measurement conditions and obtain results similar to Figure 80 and Figure 81. To achieve this, the properties of the coaxial cable were adjusted. Its length was changed to around 70.5 cm so that the resulting peaks had a spacing of around 150 MHz, as shown in the inset of Figure 80. Then, the relative resistivity of the cable was tuned to 250 with the objective of achieving an S11 that has a range similar to the results shown in Figure 80 and a behavior that is similar to the results shown in Figure 81. The parameters of the antenna were the results from layout simulation. The parameters of the graphene used were based on the graphene's dimensions and calculated through the values shown in Table 5. To model the measurements at 0 V, the extracted characteristics at 0 V were used. To model the measurements at 4 V, the extracted values for 15 V were used since those are the extracted values that are closer to the chemical potential of the device at 4 V. This difference results from the different oxides used in the characterization of graphene and fabrication of the backscatter antenna. The results from these simulations are shown in Figure 84.

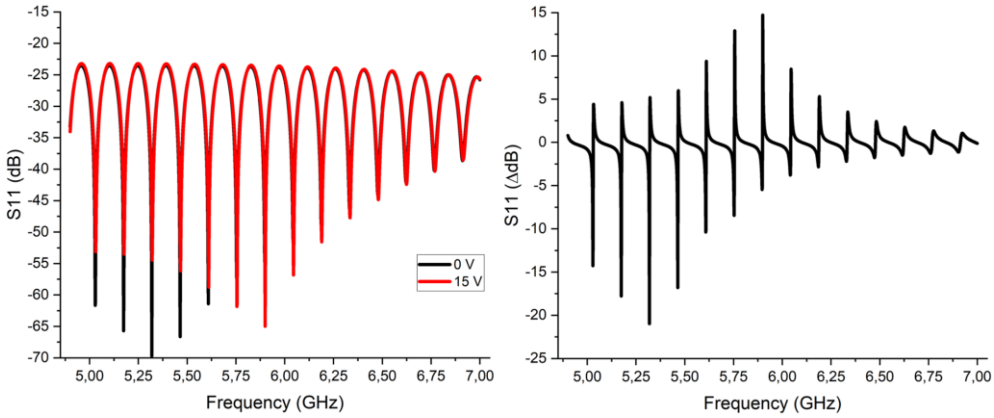


Figure 84 - Results from the simulation of the circuit with the antenna and graphene to measure the backscatter: on the left are the results of S11 for a gate voltage of 0 V and 15 V, and on the right is the resulting difference from both cases.

It is possible to use these results to compare the modelling with the obtained measurements, however, it is mostly possible to perform only a qualitative analysis. This is due to the imperfect measurement setup and conditions (that are only obtained in simulations) that couldn't be obtained due to the nature of the implemented over the air characterization setup. Furthermore, it is also worth noting that the measurements of, for example, the case of 0 V and 4 V aren't performed exactly at the same time, making it possible to have slight physical changes in the setup (for example through slight vibrations, moving cables, or measurement needles). However, replication of the measurement results was attempted.

It is possible to observe through the results that the peaks with spacing of 150 MHz were successfully obtained through adjusting the length of the coaxial cable. Furthermore, an approximation of the range of S11 which was measured to be around -70 dB to -30 dB was modelled to be from around -70 dB to -25 dB.

Then, the variation of S11 in the measurements has values that changed from -15 dB to around 15 dB, which in the simulations was obtained from around -21 dB to 15 dB. Furthermore, it is possible to observe that there is a tendency for the largest peaks to be negative below 5.3 GHz in the measurements and below 5.5 GHz in the simulations. There is also a tendency for the largest peaks to be positive above 5.3 GHz in the measurements, and above 5.5 GHz in the simulations. Throughout the whole frequency range, in both measurement and simulations, there are also lower peaks and peaks that have the opposing sign. In the measurements above approximately 5.8 GHz there was a large reduction on the amplitude of these peaks. In the simulations there is also a large reduction in the peak's amplitude above 6.2 GHz, although the decline in amplitude is larger in the measurements.

Through the measured and simulated results, it is possible to conclude that the modelling of the device, including the measurement setup, the antenna, and the graphene and its tunable characteristics could be achieved. Therefore, it is also possible to conclude that the extraction and modelling of graphene parameters presented in this work was successfully performed and could be used to model an RF device integrating graphene.

7 CONCLUSIONS

Graphene has been widely presented as a wonder material that has extraordinary properties, a wide range of applications and the potential to revolutionize various industries. One possible application of graphene is electronic circuits, more specifically for RF applications. This application of graphene still requires further research to consolidate graphene's potential. Therefore, the work presented in this document aimed to further increase the knowledge on graphene and contribute to the state of the art.

Although using graphene to develop graphene passive elements for RF applications is not recent, it is still a growing area. Therefore, the literature was analyzed to determine where graphene had been used to develop RF components and establish the current state of the art on graphene devices and modelling of graphene devices. This allowed to conclude that graphene can be a promising material for the development of RF devices, with various devices having a promising performance. The current state of modelling, however, is still not well defined yet, resorting mostly to the Kubo formalism.

In this work, it was aimed to further increase the knowledge on the RF characteristics of graphene, provide a detailed insight on its characteristics, and provide data and tools that can aid and reduce the complexity on the development of graphene devices. Therefore, the TRL calibration was used to characterize graphene. Due to the exotic properties of graphene, however, it was necessary to perform simulation work on this calibration. These simulations were used to establish the requirements for the fabrication of the calibration structures and the devices, since graphene requires thin metal contact height and a back gate to characterize it for different chemical potentials.

Graphene device fabrication must take the properties of graphene into account. The fabrication process started with the growth of graphene which evolved into tailoring the recipe to grow of large graphene crystal flakes. Ultimately, typical monolayer graphene was used since the graphene flakes reduce the device yield, and using the graphene flakes was not possible due to growth conditions. This resulted in a fabrication yield of around 40% up to 55%. Then, the graphene transfer and contact resistance reduction were discussed, concluding with using gold contacts and transferring with PMMA. Finally, the characterization of graphene and quality evaluation was done through Raman spectroscopy. This allowed to conclude that the graphene used is monolayer since the 2D band peak is larger than the G band peak. The previously performed simulations on the structure of the devices was used to develop the fabrication process while taking into account the available cleanroom equipment and graphene's constraints.

Through the devices it was possible to perform the high frequency characterization of graphene. This was performed through a VNA and a voltage source to characterize the graphene for different chemical potentials. Then, through the extracted values and using a pi model, it was possible to isolate and extract the different components from graphene. The values were extracted and modelled for a frequency range from 1 GHz to 8.5 GHz, for a gate voltage from 0 V to 15 V and were obtained for graphene with a 50 µm width. The measured graphene resistance changed according to the device length and was in the range of 113 Ω to 558 Ω at 0 V, increasing to the range from 160 Ω to 886 Ω at 15 V. The measured capacitance was in the 0,64 pF to 1.2 pF range at 0 V, reducing to the range of 0.36 pF to 0.94 pF at 15 V. The inductance was only possible to determine for one device, being 1.4 nH at 0 V, and increasing up to 4.75 nH at 15 V. The extraction was further refined, determining the values of lumped components, allowing to include them in schematic simulators.

Through the known graphene's tunable characteristics, a device was fabricated. This device was comprised of a metallic antenna resembling a dipole with a gated graphene sheet in its center. The highest gain was -10.7 dBi at 4.9 GHz. Through this device, backscatter measurements were performed at around 10 cm from the aperture of a PE9887-11 horn antenna. It was possible to verify that through these measurements, the measured backscatter changed according to the applied graphene gate voltage, as expected. The applied voltage ranged from 0 V to 4 V (with a 10 nm thick Al_2O_3 gate). Furthermore, it was possible to model the measured device through simulations, using the extracted parameters from 0 V and 15 V (50 nm thick SiO_2 gate), since these have the closest chemical potential. The resulting variation from the measurements was from around -15 dB to around 15 dB, while in the simulations it was from around -21 dB to 15 dB. This demonstrates that the extracted graphene characteristics and modelling were performed successfully. Since the extracted graphene property values are within the typical values used in RF devices and systems, it means that using graphene biosensors for RF applications could be attainable. Furthermore, through this device, it is possible to demonstrate how such a device can be applied to biosensors. The gating voltage used in this example is equivalent to the modulation of graphene's chemical potential that is achieved through graphene functionalization to detect target biological analytes. Therefore, through functionalization, it should be possible to measure different responses according to different concentrations of target analytes thus allowing for wireless biosensors.

Graphene is, therefore, a very promising material for RF applications. However, due to its characteristics, it still requires further research to be performed. Although in terms of performance it currently is not comparable to commercial silicon devices, in the future it should be possible to obtain

similar performance when further miniaturization is required. Furthermore, in the future, some specific applications may require graphene specific characteristics.

7.1 Future work

Through this thesis it was possible to further explore graphene's RF properties. However, this research on the characterization of graphene and development of graphene RF biosensors is far from complete and it is also clear that further research is still needed. For the graphene characterization, changing the length of the device was explored, however, this analysis can be further refined by measuring even more different lengths. Furthermore, it should be possible to develop devices that have graphene with the previously characterized lengths and perform thorough testing on their properties through their integration in RF circuits and systems. Furthermore, only the characteristics of graphene with different lengths were explored in this work, meaning that it is still necessary to explore and determine how changing the width affects the properties of graphene. Through completing this analysis, it should be possible to obtain a full model that represents graphene's characteristics when it has different dimensions in either direction to fully integrate it in circuit analysis.

This work should also be completed through further uniformization of graphene's properties through fabrication. It was possible to conclude through the measurement of graphene and its characterization that the current properties of graphene such as its quality and contact resistance still need improvement. This should allow for the development of a model that is more robust.

The developed device allowed to demonstrate that through the properties of graphene it is possible to obtain a backscatter readout, however, it is still lacking performance. In this case, it is expected that the performance of the device can be further improved through the antenna design since the developed antenna had a very low efficiency.

Finally, it is necessary to develop of a fully functional graphene RF biomedical device. This can be achieved through the development of a graphene device that has known RF properties and through the integration of graphene functionalization.

8 REFERENCES

[1] S. Lee and Z. Zhong, "Nanoelectronic circuits based on two-dimensional atomic layer crystals," *Nanoscale*, vol. 6, no. 22, pp. 13283–13300, 2014, doi: 10.1039/C4NR03670K.

[2] W. Zhu, V. Perebeinos, M. Freitag, and P. Avouris, "Carrier scattering, mobilities, and electrostatic potential in monolayer, bilayer, and trilayer graphene," *Phys Rev B Condens Matter Mater Phys*, vol. 80, no. 23, pp. 1–18, 2009, doi: 10.1103/PhysRevB.80.235402.

[3] "Silicon electrical properties." Accessed: Oct. 27, 2019. [Online]. Available: https://www.azom.com/article.aspx?ArticleID=8346

[4] K. I. Bolotin, K. J. Sikes, J. Hone, H. L. Stormer, and P. Kim, "Temperature-dependent transport in suspended graphene," *Phys Rev Lett*, vol. 101, no. 9, pp. 1–4, 2008, doi: 10.1103/PhysRevLett.101.096802.

[5] R. S. Shishir and D. K. Ferry, "Velocity saturation in intrinsic graphene," *Journal of Physics Condensed Matter*, vol. 21, no. 34, 2009, doi: 10.1088/0953-8984/21/34/344201.

[6] P. C. Feijoo *et al.*, "Does carrier velocity saturation help to enhance: F maxin graphene field-effect transistors?," *Nanoscale Adv*, vol. 2, no. 9, pp. 4179–4186, 2020, doi: 10.1039/c9na00733d.

[7] A. H. Castro Neto, F. Guinea, N. M. R. Peres, K. S. Novoselov, and A. K. Geim, "The electronic properties of graphene," *Rev Mod Phys*, vol. 81, no. 1, pp. 109–162, 2009, doi: 10.1103/RevModPhys.81.109.

[8] H. Lee, K. Paeng, and I. S. Kim, "A review of doping modulation in graphene," *Synth Met*, vol. 244, no. May, pp. 36–47, 2018, doi: 10.1016/j.synthmet.2018.07.001.

[9] D. Y. Jeon *et al.*, "Radio-frequency electrical characteristics of single layer graphene," *Jpn J Appl Phys*, vol. 48, no. 9 Part 1, pp. 0916011–0916013, 2009, doi: 10.1143/JJAP.48.091601.

[10] K. S. Novoselov, V. I. Fal'Ko, L. Colombo, P. R. Gellert, M. G. Schwab, and K. Kim, "A roadmap for graphene," *Nature*, vol. 490, no. 7419, pp. 192–200, 2012, doi: 10.1038/nature11458.

[11] A. Pandey, Y. Gurbuz, V. Ozguz, J. H. Niazi, and A. Qureshi, "Graphene-interfaced electrical biosensor for label-free and sensitive detection of foodborne pathogenic E. coli O157:H7," *Biosens Bioelectron*, vol. 91, no. October 2016, pp. 225–231, 2017, doi: 10.1016/j.bios.2016.12.041.

[12] X. Liu *et al.*, "Highly sensitive and selective potassium ion detection based on graphene hall effect biosensors," *Materials*, vol. 11, no. 3, pp. 1–9, 2018, doi: 10.3390/ma11030399.

[13] W. Fu, L. Jiang, E. P. van Geest, L. M. C. Lima, and G. F. Schneider, "Sensing at the Surface of Graphene Field-Effect Transistors," *Advanced Materials*, vol. 29, no. 6, p. 1603610, 2017, doi: 10.1002/adma.201603610.

[14] C. Haslam, S. Damiati, T. Whitley, P. Davey, E. Ifeachor, and S. Awan, "Label-Free Sensors Based on Graphene Field-Effect Transistors for the Detection of Human Chorionic Gonadotropin Cancer Risk Biomarker," *Diagnostics*, vol. 8, no. 1, p. 5, Jan. 2018, doi: 10.3390/diagnostics8010005.

[15] X. Li *et al.*, "Graphene Inductors for High-Frequency Applications – Design, Fabrication, Characterization, and Study of Skin Effect," *IEDM, Technical Digest - International Electron Devices Meeting*, pp. 120–123, 2014, doi: 10.1109/IEDM.2014.7046989.

[16] L. Liao *et al.*, "High-speed graphene transistors with a self-aligned nanowire gate," *Nature*, vol. 467, no. 7313, pp. 305–308, 2010, doi: 10.1038/nature09405.

[17] R. Cheng *et al.*, "High-frequency self-aligned graphene transistors with transferred gate stacks," *Proc Natl Acad Sci U S A*, vol. 109, no. 29, pp. 11588–11592, 2012, doi: 10.1073/pnas.1205696109.

[18] S. K. Ghosh, S. Das, and S. Bhattacharyya, "Transmittive-type triple-band linear to circular polarization conversion in THz region using graphene-based metasurface," *Opt Commun*, vol. 480, no. June 2020, p. 126480, 2021, doi: 10.1016/j.optcom.2020.126480.

[19] K. Kim, J. Y. Choi, T. Kim, S. H. Cho, and H. J. Chung, "A role for graphene in silicon-based semiconductor devices," *Nature*, vol. 479, no. 7373, pp. 338–344, 2011, doi: 10.1038/nature10680.

[20] J. Jiang, J. H. Chu, and K. Banerjee, "CMOS-Compatible Doped-Multilayer-Graphene Interconnects for Next-Generation VLSI," pp. 799–802, 2018.

[21] D. Reddy, L. F. Register, G. D. Carpenter, and S. K. Banerjee, "Graphene field-effect transistors," *J Phys D Appl Phys*, vol. 45, no. 1, 2012, doi: 10.1088/0022-3727/45/1/019501.

[22] Y.-M. Lin *et al.*, "Wafer-Scale Graphene Integrated Circuit," *Science (1979)*, vol. 332, no. 6035, pp. 1294 LP – 1297, Jun. 2011.

[23] "Graphene Flagship - Competitive Call." Accessed: Mar. 25, 2018. [Online]. Available: http://www.graphenecall.esf.org/about-the-call/gf09-passive-components-for-rf-applications.html

[24] M. A. Andersson, Y. Zhang, and J. Stake, "A 185-215-GHz Subharmonic Resistive Graphene FET Integrated Mixer on Silicon," *IEEE Trans Microw Theory Tech*, vol. 65, no. 1, pp. 165–172, 2017, doi: 10.1109/TMTT.2016.2615928.

[25] A. C. Ferrari *et al.*, "Science and technology roadmap for graphene, related two-dimensional crystals, and hybrid systems," *Nanoscale*, vol. 7, no. 11, pp. 4598–4810, 2015, doi: 10.1039/C4NR01600A.

[26] J. Kang *et al.*, "On-chip intercalated-graphene inductors for next-generation radio frequency electronics," *Nat Electron*, vol. 1, no. 1, pp. 46–51, 2018, doi: 10.1038/s41928-017-0010-z.

[27] Z. Wang, Q. Zhang, P. Peng, and Z. Tian, "Q -factors of CVD monolayer graphene and graphite inductors," 2017.

[28] Z. Pan, X. Ji, M. Li, Z. Ye, and Y. Wang, "Modeling RF Behavior of Graphene up to 67GHz," *2014 IEEE MTT-S International Microwave Symposium (IMS2014)*, vol. 1, no. c, pp. 1–4, 2014, doi: 10.1109/MWSYM.2014.6848365.

[29] Y. Zhang, R. Ma, X. Zhen, Y. Kudva, P. Buhlmann, and S. J. Koester, "Capacitive Sensing of Glucose in Electrolytes Using Graphene Quantum Capacitance Varactors Capacitive Sensing of Glucose in Electrolytes Using Graphene Quantum Capacitance Varactors," 2017, doi: 10.1021/acsami.7b14864.

[30] C. F. Moldovan, W. A. Vitale, M. Tamagnone, J. R. Mosig, and A. M. Ionescu, "Graphene Quantum Capacitors for High-Q Tunable LC-tanks for RF ICs," *2016 46th European Solid-State Device Research Conference (ESSDERC)*, pp. 345–348, 2016, doi: 10.1109/ESSDERC.2016.7599657.

[31] C. F. Moldovan, W. A. Vitale, P. Sharma, M. Tamagnone, J. R. Mosig, and A. M. Ionescu, "Graphene Quantum Capacitors for High Frequency Tunable Analog Applications," *Nano Lett*, vol. 16, no. 8, pp. 4746–4753, 2016, doi: 10.1021/acs.nanolett.5b05235.

[32] D. Zhang *et al.*, "A Tunable Resonant Circuit Based on Graphene Quantum Capacitor," *Adv Electron Mater*, vol. 2001009, pp. 1–5, 2021, doi: 10.1002/aelm.202001009.

[33] R. Goyal and D. K. Vishwakarma, "Design of a graphene-based patch antenna on glass substrate for high-speed terahertz communications," *Microw Opt Technol Lett*, vol. 60, no. 7, pp. 1594–1600, 2018, doi: 10.1002/mop.31216.

[34] N. R. N. M. Rodrigues, R. de Oliveira, and V. Dmitriev, "Smart Terahertz Graphene Antenna: Operation as an Omnidirectional Dipole and as a Reconfigurable Directive Antenna," *IEEE Antennas Propag Mag*, vol. 60, no. 5, pp. 26–40, Oct. 2018, doi: 10.1109/MAP.2018.2859169.

[35] M. Esquius-Morote, J. S. Gomez-Diaz, and J. Perruisseau-Carrier, "Sinusoidally modulated graphene leaky-wave antenna for electronic beamscanning at THz," *IEEE Trans Terahertz Sci Technol*, vol. 4, no. 1, pp. 116–122, 2014, doi: 10.1109/TTHZ.2013.2294538.

[36] M. Dragoman, A. A. Muller, D. Dragoman, F. Coccetti, and R. Plana, "Terahertz antenna based on graphene," *J Appl Phys*, vol. 107, no. 10, pp. 1–4, 2010, doi: 10.1063/1.3427536.

[37] C. Lei *et al.*, "Planar Spiral Micro-Inductor Based on Graphene/Cu Composite Film Conductive Coil Fabricated by MEMS Technology," *J Electron Mater*, vol. 52, no. 12, pp. 8030–8037, Dec. 2023, doi: 10.1007/s11664-023-10720-3.

[38] X. Li, L. S. Wu, and J. F. Mao, "High-Frequency Analysis of Intercalated Multilayer Graphene (IMLG) and Implication for Tunable Terahertz Resonator Design," *IEEE Access*, vol. 5, no. c, 2017, doi: 10.1109/ACCESS.2017.2701506.

[39] R. Inum, M. M. Rana, and K. N. Shushama, "Performance analysis of graphene based nano dipole antenna on stacked substrate," *ICECTE 2016 - 2nd International Conference on Electrical, Computer and Telecommunication Engineering*, no. December, pp. 1–4, 2017, doi: 10.1109/ICECTE.2016.7879574.

[40] A. Biabanifard, M, Biabanifard, S, Javad Hosseini, S, Jahanshiri, "Design and Comparison of Terahertz Graphene Antenna: Ordinary dipole, Fractal dipole, Spiral, Bow-tie and Log-periodic," *Eng Technol Open Acc*, vol. 2, no. 2, 2018.

[41] Z. Fang *et al.*, "Plasmon-induced doping of graphene," *ACS Nano*, vol. 6, no. 11, pp. 10222–10228, 2012, doi: 10.1021/nn304028b.

[42] Z. Fang, Z. Liu, Y. Wang, P. M. Ajayan, P. Nordlander, and N. J. Halas, "Graphene-antenna sandwich photodetector," *Nano Lett*, vol. 12, no. 7, pp. 3808–3813, 2012, doi: 10.1021/nl301774e.

[43] D. Mencarelli, M. Dragoman, L. Pierantoni, T. Rozzi, and F. Coccetti, "Design of a coplanar graphene-based nano-patch antenna for microwave application," *IEEE MTT-S International Microwave Symposium Digest*, pp. 1–4, 2013, doi: 10.1109/MWSYM.2013.6697800.

[44] M. Dragoman *et al.*, "A tunable microwave slot antenna based on graphene," *Appl Phys Lett*, vol. 106, no. 15, 2015, doi: 10.1063/1.4917564.

[45] S. Koh *et al.*, "Graphene transparent antennas," *Carbon Reports*, vol. 2, no. 1, p. 020104, Mar. 2023, doi: 10.7209/carbon.020104.

[46] D. Sarkar, C. Xu, H. Li, and K. Banerjee, "High-frequency behavior of graphene-based interconnects-Part I: Impedance modeling," *IEEE Trans Electron Devices*, vol. 58, no. 3, pp. 843–852, 2011, doi: 10.1109/TED.2010.2102031.

[47] D. Sarkar, C. Xu, H. Li, and K. Banerjee, "High-frequency behavior of graphene-based interconnect-sPart II: Impedance analysis and implications for inductor design," *IEEE Trans Electron Devices*, vol. 58, no. 3, pp. 853–859, 2011, doi: 10.1109/TED.2010.2102035.

[48] D.-W. Wang, M.-J. Yuan, J.-Y. Dai, and W.-S. Zhao, "Electrical Modeling and Characterization of Graphene-Based On-Chip Spiral Inductors," *Micromachines (Basel)*, vol. 13, no. 11, p. 1829, Oct. 2022, doi: 10.3390/mi13111829.

[49] C. F. Moldovan, W. A. Vitale, P. Sharma, M. Tamagnone, J. R. Mosig, and A. M. Ionescu, "Graphene Quantum Capacitors for High Frequency Tunable Analog Applications - Supplementary Information," 2016, doi: 10.1021/acs.nanolett.5b05235.

[50] C. M. Nam and Y. S. Kwon, "High-performance planar inductor on thick oxidized porous silicon (OPS) substrate," *IEEE Microwave and Guided Wave Letters*, vol. 7, no. 8, pp. 236–238, 1997, doi: 10.1109/75.605489.

[51] P. Carazzetti, M.-A. Dubois, and N.-F. de Rooij, "High-performance micromachined RF planar iductors," in *The 13th International Conference on Solid-State Sensors, Actuators and Microsystems, 2005. Digest of Technical Papers. TRANSDUCERS '05.*, IEEE, 2010, pp. 1084–1087. doi: 10.1109/SENSOR.2005.1496644.

[52] J. M. López-villegas, J. Samitier, C. Cané, P. Losantos, and J. Bausells, "Improvement of the Quality Factor of RF Integrated Inductors by Layout Optimization," vol. 48, no. 1, pp. 76–83, 2000.

[53] Z. Hailu, "High quality factor RF MEMS tunable capacitor," *Microsystem Technologies*, vol. 23, no. 8, pp. 3719–3730, 2017, doi: 10.1007/s00542-016-3181-z.

[54] F. Khan, J. Lu, and Y. Zhu, "Experimental investigation of actuation in a micromachined electrically floating tunable capacitor," *Microelectron Eng*, vol. 213, no. October 2018, pp. 31–34, 2019, doi: 10.1016/j.mee.2019.02.007.

[55] H. Liu, X. Guo, Z. You, and Z. Liu, "Fabrication of a Tunable Capacitor with a Non-Planar Plate by Using Titanium and Polyimide as Sacrificial Layers," *Proceedings of the IEEE International Conference on Micro Electro Mechanical Systems (MEMS)*, vol. 2019-Janua, no. January, pp. 863–866, 2019, doi: 10.1109/MEMSYS.2019.8870693.

[56] L. Anzi *et al.*, "Ultra-low contact resistance in graphene devices at the Dirac point," *2d Mater*, vol. 5, no. 2, 2018, doi: 10.1088/2053-1583/aaab96.

[57] T. Cusati *et al.*, "Electrical properties of graphene-metal contacts /639/301/1005/1007 /639/925/927/1007 /119 /119/118 /120 /128 article," *Sci Rep*, vol. 7, no. 1, pp. 1–11, 2017, doi: 10.1038/s41598-017-05069-7.

[58] J. T. Smith, A. D. Franklin, D. B. Farmer, and C. D. Dimitrakopoulos, "Reducing contact resistance in graphene devices through contact area patterning," *ACS Nano*, vol. 7, no. 4, pp. 3661–3667, 2013, doi: 10.1021/nn400671z.

[59] N. A. A. Rahim, M. H. Kara, Z. Awang, and M. R. Mahmood, "Accuracy issues in microwave characterization of graphene transmission lines," in *2014 IEEE 2nd International Symposium on Telecommunication Technologies (ISTT)*, IEEE, Nov. 2014, pp. 305–309. doi: 10.1109/ISTT.2014.7238225.

[60] H. Packard, "Applying the HP 8510B TRL Calibration for Non-Coaxial Measurements," *Product Note*, pp. 8510–8, 1987.

[61] R. F. Kaiser and D. F. Williams, "Sources of error in coplanar-waveguide TRL calibrations," *54th ARFTG Conference Digest Fall 1999: Automatic RF Techniques Group: Characterization of Broadband Access Technologies, ARFTG Fall 1999*, no. 303, pp. 1–6, 1999, doi: 10.1109/ARFTG.1999.327367.

[62] R. B. Marks, "A Multiline Method of Network Analyzer Calibration," *IEEE Trans Microw Theory Tech*, vol. 39, no. 7, pp. 1205–1215, 1991, doi: 10.1109/22.85388.

[63] "TRL calibration." [Online]. Available: https://www.microwaves101.com/encyclopedias/trl-calibration

[64] H. Forstén, "TRL calibration procedure." [Online]. Available: https://hforsten.com/trl-measurements-with-homemade-vna-and-open-source-software.html

[65] "scikit-rf." Accessed: May 13, 2021. [Online]. Available: https://scikit-rf.readthedocs.io/en/latest/index.html

[66] G. V. Bianco *et al.*, "Extraordinary low sheet resistance of CVD graphene by thionyl chloride chemical doping," *Carbon N Y*, vol. 170, pp. 75–84, 2020, doi: 10.1016/j.carbon.2020.07.038.

[67] J. Y. Hong *et al.*, "A Rational Strategy for Graphene Transfer on Substrates with Rough Features," *Advanced Materials*, vol. 28, no. 12, pp. 2382–2392, 2016, doi: 10.1002/adma.201505527.

[68] D. Correas-Serrano, J. S. Gomez-Diaz, A. Alu, and A. Alvarez-Melcon, "Electrically and Magnetically Biased Graphene-Based Cylindrical Waveguides: Analysis and Applications as Reconfigurable Antennas," *IEEE Trans Terahertz Sci Technol*, vol. 5, no. 6, pp. 951–960, 2015, doi: 10.1109/TTHZ.2015.2472985.

[69] J. Fontebasso Neto, L. C. Moreira, and F. S. Correra, "Design Equations for Spiral and Scalable Cross Inductors on 0.35 μm CMOS Technology," *Journal of Microwaves, Optoelectronics and*

Electromagnetic Applications, vol. 17, no. 3, pp. 403–415, Sep. 2018, doi: 10.1590/2179-10742018v17i31215.

[70] W. B. Kuhn, Xin He, and M. Mojarradi, "Modeling spiral inductors in SOS processes," *IEEE Trans Electron Devices*, vol. 51, no. 5, pp. 677–683, May 2004, doi: 10.1109/TED.2004.826868.

[71] N.-J. Oh and S.-G. Lee, "A Simple Model Parameter Extraction Methodology for an On-Chip Spiral Inductor," *ETRI Journal*, vol. 28, no. 1, pp. 115–118, Feb. 2006, doi: 10.4218/etrij.06.0205.0056.

[72] J. H. Chang, A. Huzayyin, K. Lian, and F. Dawson, "Quantum capacitance of graphene in contact with metal," *Appl Phys Lett*, vol. 107, no. 19, p. 193902, Nov. 2015, doi: 10.1063/1.4935365.

[73] S. A. Awan *et al.*, "Transport conductivity of graphene at RF and microwave frequencies," *2d Mater*, vol. 3, no. 1, p. 0, 2016, doi: 10.1088/2053-1583/3/1/015010.

[74] H. Lee *et al.*, "Intrinsic characteristics of transmission line of graphenes at microwave frequencies Intrinsic characteristics of transmission line of graphenes at microwave frequencies," vol. 223102, pp. 100–103, 2012, doi: 10.1063/1.4722585.

[75] J. M. P. N. S. Fernandes, "Design, fabrication and integration of 3D micro-structures using self-folding techniques for ultra-miniaturization of smart microsystems," 2019.

[76] T. Palacios, A. Hsu, and H. Wang, "Applications of graphene devices in RF communications," *IEEE Communications Magazine*, vol. 48, no. 6, pp. 122–128, 2010, doi: 10.1109/MCOM.2010.5473873.

[77] I. Colmiais, V. Silva, J. Borme, P. Alpuim, and P. M. Mendes, "Towards RF graphene devices : A review," *FlatChem*, vol. 35, no. April, 2022, doi: 10.1016/j.flatc.2022.100409.

[78] L. Liao and X. Duan, "Graphene for radio frequency electronics," *Materials Today*, vol. 15, no. 7–8, pp. 328–338, 2012, doi: 10.1016/S1369-7021(12)70138-4.

[79] X. Li, L. Colombo, and R. S. Ruoff, "Synthesis of Graphene Films on Copper Foils by Chemical Vapor Deposition," *Advanced Materials*, vol. 28, no. 29, pp. 6247–6252, 2016, doi: 10.1002/adma.201504760.

[80] G. A. López and E. J. Mittemeijer, "The solubility of C in solid Cu," *Scr Mater*, vol. 51, no. 1, pp. 1–5, Jul. 2004, doi: 10.1016/j.scriptamat.2004.03.028.

[81] Y. Liu *et al.*, "How Low Nucleation Density of Graphene on CuNi Alloy is Achieved," *Advanced Science*, vol. 5, no. 6, p. 1700961, Jun. 2018, doi: 10.1002/advs.201700961.

[82] M. L. Narula, V. B. Tare, and W. L. Worrell, "Diffusivity and solubility of oxygen in solid copper using potentiostatic and potentiometric techniques," *Metallurgical Transactions B*, vol. 14, no. 4, pp. 673–677, Dec. 1983, doi: 10.1007/BF02653953.

[83] S. Chaitoglou, E. Bertran, and J. L. Andujar, "Growth Study and Characterization of Single-Layer Graphene Structures Deposited on Copper Substrate by Chemical Vapour Deposition," *Graphene Materials - Structure, Properties and Modifications*, 2017, doi: 10.5772/67439.

[84] G. H. Han *et al.*, "Influence of copper morphology in forming nucleation seeds for graphene growth," *Nano Lett*, vol. 11, no. 10, pp. 4144–4148, 2011, doi: 10.1021/nl201980p.

[85] C. Yu *et al.*, "High-Frequency Flexible Graphene Field-Effect Transistors with Short Gate Length of 50 nm and Record Extrinsic Cut-Off Frequency," *physica status solidi (RRL) - Rapid Research Letters*, vol. 12, no. 5, p. 1700435, May 2018, doi: 10.1002/pssr.201700435.

[86] A. Isacsson, A. W. Cummings, L. Colombo, L. Colombo, J. M. Kinaret, and S. Roche, "Scaling properties of polycrystalline graphene: A review," *2d Mater*, vol. 4, no. 1, 2017, doi: 10.1088/2053-1583/aa5147.

[87] J. H. Choi, J. Lee, M. Byeon, T. E. Hong, H. Park, and C. Y. Lee, "Graphene-Based Gas Sensors with High Sensitivity and Minimal Sensor-to-Sensor Variation," *ACS Appl Nano Mater*, vol. 3, no. 3, pp. 2257–2265, 2020, doi: 10.1021/acsanm.9b02378.

[88] Q. Yuan, G. Song, D. Sun, and F. Ding, "Formation of Graphene Grain Boundaries on Cu(100) Surface and a Route Towards Their Elimination in Chemical Vapor Deposition Growth," *Sci Rep*, vol. 4, no. 1, p. 6541, Oct. 2014, doi: 10.1038/srep06541.

[89] M. D. Bhatt, H. Kim, and G. Kim, "Various defects in graphene: a review," *RSC Adv*, vol. 12, no. 33, pp. 21520–21547, 2022, doi: 10.1039/d2ra01436j.

[90] I. Vlassiouk *et al.*, "Role of Hydrogen in Chemical Vapor Deposition Growth of Large Single-Crystal Graphene," *ACS Nano*, vol. 5, no. 7, pp. 6069–6076, Jul. 2011, doi: 10.1021/nn201978y.

[91] Z. G. Wang *et al.*, "Effects of methane flux on structural and transport properties of CVD-grown graphene films," *Vacuum*, vol. 86, no. 7, pp. 895–898, Feb. 2012, doi: 10.1016/j.vacuum.2011.05.011.

[92] G. D. Kwon, E. Moyen, Y. J. Lee, Y. W. Kim, S. H. Baik, and D. Pribat, "Influence of the copper substrate roughness on the electrical quality of graphene," *Mater Res Express*, vol. 4, no. 1, p. 015604, Jan. 2017, doi: 10.1088/2053-1591/aa54d3.

[93] X. Zhang *et al.*, "Hydrogen-induced effects on the CVD growth of high-quality graphene structures," *Nanoscale*, vol. 5, no. 18, p. 8363, 2013, doi: 10.1039/c3nr01599h.

[94] Y. Hao *et al.*, "The Role of Surface Oxygen in the Growth of Large Single-Crystal Graphene on Copper," *Science (1979)*, vol. 342, no. 6159, pp. 720–723, Nov. 2013, doi: 10.1126/science.1243879.

[95] P. Braeuninger-Weimer, B. Brennan, A. J. Pollard, and S. Hofmann, "Understanding and Controlling Cu-Catalyzed Graphene Nucleation: The Role of Impurities, Roughness, and Oxygen Scavenging," *Chemistry of Materials*, vol. 28, no. 24, pp. 8905–8915, Dec. 2016, doi: 10.1021/acs.chemmater.6b03241.

[96] X. Li *et al.*, "Large-Area Graphene Single Crystals Grown by Low-Pressure Chemical Vapor Deposition of Methane on Copper," *J Am Chem Soc*, vol. 133, no. 9, pp. 2816–2819, Mar. 2011, doi: 10.1021/ja109793s.

[97] H. Yan *et al.*, "Effect of staged methane flow on morphology and growth rate of graphene monolayer domains by low-pressure chemical vapor deposition," *Thin Solid Films*, vol. 736, p. 138921, Oct. 2021, doi: 10.1016/j.tsf.2021.138921.

[98] P. Trinsoutrot, C. Rabot, H. Vergnes, A. Delamoreanu, A. Zenasni, and B. Caussat, "The Role of the Gas Phase in Graphene Formation by CVD on Copper," *Chemical Vapor Deposition*, vol. 20, no. 1-2–3, pp. 51–58, Mar. 2014, doi: 10.1002/cvde.201307075.

[99] X. Yang and M. Yan, "Removing contaminants from transferred CVD graphene," *Nano Res*, vol. 13, no. 3, pp. 599–610, 2020, doi: 10.1007/s12274-020-2671-6.

[100] V. Shautsova, A. M. Gilbertson, N. C. G. Black, S. A. Maier, and L. F. Cohen, "Hexagonal Boron Nitride assisted transfer and encapsulation of large area CVD graphene," *Sci Rep*, vol. 6, no. July, pp. 1–8, 2016, doi: 10.1038/srep30210.

[101] J. Lee *et al.*, "Clean transfer of graphene and its effect on contact resistance," *Appl Phys Lett*, vol. 103, no. 10, 2013, doi: 10.1063/1.4819740.

[102] F. Qing, Y. Zhang, Y. Niu, R. Stehle, Y. Chen, and X. Li, "Towards large-scale graphene transfer," *Nanoscale*, vol. 12, no. 20, pp. 10890–10911, 2020, doi: 10.1039/D0NR01198C.

[103] C.-D. Liao *et al.*, "Optimizing PMMA solutions to suppress contamination in the transfer of CVD graphene for batch production," *Beilstein Journal of Nanotechnology*, vol. 13, pp. 796–806, Aug. 2022, doi: 10.3762/bjnano.13.70.

[104] J. W. Suk *et al.*, "Enhancement of the Electrical Properties of Graphene Grown by Chemical Vapor Deposition via Controlling the Effects of Polymer Residue," *Nano Lett*, vol. 13, no. 4, pp. 1462–1467, Apr. 2013, doi: 10.1021/nl304420b.

[105] A. Pirkle *et al.*, "The effect of chemical residues on the physical and electrical properties of chemical vapor deposited graphene transferred to SiO 2," *Appl Phys Lett*, vol. 99, no. 12, p. 122108, Sep. 2011, doi: 10.1063/1.3643444.

[106] Y. Ahn, H. Kim, Y.-H. Kim, Y. Yi, and S.-I. Kim, "Procedure of removing polymer residues and its influences on electronic and structural characteristics of graphene," *Appl Phys Lett*, vol. 102, no. 9, p. 091602, Mar. 2013, doi: 10.1063/1.4794900.

[107] H. J. Jeong *et al.*, "Improved transfer of chemical-vapor-deposited graphene through modification of intermolecular interactions and solubility of poly(methylmethacrylate) layers," *Carbon N Y*, vol. 66, pp. 612–618, Jan. 2014, doi: 10.1016/j.carbon.2013.09.050.

[108] A. Avsar *et al.*, "Toward wafer scale fabrication of graphene based spin valve devices," *Nano Lett*, vol. 11, no. 6, pp. 2363–2368, 2011, doi: 10.1021/nl200714q.

[109] A. Pirkle *et al.*, "The effect of chemical residues on the physical and electrical properties of chemical vapor deposited graphene transferred to SiO2," *Appl Phys Lett*, vol. 99, no. 12, pp. 2009–2012, 2011, doi: 10.1063/1.3643444.

[110] S. M. Kim *et al.*, "The effect of copper pre-cleaning on graphene synthesis," *Nanotechnology*, vol. 24, no. 36, p. 365602, Sep. 2013, doi: 10.1088/0957-4484/24/36/365602.

[111] B. Dai *et al.*, "Rational design of a binary metal alloy for chemical vapour deposition growth of uniform single-layer graphene," *Nat Commun*, vol. 2, no. 1, 2011, doi: 10.1038/ncomms1539.

[112] Y. C. Lin, C. C. Lu, C. H. Yeh, C. Jin, K. Suenaga, and P. W. Chiu, "Graphene annealing: How clean can it be?," *Nano Lett*, vol. 12, no. 1, pp. 414–419, 2012, doi: 10.1021/nl203733r.

[113] G. B. Barin, Y. Song, I. D. F. Gimenez, A. G. S. Filho, L. S. Barreto, and J. Kong, "Optimized graphene transfer: Influence of polymethylmethacrylate (PMMA) layer concentration and baking time on grapheme final performance," *Carbon N Y*, vol. 84, no. C, pp. 82–90, 2015, doi: 10.1016/j.carbon.2014.11.040.

[114] X. Li *et al.*, "Transfer of large-area graphene films for high-performance transparent conductive electrodes," *Nano Lett*, vol. 9, no. 12, pp. 4359–4363, 2009, doi: 10.1021/nl902623y.

[115] Y. Jia *et al.*, "Toward High Carrier Mobility and Low Contact Resistance: Laser Cleaning of PMMA Residues on Graphene Surfaces," *Nanomicro Lett*, vol. 8, no. 4, pp. 336–346, 2016, doi: 10.1007/s40820-016-0093-5.

[116] Y. Ahn, J. Kim, S. Ganorkar, Y. H. Kim, and S. Il Kim, "Thermal annealing of graphene to remove polymer residues," *Materials Express*, vol. 6, no. 1, pp. 69–76, 2016, doi: 10.1166/mex.2016.1272.

[117] S. K. Hong, S. C. Jeon, W. S. Hwang, and B. J. Cho, "Resistance analysis and device design guideline for graphene RF transistors," *2d Mater*, vol. 2, no. 3, p. 034011, Jul. 2015, doi: 10.1088/2053-1583/2/3/034011.

[118] S. M. Song, J. K. Park, O. J. Sul, and B. J. Cho, "Determination of work function of graphene under a metal electrode and its role in contact resistance," *Nano Lett*, vol. 12, no. 8, pp. 3887–3892, 2012, doi: 10.1021/nl300266p.

[119] O. Balci and C. Kocabas, "Rapid thermal annealing of graphene-metal contact," *Appl Phys Lett*, vol. 101, no. 24, 2012, doi: 10.1063/1.4769817.

[120] W. Li *et al.*, "Ultraviolet/ozone treatment to reduce metal-graphene contact resistance," *Appl Phys Lett*, vol. 102, no. 18, 2013, doi: 10.1063/1.4804643.

[121] S. Min Song, T. Yong Kim, O. Jae Sul, W. Cheol Shin, and B. Jin Cho, "Improvement of graphene-metal contact resistance by introducing edge contacts at graphene under metal," *Appl Phys Lett*, vol. 104, no. 18, 2014, doi: 10.1063/1.4875709.

[122] J. T. Smith, A. D. Franklin, D. B. Farmer, and C. D. Dimitrakopoulos, "Reducing contact resistance in graphene devices through contact area patterning," *ACS Nano*, vol. 7, no. 4, pp. 3661–3667, 2013, doi: 10.1021/nn400671z.

[123] J. Lee *et al.*, "Clean transfer of graphene and its effect on contact resistance," *Appl Phys Lett*, vol. 103, no. 10, 2013, doi: 10.1063/1.4819740.

[124] C. Gong *et al.*, "Metal-graphene-metal sandwich contacts for enhanced interface bonding and work function control," *ACS Nano*, vol. 6, no. 6, pp. 5381–5387, 2012, doi: 10.1021/nn301241p.

[125] F. Giubileo and A. Di Bartolomeo, "The role of contact resistance in graphene field-effect devices," *Prog Surf Sci*, vol. 92, no. 3, pp. 143–175, Aug. 2017, doi: 10.1016/j.progsurf.2017.05.002.

[126] K. Nagashio, T. Nishimura, K. Kita, and A. Toriumi, "Contact resistivity and current flow path at metal/graphene contact," *Appl Phys Lett*, vol. 97, no. 14, pp. 8–11, 2010, doi: 10.1063/1.3491804.

[127] K. Nagashio, T. Nishimura, K. Kita, and A. Toriumi, "Contact resistivity and current flow path at metal/graphene contact," *Appl Phys Lett*, vol. 97, no. 14, pp. 8–11, 2010, doi: 10.1063/1.3491804.

[128] J. S. Moon *et al.*, "Ultra-low resistance ohmic contacts in graphene field effect transistors," *Appl Phys Lett*, vol. 100, no. 20, pp. 2010–2013, 2012, doi: 10.1063/1.4719579.

[129] L. Wang *et al.*, "One-dimensional electrical contact to a two-dimensional material," *Science (1979)*, vol. 342, no. 6158, pp. 614–617, 2013, doi: 10.1126/science.1244358.

[130] F. Xia, V. Perebeinos, Y. M. Lin, Y. Wu, and P. Avouris, "The origins and limits of metal-graphene junction resistance," *Nat Nanotechnol*, vol. 6, no. 3, pp. 179–184, 2011, doi: 10.1038/nnano.2011.6.

[131] T. Cusati *et al.*, "Electrical properties of graphene-metal contacts," *Sci Rep*, vol. 7, no. 1, p. 5109, Jul. 2017, doi: 10.1038/s41598-017-05069-7.

[132] P. D. Cabral *et al.*, "Clean-Room Lithographical Processes for the Fabrication of Graphene Biosensors," *Materials*, vol. 13, no. 24, p. 5728, Dec. 2020, doi: 10.3390/ma13245728.

[133] M. Abrantes *et al.*, "Ultrasensitive dopamine detection with graphene aptasensor multitransistor arrays," *J Nanobiotechnology*, vol. 20, no. 1, p. 495, Nov. 2022, doi: 10.1186/s12951-022-01695-0.

[134] I. Palacio *et al.*, "Attomolar detection of hepatitis C virus core protein powered by molecular antenna-like effect in a graphene field-effect aptasensor," *Biosens Bioelectron*, vol. 222, p. 115006, Feb. 2023, doi: 10.1016/j.bios.2022.115006.

[135] H. Dinis, I. Colmiais, and P. M. Mendes, "A multiantenna approach to maximize wireless power transfered to implantable devices," *2017 International Applied Computational Electromagnetics Society Symposium - Italy, ACES 2017*, 2017, doi: 10.23919/ROPACES.2017.7916363.

[136] I. Colmiais, H. Dinis, and P. M. Mendes, "WPT system for implantable devices using a phased array and tracking algorithm for freely moving rats," in *2019 IEEE 6th Portuguese Meeting on Bioengineering (ENBENG)*, IEEE, 2019, pp. 1–4. doi: 10.1109/ENBENG.2019.8692495.

[137] H. Dinis, I. Colmiais, and P. M. Mendes, "Extending the limits of wireless power transfer to miniaturized implantable electronic devices," *Micromachines (Basel)*, vol. 8, no. 12, p. 359, Dec. 2017, doi: 10.3390/mi8120359.

[138] H. Dinis, I. Colmiais, and Paulo. M. Mendes, "Design and validation of a six-antenna WPT system with tracking capabilites for biomedical devices," *2019 17th IEEE International New Circuits and Systems Conference (NEWCAS)*, pp. 1–4, Jun. 2019, doi: 10.1109/NEWCAS44328.2019.8961219.

[139] A. C. Ferrari and D. M. Basko, "Raman spectroscopy as a versatile tool for studying the properties of graphene," *Nat Nanotechnol*, vol. 8, no. 4, pp. 235–246, Apr. 2013, doi: 10.1038/nnano.2013.46.

[140] L. M. Malard, M. A. Pimenta, G. Dresselhaus, and M. S. Dresselhaus, "Raman spectroscopy in graphene," *Phys Rep*, vol. 473, no. 5–6, pp. 51–87, Apr. 2009, doi: 10.1016/j.physrep.2009.02.003.

[141] E. Instruments, “Raman Microscopy of Graphene.” [Online]. Available: https://www.edinst.com/us/application-note-raman-microscopy-of-graphene/

ANNEX 1 - HARDMASK FABRICATION

The required thickness of copper (5 µm) means that 10 µm of the resist AZ10XT were necessary to perform the electroplating growth. However, this resist thickness is too large for performing the laser lithography through the DWL, since it would require several passages of the laser, accumulating several hours of exposure. Therefore, the alternative is fabricating a hardmask that is specific for this step. It allows to perform the lithography of the desired structures faster than the DWL, although it comes with an initial extra time spent on its fabrication and limits the design and fabrication of new structures. The steps for the fabrication of the hardmask are shown in Figure 85.

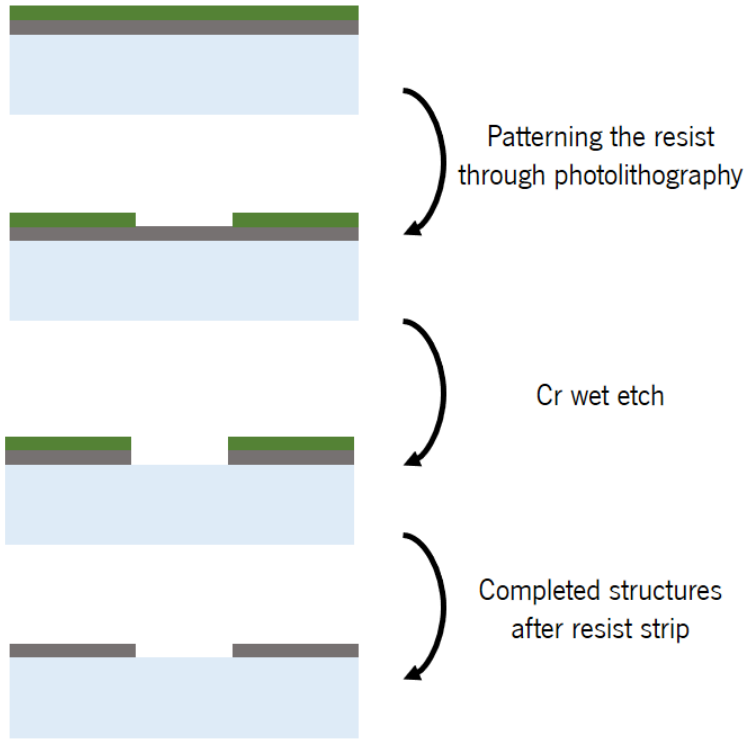


Figure 85 - Steps of the fabrication of the hardmask.

Its fabrication starts with a 16 inch by 16 inch square glass with pre-deposited Cr and pre-coated with 530 nm of AZ1518 photoresist from Nanofilm. The process starts with patterning the mirrored layout (since the hardmask will be flipped for the lithography) in the DWL. Then, the mask is manually developed in AZ400K for 90 seconds in the orbital mixer in the low agitation setting. Afterwards, the mask is rinsed in DI H_2O, and dried with an N_2 gun. An optical microscope verification is performed and after checking that the etching was performed correctly, the Cr is etched. This is performed with the etchant Etch18, in which the mask is placed for 1 minute and 40 seconds in the orbital mixer in the low agitation setting, followed by DI H_2O rinse and N_2 gun dry. Finally, after verifying that the etching was performed successfully

through the optical microscope, the resist is removed by placing the mask in Microstrip 3001 for 5 minutes in low agitation, followed by an IPA rinse, a DI H_2O rinse and N_2 gun dry. In the end, optical microscope images were acquired, as shown in Figure 86, where it is possible to observe that the masks were successfully fabricated.

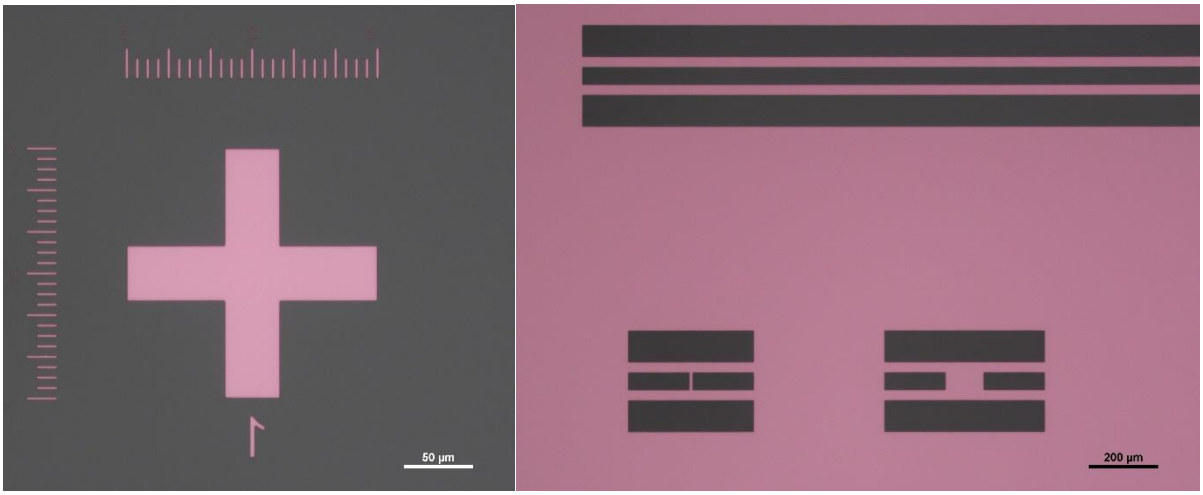


Figure 86 - Optical microscope pictures of the patterned hard mask, on the left is shown one of the alignment marks, and on the right parts of the structures are shown.

ANNEX 2 - CONFOCAL RAMAN SPECTROSCOPY

To confirm the presence of graphene, characterize its quality, and if it is single layer, confocal Raman spectroscopy is used. The WITec Alpha300R (Ulm, Germany) confocal Raman microscope is used with a frequency doubled Nd:YAH laser, using a wavelength of 532 nm. The data analysis is performed through the WITec Project FOUR+ software. This analysis is performed throughout the fabrication process, starting immediately after the graphene growth, and ending with the fabricated device. The laser power used to acquire the spectra is usually 2 mW, and focused through the Raman system lenses. The number of acquisitions and the acquisition time can be modified in each measurement.

To check whether the graphene flakes are monolayer, the ratio between the 2D (I2D ~2700 cm^{-1}) and G (IG ~1590 cm^{-1}) peaks can be used, where it is considered that monolayer fulfils the condition I2D/IG > 1 [139]. Finally, the intensity of the D mode (ID ~1350 cm^{-1}) can be used to estimate the presence of defects [140]. These peaks can be observed in Figure 87.

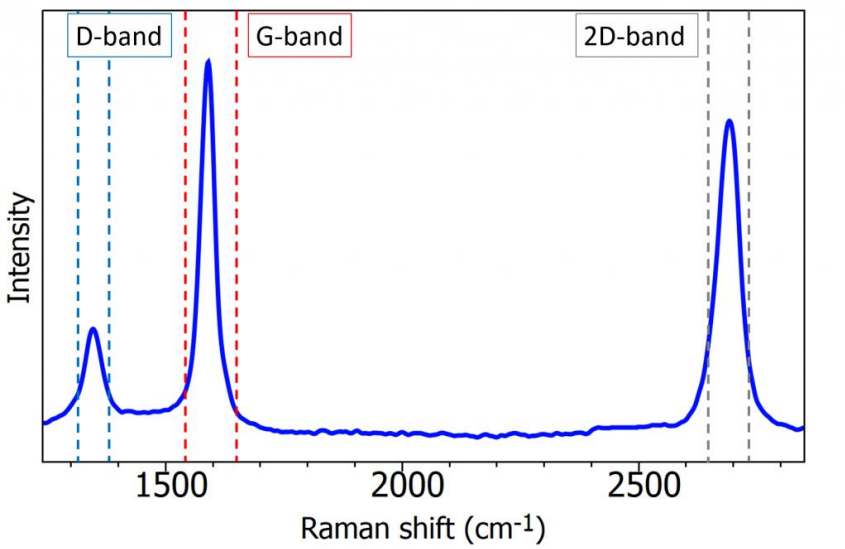


Figure 87 - Raman spectrum of graphene, with the identification of the D, G, and 2D peaks [141].